Università degli studi di Cagliari
Physics Department

Tuning the magnetic anisotropy in nanostructured magnetic oxides

Magnetic properties of ferrite and manganite nanostructures

A dissertation submitted for the degree of

Doctor of Philosophy in Physics

Presented by **Giuseppe Muscas** (Cycle XXVII)

Supervisor **Prof. Giorgio Concas**

Co-supervisor **Doc. Davide Peddis**

PhD School Coordinator **Prof. Paolo Ruggerone**

SSD FIS/03, FIS/01

Final exam, academic year 2013-2014

UNIONE EUROPEA
Fondo sociale europeo

REGIONE AUTONOMA DELLA SARDEGNA

FSE 2007-2013
POR SARDEGNA
obiettivo competitività regionale e occupazione

Università degli Studi di Cagliari

DOTTORATO DI RICERCA IN FISICA

Ciclo XXVII

Tuning the magnetic anisotropy in nanostructured magnetic oxides

Magnetic properties of ferrite and manganite nanostructures

Settore scientifico disciplinare di afferenza SSD

FIS/03, FIS/01

Presentata da: **Giuseppe Muscas**

Coordinatore Dottorato: **Prof. Paolo Ruggerone**

Tutor / Relatore: Prof. **Giorgio Concas**

Esame finale anno accademico 2013 – 2014

Knowledge is the tool to
justify your imagination

Abstract

Among nanostructured magnetic materials, nanoparticles (NPs) are unique complex physical objects: in these systems a multidomain organization is energetically unfavorable and single-magnetic-domain particles are formed, each one with a huge magnetic moment with comparison to that of single atoms, thus they are often named "supermoment". The attractive performance of magnetic NPs based materials are appealing for several technological fields ranging from nanomedicine to high-density magneto recording. Thus, understanding the physics of magnetic nanoparticles and controlling their magnetic properties represent hot topics not only for fundamental studies but also for technological applications. The magnetic behavior of such entities is related to the reversal of their magnetization; this can be a thermal or a field activated transition, which is characterized by an energy barrier defined as a magnetic anisotropy energy (MAE), which is influenced by several parameters. Thus, the tuning of the magnetic properties of nanoparticles means control of the MAE.

In this work it will be discussed how to tune the MAE at the nanoscale showing the main parameters that can influence the anisotropy itself. It will be investigated the role of particle volume in the effective anisotropy, and its correlation with the surface contribution, exploring its strong effect with particle size below 10 nm. In this framework it will be investigated the role of organic coating, underlining its ability to reduce the magnetic disorder arising from the broken symmetry at particles surface. In addition, in nanoparticle ensemble, the MAE may differ from one particle to another due to particles size and shape distributions. Thus it will be defined a detailed statistical analysis of particles' morphology, leading to the development of a new instrument to analyze particles morphology, called "aspect maps".

The relation between the physical chemical structures of nanoparticles will be investigated on nickel doped cobalt ferrite samples, demonstrating how to tune the MAE by chemical composition, i.e., controlling magnetocrystalline anisotropy. Furthermore it will be analyzed the evolution of interparticles interactions with respect single particle magnetic anisotropy by means of a modified random anisotropy model.

The last part of this work will deal with the design of novel nanostructured composites. $La_{0.67}Ca_{0.33}MnO_3$ and $CoFe_2O_4$ will be combined using two different structures, which can be easily extent to other materials, to improve their magnetic interactions in order to obtain tunable magnetotrasport proprieties of the final composites.

Contents

List of figures

Preface

This thesis covers part of the work that I have performed between March 2012 and February 2015 for the PhD in Physics at the Physics department of University of Cagliari under the supervision of Prof. Giorgio Concas and Doc. Davide Peddis.

The first part of the synthesis and characterization has been carried out in chemistry department (under the supervision of Doc. Carla Cannas and Prof. Anna Musinu) and in Physics Department under the supervision of Prof. Giorgio Concas.

Since May 5th 2013 to today I am associate researcher at Institute of Structure of the Matter (ISM) of CNR (Ref. Doc. Davide Peddis), within the project "Materiali magnetici nanostrutturati". Thanks to this, the great part of the magnetic measurements has been carried out at ISM-CNR.

During the period September – October 2013 I have spent 6 weeks at the Department of Chemical Engineering of the Norwegian University of Science and Technology (NTNU) at Trondheim, Norway, where I have developed the synthesis and structural characterization of iron oxide nanoparticles.

During the period October 2013 – March 2014 I have spent 6 months at the Department of Engineering Science of Uppsala University (Sweden), where I have developed the synthesis of nanocomposites materials and I have carried out the magnetic and magnetoelectric characterization of my samples. In 2014 I have received a grant from the Swedish foundation *C.M. Lerici*, to finance a further period of 3 moths (September – November 2014) at Uppsala University to conclude my work on nanocomposites.

Between February 25th and March 8th 2013 I have attend the European School on Magnetism in Cargèse, France.

I gratefully acknowledge Sardinia Regional Government for the financial support of my PhD scholarship (P.O.R. Sardegna F.S.E. Operational Programme of the Autonomous Region of Sardinia, European Social Fund 2007-2013 - Axis IV Human Resources, Objective l.3, Line of Activity l.3.1.)

Acknowledgments

This has been a three years long journey, the first real steps for my future work. I must thank my supervisor Prof. Giorgio Concas; we have worked side by side introducing me to the Mössbauer world such as in the activity of tutor, “fighting” with hundreds of students in the last years! Thank you for your help and role.

My PhD should be nothing of what it is without my “co-supervisor” Doc. Davide Peddis. Already during my Master you introduced me to research, turning on my curiosity about magnetic materials. Thank you to have continuously involved me in a lot of projects, to have open for me so many possibilities among conferences, activities, collaborations, abroad periods, all things that have given a real plus to my PhD but, most importantly, which have open my mind and deeply change my life! Thank you very much Boss!

I would like to thank Prof. Anna Musinu and Doc. Carla Cannas, you have given me the opportunity to work in your lab and you have share your knowledge many times with useful discussions. Thanks also to all my friends Mauro, Federica, Andrea, Valentina, Roberto, we share a lot of time in lab, thank you for your support!!

During my periods abroad, I have known many beautiful friends; thank you Doc. Gurvinder Singh, to have worked with me in the beautiful facilities of NTNU! I have spent two months in Norway living a full period at work, but also full of experiences with Navjeet, Sarabjet and of course my friends Danny and Manny, Norway was so funny thanks to you!

The first time I was in Uppsala I completely fallen in love with Sweden; it is of course due to this beautiful country, but nevertheless, it was thanks to the beautiful people I have met there. Thank you Prof. Roland Mathieu, you have really opened my perspective about science. Thanks to Doc. Petra Jönsson and, of course, to Alfred, Linnea and Louise for the so nice time spent with me! Special thanks to Doc. P. Anil Kumar, for all the time you have spent with me with patience in lab and our scientific discussions; I cannot forget our lunches! Thanks to Mikael, for all time spent with me, to Prof. Per Nordblad, the living legend of Uppsala, and to Prof. Sergey A. Ivanov, the magician of diffraction!

Thanks to my parents, Laura and Efisio, if today I am a little bit closer to be a man it is thanks to you, your help, your support, your example, thank you! Thank you to my brother Francesco, because we only need to look each other in the eyes to face whatever we meet!!

Finally, but first in my mind, thank you my little star. Your daily support in all this journey has been fundamental; this “travel” itself could not be so significant without you! I know I have found my second half, the best one. Thank you Sheila!

March 2015,

Giuseppe Muscas

Publications and contributions

Part of the work carried out during my PhD has been object of scientific publications:

1. Beyond the Effect of Particle Size: Influence of CoFe2O4 Nanoparticle Arrangements on Magnetic Properties

D. Peddis, **G. Muscas**, C. Cannas, A. Musinu, A. Ardu, F. Orrù, D. Fiorani, S. Laureti, D. Rinaldi, G. Piccaluga.

Chemistry of Materials

http://pubs.acs.org/doi/abs/10.1021/cm303352r

2. Magnetic Properties of Small Magnetite Nanocrystals

G. Muscas, G. Concas, C Cannas, A. Musinu, A. Ardu, F. Orrù, D. Fiorani, S. Laureti, D. Rinaldi, G. Piccaluga, and D. Peddis

The Journal of Physical Chemistry C

http://pubs.acs.org/doi/abs/10.1021/jp407863s

3. Tuning the size and shape of oxide nanoparticles by controlling oxygen content in the reaction environment: morphological analysis by aspect maps

G. Muscas (corresponding author), G. Singh, W. R. Glomm, R. Mathieu, P. Anil Kumar, G. Concas, E. Agostinelli and D. Peddis

Chemistry of materials

http://pubs.acs.org/doi/abs/10.1021/cm5038815

4. Structural and Magnetic Properties of MnFe2O4 Nanoparticles Synthesized by Solvothermal Method

B. Aslibeiki, P. Kameli, M. Ehsani, H. Salamati, **G. Muscas**, E. Agostinelli, V. Foglietti, S. Casciardi, and D. Peddis

The Journal of Physical Chemistry (under review)

5. Designing new manganite/ferrite nanocomposites with tunable magnetic and electrical properties

G. Muscas, P. Anil. Kumar, G. Barucca, G. Concas, G. Varvaro, R. Mathieu and D. Peddis
Physical Review B (under review)

6. Chemical tuning of the magnetic properties of spinel oxide nanoparticles

G. Muscas, N. Yaacob, G. Concas, J.M. Greneche, C. Cannas, A. Musinu, V. Foglietti, S. Casciardi, C. Sangregorio and D. Peddis
Nanoscale (submitted)

7. Competition of single particle anisotropy and interparticle interaction energy in ensembles of mixed Cobalt-Nickel ferrite nanoparticles

G. Muscas, G. Concas, C. Cannas, A. Musinu, A. M. Testa and D. Peddis
In preparation

Contributions in articles preparation:

1. Part of magnetic characterization and data analysis.
2. All Magnetic characterization and data analysis, manuscript preparation.
3. Synthesis, structural characterization (XRD), magnetic characterization, all data elaboration, development of the "aspect map" analysis method and manuscript preparation.
4. Structural characterization (FT-IR and TGA-SDTA) and modeling of particles aggregates.
5. Synthesis, structural characterization (XRD), magnetic and magneto-transport characterization, all data elaboration and manuscript preparation.
6. Synthesis, structural characterization (XRD, TGA, IR), part of the magnetic measurements, all data elaboration and manuscript preparation.
7. Synthesis, structural characterization (XRD, TGA, IR) part of the magnetic measurement, all data elaboration and manuscript preparation.

Contribution to conferences

Joint European Magnetic Symposia 2012 (JEMS '12), September 9-12, 2012, Parma, Italy

1) Poster communication:
D. Peddis, A. Musinu, C. Cannas, A. Ardu, F. Orrù,
G. Muscas, G. Piccaluga.
Interparticle interactions and magnetic anisotropy in cobalt ferrite nanoparticles: influence of molecular coating.

2) Oral communication:
G. Muscas, F. Orrù, N. Yaacoub, J. M. Greneche, A. Musinu, C. Cannas, A. Ardu, G. Piccaluga, D. Rinaldi, G. Concas, D. Fiorani, D. Peddis,
Magnetic properties of spinel iron oxides nanoparticles

"La parola ai giovani", September 19, Sassari, 2012, Italy

3) Oral communication:
G. Muscas, G. Piccaluga, A. Musinu, C. Cannas, A. Ardu, F. Orrù, G. Concas, D. Peddis
Tuning Magnetic Properties of Spinel Ferrite Nanoparticles with Chemical Composition

8th International Conference on Fine Particle Magnetism ICFPM 2013, June 24-27, 2013, Perpignan, France

4) Poster communication:
D. Peddis, E. Agostinelli, D. Fiorani, G. Muscas, D. Rinaldi, G. Ennas, A. Scano and G. Concas.
Superparamagnetic blocking and superspin-glass freezing in ultra-small $\delta(Fe_{0.67}Mn_{0.33})OOH$ particles

5) Poster communication:
D. Peddis, F. Orrù, A. Ardu, A. Musinu, G. Piccaluga, C. Cannas, G. Muscas and G. Concas.
$CoFe_2O_4$ and $CoFe_2O_4$/ SiO_2 Core/Shell Nanoparticles: a Magnetic Investigation

6) Poster communication:

D. Peddis, A. Musinu, C. Cannas, A. Ardu, F. Orrù, G. Piccaluga G. Muscas and G. Concas.

Beyond the effect of particle size: influence of $CoFe_2O_4$ nanoparticles arrangements on magnetic properties

7) Poster communication:

D. Peddis, D. Fiorani, S. Laureti, G. Muscas, G. Concas, C. Cannas, A. Musinu, A. Ardu, F. Orrù, G. Piccaluga and D. Rinaldi.

Interactions and Magnetic Anisotropy in Cobalt Ferrite nanoparticles: influence of molecular coating

8) Poster communication:

G. Muscas, G. Concas, A. Musinu, C. Cannas, A. Ardu, F. Orrù, G. Piccaluga, N. Yaacoub, J.M. Greneche, D. Rinaldi, D. Fiorani and D. Peddis

Magnetic Properties and surface effects of spinel iron oxide nanoparticles nanoparticles.

4th International Conference on Superconductivity and Magnetism ICSM 2014, April 27 - May 2, 2014, Antalya, Turkey

9) Oral communication:

D. Peddis, A. Musinu, C. Cannas, A. Ardu, F. Orrù, G. Piccaluga G. Muscas and G. Concas.

Interactions and Magnetic Anisotropy in Cobalt Ferrite nanoparticles: influence of molecular coating

4th Italian Conference on Magnetism MAGNET 2015, February 16-18, Bologna, Italy

10) Poster contribution:

G. Muscas, G. Concas, C Cannas, A. Musinu, A. Ardu, F. Orrù, D. Fiorani, S. Laureti, D. Rinaldi, G. Piccaluga, and D. Peddis

Magnetic Properties of Small Magnetite Nanocrystals

11) Oral contribution:

G. Muscas, R. Mathieu, P. Anil Kumar, G. Concas, G. Varvaro, C. Cannas, A Musinu, and D. Peddis

Advanced Multiferroic Nanocomposite

School, seminars and workshops

Between February 25th and March 8th 2013 I have attend the European School on Magnetism in Cargèse, France. In the internal conference organized by the school, I have presented the posters contributions titled "*Beyond the effect of particle size: influence of $CoFe_2O_4$ nanoparticles arrangements on magnetic properties"* and "*Interactions and Magnetic Anisotropy in Cobalt Ferrite nanoparticles: influence of molecular coating"*

During my stay at Uppsala University, I have presented the talk *Interactions and Magnetic Anisotropy in Cobalt Ferrite nanoparticles: influence of molecular coating* at the Workshop Magnetic nanoparticles and superspinglass (March 25th, 2013).

During the visit at the Institute of Structure of the Matter of CNR, I have presented part of my work in the seminar *Nanostructured Magnetic Oxides* (May 21st, 2014).

List of symbols and acronyms

μ = Magnetic permeability [T m A^{-1}]

μ_0 = Vacuum magnetic permeability ($4\pi \cdot 10^{-7}$ T m A^{-1})

μ_R = Relative magnetic permeability [T m A^{-1}]

μ_B = Bohr magneton ($9{,}274 \cdot 10^{-24}$ J T^{-1})

ρ = Resistivity [Ω m]

χ = Magnetic susceptibility (unit less)

χ_d = Magnetic susceptibility of high anisotropy component (unit less)

B = Magnetic flux density [T]

DCD = DC Direct demagnetization remanence curve

E_a = Anisotropy energy

FC = Field Cooling

FiM = Ferrimagnetism

FM = Ferromagnetism

FT-IR = Fourier Transform Infrared Spectroscopy

H = Magnetic field strength [A m^{-1}]

h= Planck costant ($6.626 \cdot 10^{34}$ J s).

$\hbar$ = Reduced Plank constant ($1.0546 \cdot 10^{34}$ J s).

$\mu_0 H_C$ = Coercive field [T]

$\mu_0 H_K$ = Anisotropy field [T]

$\mu_0 H_{SAT}$ = Saturation field [T]

IRM = Isothermal Remanence Magnetization

K_A = Magnetic anisotropy constant

k_B = Boltzmann constant($1.381 \cdot 10^{-23}$ J K^{-1}).

l = Orbital angular momentum

m = Magnetic moment [A m^2]

M = magnetization (magnetic moment per unit of volume [A m^{-1}] or per unit of mass [A m^2 kg^{-1}])

m_e = electron mass ($9.109 \cdot 10^{-31}$ kg)

M_R = Remanent magnetization [A m^{-1}or A m^2 kg^{-1}]

M_{Red} = Reduced remanent magnetization

M_S = Saturation magnetization [A m^{-1} or A m^2 kg^{-1}]

s = Spin angular moment

SDTA = Simulaneous Differential Thermal Analysis

SFM = Super-Ferromagnetism

SPM = Super-Paramagnetism

SQUID = Superconducting Quantum Interference Device

SSG= Super-Spin-Glass

T_B = Superparamagnetic blocking temperature

T_C = Curie temperature

T_g = Spin glass transition temperature

T_{irr} = Irreversibility temperature between ZFC and FC curves

T_{max} = Temperature corresponding to the maximum in ZFC curve

T_N = Néel temperature

T_V = Verwey transition temperature (≈ 120 K).

TEM = Transmission Electron Microscopy

TGA = Thermo-gravimetric analysis

VSM = Vibrating Sample Magnetometer

XRD = X-ray diffraction

ZFC = Zero Field Cooling

Introduction

Magnetic materials have been fascinating human beings for over 4000 years. Since an ancient Greek shepherd noticed in Magnesia that the iron nails in his shoe and the iron tip of his staff stuck to certain rocks (Lodestone) [1], the magnetic phenomena have been object of careful study and it is still common opinion that "*few subjects in science are more difficult than magnetism"* [2]. Nowadays, the magnetic materials have found their way into almost every part of our civilization. In our modern society, we use magnetic materials daily, such as computer hard disk, credit and ID cards, loud speakers, refrigerator door seals and a host of other conveniences. The development of new materials on smaller and smaller length scale has been at the root of progress in material science in the last 40 years. This is particularly true in the development of new magnetic materials: the discovery of giant magnetoresistance (GMR) in magnetic thin films [3,4] and subsequently the observation of GMR in small granular systems of Fe, Co, and Ni and their various alloys in Cu, Ag or Au matrices [5] are examples of such development.

Broadly speaking, the physical properties of a material are size dependent, being the results of phenomena which occur only at a specific size-scale [6,7]. On entering the nanometer-scale regime the magnetic properties of condensed matter show substantial differences with respect to the bulk state, leading *to new physics* [8–10] and applications [7,11]. In magnetism, several phenomena are related to nanoscale, such as the dimensions of magnetic domains or the length of exchange coupling interactions. For this reason, since a few decades ago, nanostructured magnetic materials are object of a great attention, with the aim to control systems constituents in the range 1 - 100 nm to design their magnetic properties. Among nanostructured magnetic materials, nanoparticles (NPs) are unique complex physical objects: in these systems a multidomain organization is energetically unfavorable and single-magnetic-domain particles are formed, each one with a huge magnetic moment with comparison to that of single atoms, thus they are often named "supermoment" [6]. In addition, the attractive performance of magnetic NPs based materials are appealing for several technological field as nanomedicine [12] (e.g., magnetic sensors [13], bio-imaging [14,15], drug delivery [16,17] therapeutic hyperthermia [18–20]), ferrofluid technology [21], catalysts [22,23], color imaging [24], and high density magneto recording [25,26].

Furthermore, iron oxide nanoparticles (Fe_3O_4, γ-Fe_2O_3) play an important role in nature; indeed, they are commonly found in soils and rocks and they are also important in several ways for the functioning of living organisms [8,27].

In this framework, understanding the physics of magnetic nanoparticles and controlling their magnetic properties represent hot topics for both fundamental studies and technological applications. Generally speaking, the energy of a magnetic particle can be considered dependent on the *magnetic anisotropy energy* (MAE). According to the Néel−Brown theory, above a certain temperature (the blocking temperature T_B) and on a certain time scale, the particle magnetic moment can produce a thermally activated transition. This behavior is analogous to paramagnetism, but with different time and magnetization scale, for this reason, it is called "superparamagnetism" (SPM). For a given experimental measuring time τ_m, a corresponding T_B is defined, below which the particle's moment rotate over the barrier in a time longer than τ_m, thus it appears as blocked. In addition, the behavior of a random ensemble of nanoparticles depends on the type and strength of interparticle interactions, evolving from paramagnetic (PM)-like to ferromagnetic (FM)-like, including a spin-glass (SG)-like behavior. Due to the enhanced time and magnetization scale with respect to atomic systems, the magnetism of nanoparticle ensembles has been often called *supermagnetism* [6,28].

Beyond the effect of particle volume and the influence of magnetic interactions, the tuning of the magnetic properties of nanoparticles means control of the magnetic anisotropy energy. For bulk materials, the MAE depends mainly on structure and chemical composition (i.e., magnetocrystalline anisotropy); for nanoparticles other factors, such as particle shape (i.e., shape anisotropy) and surface to volume ratio (i.e., surface anisotropy) have to be taken into consideration as well. Furthermore, in nanoparticle ensemble, the MAE may differ from one particle to another, due to the presence of physical and/or chemical inhomogeneity; therefore, the macroscopic measured anisotropy will be a type of weighted average of the single particles anisotropy. Thus, in order to design magnetic nanostructured materials suitable for several applications, it will be essential to control the distribution of MAE, that is, particle shape, size, and size distribution and chemical homogeneity [6,7].

The anisotropy arising from the coupling of two magnetic phase, i.e., the exchange anisotropy [29,30], becomes a new tool in order to tailor the magnetic properties at the nanoscale. Such exchange coupling (EC) is already at the bases of new multiphase compounds, which find applications in several fields, from permanent magnets, to magneto-recording, microwave adsorption or biomedical applications [31].

The aim of this PhD project was to investigate and tune particle MAE modulating magnetic properties of NPS ensembles. This study has been mainly performed on spinel

iron oxide nanoparticles: these materials are good models systems for studies of the relationship between magnetic behavior and magnetic structure at atomic level, owning structural properties and a rich crystal chemistry, which offer excellent opportunities for fine tuning and understanding their magnetic properties [32–34].

A detailed description of the experimental work and of the data rationalization will be given on this thesis by chapters organizations.

Chapter 1 will briefly introduce the magnetism of nanoparticles, in order to highlight the key elements to understand the role of the MAE in the physics of these systems. Furthermore, it will discuss how to tune the MAE at the nanoscale showing the main parameters that can influence the anisotropy itself, defining the framework within the synthetic strategies used in this work have been developed.

The surface component of MAE is strictly dependent on particles volume (i.e., surface/volume ratio). In this view, ***Chapter 2*** will discuss the influence of the particles size on a scale of few nm (5-10 mm), with the analysis of four ensembles of maghemite (γ-Fe_2O_3) nanoparticles. It will be demonstrated that on such size scale the influence of the surface anisotropy plays a fundamental role in characterizing the magnetic behavior. Particular attention will be devoted to understand the contribution of the local surface anisotropy and its origin in terms of non-collinear spin structure. Finally, some insights about the use of suitable molecular coating to tune single particle MAE will be discussed.

Within this analysis, it emerges the fundamental role of particles morphology (i.e., size and shape) and its distribution to tune the MAE. Indeed, for applications ranging from electronics to biomedicine, one of the key points to improve the system efficiency is to have narrow distribution of size and shape, in order to minimize the different magnetic anisotropy among nanoparticles. ***Chapter 3*** will introduce a semiautomatic procedure for a very detailed statistical analysis leading to the development of a new tool to investigate particles morphology, called “aspect maps”. This new instrument allows analyzing morphology of NPs assemblies with an higher resolution with compared to usual statistical procedures reported in literature. Its potentialities have been used to improve the high temperature thermal decomposition process of metalorganic precursor. Cobalt ferrite nanoparticles have been chosen as model system to prepare high quality colloidal magnetic nanoparticles with controlled morphology. As a main result of such study, it will be shown how a narrow particle size distribution reflects a more homogenous magnetic response of the nanoparticles.

One of the most intriguing way to tune the magnetic anisotropy of a material is to control its physical-chemical structure. ***Chapter 4*** will face the role of the chemical

composition in determining the magnetocrystalline anisotropy in nickel-doped cobalt ferrite nanoparticles; it will be analyzed its influence on the effective MAE and the magnetic structure of NPs.

The interparticle interactions can own a strong influence on NPs superparamagnetic relaxation process, up to induce collective magnetic behaviors, i.e., superspinglass (SSG) and superferromagnetism (SFM). ***Chapter 5*** will introduce the analysis of the interparticles interactions on ensembles of spinel iron oxides with the same morphological structure but different MAE due to the different chemical composition. The process of magnetization reversal will be studied in both the low and high field regime, analyzing the competitive role of interparticles interactions and single particle MAE employing a modified random anisotropy model (RAM).

Nowadays, one of the most appealing field in magnetic material development is to design nanostructured composites. They allow combining the properties of two or more materials to improve it or to introduce entirely new ones. ***Chapter 6*** will present novel approaches to create nanocomposites in order to design structures in which improve magnetic interactions among their constituents. In addition it will be studied the effect of such structures on the magneto-transport properties of manganese oxides. Different nanocomposites structures will be obtained mixing cobalt ferrite nanoparticles with calcium doped lanthanum manganese oxides. This compound represent a typical strongly correlated transition metal oxide well studied for its magnetoresistance properties for several technological application, e.g., the tunnel magnetoresistance effects. Both materials can be considered an optimum starting point for the development of nanostructures, which later can be extent to other materials.

In ***appendix*** to this thesis, it will be reported a detailed description of manganites with an in-depth analysis of magnetic and magnetoelectric protocols of measurements employed for these studies.

Chapter 1
Nanomagnetism

The breakthrough point for magnetic materials occurs when their constituents undergo a critical radius. In such case, their configuration of minimal energy is the one with all atomic moments aligned in the same direction. Such critical radius r_C is typical for each material and in the range of nanometers:

$$r_c \approx 9\frac{(AK_u)^{\frac{1}{2}}}{\mu_0 {M_S}^2} \quad (1.1)$$

where A is the exchange constant, K_u the constant for magnetic uniaxial anisotropy and μ_0 the vacuum magnetic permeability. Typical values of r_C are 15 nm for Fe, 35 nm for Co, 30 nm for γ-Fe_2O_3 , 55 nm for Ni, and 750 nm per $SmCo_5$ [28]. Such particles act as single magnetic domains with a compressive magnetic moment in the range 10^3-10^5 μ_B. They are similar to atomic moments in paramagnetic materials, but with a much larger magnetization magnitude and a specific time scale for magnetization reversal; for this reason they are often defined as *superspins*, and their magnetic behavior can be described as *supermagnetism* [28].

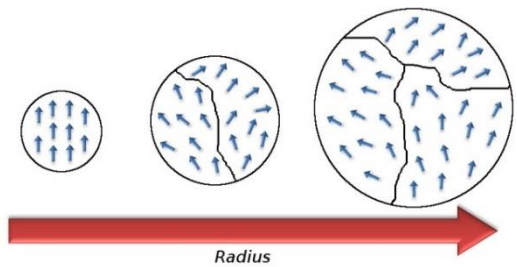

Figure 1.1: Magnetic Domain configuration with respect particles size.

1.1 Magnetic anisotropy energy

In order to align the magnetization of a superspin, it is necessary to overcome a magnetic anisotropy energy barrier. This anisotropy describes the dependence of the internal energy to the direction of magnetization orientation, introducing the concept of easy and hard directions of magnetizations. There are several sources of anisotropy, and its effective value determinates in large part the magnetic behavior of a material. On nanoscale, the two most important contribution are the magnetocristalline and the surface ones. In particular, on a very low size scale (i.e., under 10 nm), due to the increasing surface to volume ratio, the surface contribution acquires a primary role, sometimes overcoming the magnetocrystalline one.

1.1.1 Magneto-crystalline anisotropy

This anisotropy is deeply related to the crystalline structure and its symmetry, and it is an intrinsic property of a material [35]. The simplest conditions is represented by a spherical particle with uniaxial anisotropy, i.e., a single direction (easy axis) in which the alignment of the magnetization is favored.

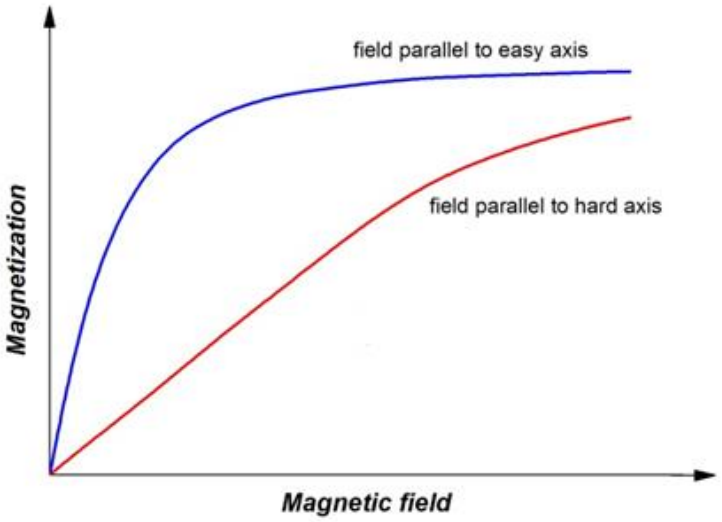

Figure 1.2: Examples of magnetization curves measured with the magnetic field applied parallel to an easy and a hard axis.

To switch the magnetization between the parallel to the antiparallel orientation is necessary to overcome the magneto-crystalline anisotropy energy defined as:

$$E_a^{uni} = K_1 V \sin^2\theta + K_2 V \sin^4\theta + \ \ldots \ \approx \ KV \sin^2\theta \qquad (1.2)$$

where the anisotropy constant *K* can be approximated to K_1, being $K_1 >> K_2, K_3$, … , *V* is the particle volume and θ represents the angle between the easy axis and the magnetization.

The first source of magnetocrystalline anisotropy is the single ion contribution. For a specific atomic site, the crystal field tends to stabilize a specific orbital. Due to the spin-orbit coupling this effect translates in a specific orientation of spins long a given crystallographic orientation [36]. A second contribution arises from the dipolar coupling among moments, which tend to align head to tail, owing such configuration the minimal energy. The dipole sum has to be extended to the whole lattice, and for certain lattices (e.g., all cubic ones) it can vanish [35,37].

1.1.2 Shape anisotropy

For a sample with magnetization M_i along a specific axis *i*, a corresponding internal magnetization field H^d_i can be defined:

$$H_i^d = -N_i M_i \qquad (1.3)$$

where N_i is the demagnetizing factor along that axis. For a sphere, the *N* factors are equal to 1/3 in all *x*-*y*-*z* axis, resulting in a isotropic demagnetization field, thus, no shape anisotropy appears.

For particles with elongated shape, a smaller demagnetizing field emerges for the long axis, due to the larger distance of the two magnetic poles, induced at particles surface. Thus, for a general uniform magnetized ellipsoid of revolution around the *z* axis

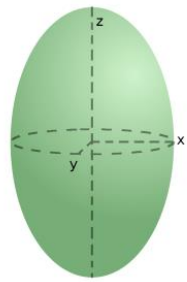

Figure 1.3: Ellipsoid with revolution z axis

(**figure 1.3)**, the difference in energy when the ellipsoid is magnetized along its hard and easy directions represents the shape anisotropy E_a^{shape}:

$$E_a^{shape} = \frac{1}{2}\mu_0 V M_S^2 (N_z \cos^2\vartheta + N_x \sin^2\vartheta) \qquad (1.4)$$

where the $N_x = N_y$, and N_z represent the demagnetization factors and M_S the saturation magnetization.

1.1.3 Strain anisotropy

A further anisotropy energy can come from a stress applied to a material that can modify its magnetic structure. Similarly, an external applied field can induce a distortion in the crystalline structure, modifying the shape of the crystal. Such anisotropy energy can be defined as:

$$E_a^{strain} = -\frac{3}{2}\lambda_S \, \sigma \, S \cos^2\theta' \qquad (1.5)$$

where λ_S is the saturation magnetostriction, σ the strain value by surface unit, S the particle surface and θ' the angle between the magnetization and the strain tensor axis.

1.1.4 Surface anisotropy

The breaking of the symmetry at particles surface reduces the nearest neighbors' coordination leading to a different local magnetocrystalline anisotropy. Reducing particles size, the surface on volume ratio increases, thus smaller particles manifest larger effect of surface anisotropy. For the simple case of small spherical particles with diameter d, the effective anisotropy constant can be defined as:

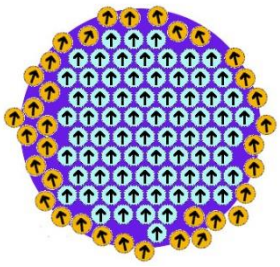

Figure 1.4: Graphical sketch of surface disorder of magnetic moments.

$$K_{eff} = K + \frac{6}{d}K_S \qquad (1.6)$$

where K represents the magnetocrystalline anisotropy constant and K_S its local surface value measured in J m^{-2}.

1.2 Superparamagnetism

An effective anisotropy energy can be defined in case of uniaxial anisotropy as:

$$E_a^{eff} = K_{eff} V \sin^2 \theta \qquad (1.7)$$

Its value reaches a minimum for the parallel and the antiparallel orientation of the magnetization with respect the easy axis, and the maximum when it is perpendicular to it (parallel to the hard axis). Such energy is related to the effective anisotropy constant of the material and grows with respect particles volume (**figure 1.5**).

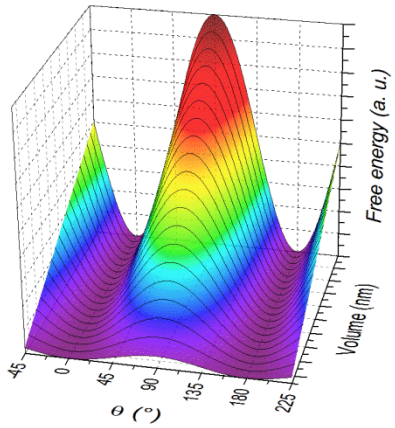

Figure 1.5: Dependence of magnetic anisotropy energy from the angle between the particle magnetization and the anisotropy easy axis. Furthermore, the dependence from particles volume is considered.

For a system of single domain particles with uniaxial anisotropy, at relative high temperature, such as the thermal energy $k_BT >> K_{eff}V$, the superspins can freely rotate and the magnetization process can be treated with the Langevin model for atomic paramagnetism. For a nanoparticle with total dipolar moment m under the influence of a magnetic field $\mu_0 H$, its magnetization M can be described as $M = M_S L(x)$, where M_S is the saturation magnetization, $L(x) = coth(x) - 1/x$ is the Langevin function, and $x = \mu_0 mH/k_BT$. Thus, for analogy, such thermal equilibrium behavior is called *superparamagnetism*.

When the thermal energy is lager but comparable to the anisotropy energy, the magnetization process significantly differs from the Langevin model [38], due to the

measurable effect of the anisotropy energy barrier (**figure 1.5**). The magnetostatic energy of a particle with superspin moment *m* can be defined as:

$$E_m = -\left(K_{eff}V\right)\cos^2\theta - \mu_0\vec{m}\cdot\vec{H} \qquad (1.8)$$

The switching between the two energy minima happens with a given frequency (*f*) which correspond to a relaxation time ($\tau = 1 / (2\,\pi\, f)$) described by the Néel-Brown relation [39,40]:

$$\tau = \tau_0 \exp\left[\frac{K_{eff}V}{k_B T}\right] \qquad (1.9)$$

where k_B is the Boltzmann constant and τ_0 represents the inverse attempt frequency. The system appears static when the superparamagnetic (SPM) relaxation time τ becomes much longer than the experimental measuring time τ_m. For a give experimental technique this two quantities becomes comparable only at a specific temperature, at which the systems appears as "blocked". The corresponding blocking temperature can be defined as:

$$T_B = \frac{K_{eff}V}{k_B\, ln(\tau_m/\tau_0)} \qquad (1.10)$$

At a temperature low enough such as $k_BT < K_{eff}V$, the magnetization reversal of a single domain particle is described by the Wohlfarth and Stoner model (WS) [41]. According to that, the free energy of the particles is related to the applied field $\mu_0 H$ and to the angles φ and θ, which the field and the particle moment *m* form with respect the easy axis, respectively (**figure 1.6)**:

$$E = K_{eff}V\sin^2\theta - m\mu_0 H\cos(\varphi - \theta) \qquad (1.11)$$

In order to reverse the magnetization from one minima to the other it is necessary to overcame an energy barrier ΔE_B . The application of an external field reduces such barrier allowing for a parallel orientation between the magnetization and the applied field. Such energy barrier is field dependent and can be defined as $\Delta E_B = KV\ (1-\mu_0 H/\mu_0 H_K)$ [42].

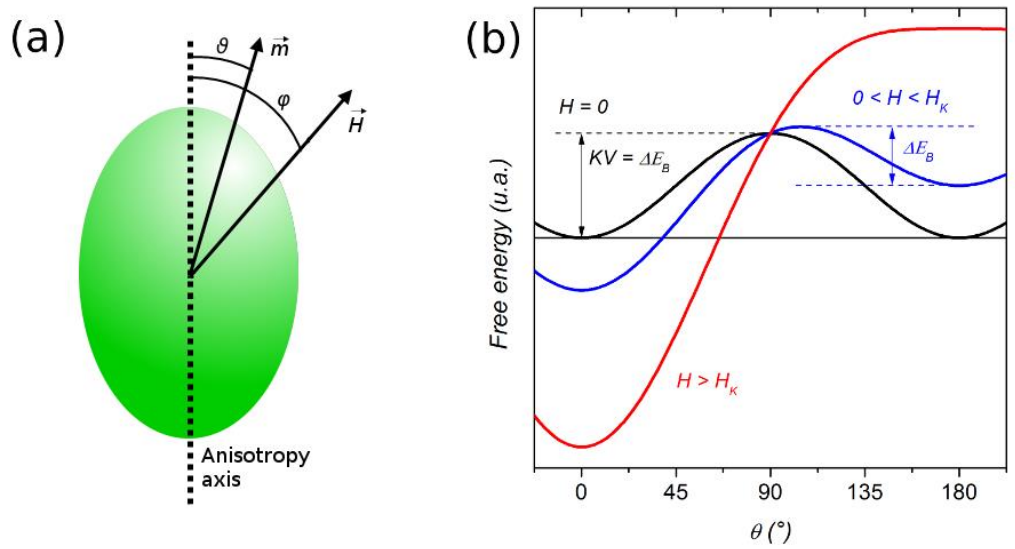

Figure 1.6: (a) Sketch of the magnetization reversal for a monodomain particle with uniaxial anisotropy with an applied field H. (b) The dependence of the free energy from the angle between the easy axis and the magnetization is reported for different applied fields.

According to the WS model the M(H) curve can show hysteresis and the reversal of the magnetization at a coercive field $\mu_0 H_C$. No hysteresis occurs for $\varphi = 90°$, while the curve shows squared shape for a field applied parallel ($\varphi = 0°$) or antiparallel ($\varphi = 180°$) to the easy axis. In this condition, the coercive field reaches its maximum value defined as the anisotropy field $\mu_0 H_K = 2K/M_S$. For an ensemble of particles with randomly distributed orientation of easy anisotropy axis, M(H) curves show hysteresis with a ratio between the remanent magnetization M_R (at H = 0) and the saturation magnetization M_S equal to $M_{red} = M_R/M_S = 0.5$. Furthermore, it is possible to identify a coercive field $H_C = 0.48\ \mu_0 H_K$ as the field necessary to reduce to zero the magnetization.

1.3 Magnetic interactions at the nanoscale

Interparticle interactions own a deep influence on the magnetic behavior of an ensemble of superspins. Such interactions can be assimilated to atomic spin interactions, replacing them with the giant moment of superspins and considering the distance among nanoparticles. Here, a brief qualitative discussion of magnetic interaction will be given, with particular attention being paid to the most important interactions at the nanoscale. A complete description of magnetic interactions in bulk and nanostructured systems can be found elsewhere [8,28,43].

For an ensemble of spins of average moment μ and average distance d, the average energy of dipolar interactions can be evaluated as:

$$E_{dip} \approx \frac{\mu_0}{4\pi}\frac{\mu^2}{d^3} \qquad (1.12)$$

In case of atoms such energy owns almost negligible values of 10^{-23} J ≈ 1 K, due to the low magnitude of the atomics moments (few μ_B), and their distance (0.1-1 nm) in the crystalline lattice. Replacing atoms with the moments of superspins (10^3 – 10^5 μ_B), and considering interparticles distances of few nm, the energy involved rises up to tens of K [43], with a deep influence on their SPM blocking temperature. A critical temperature at which a ordering can appear among nanoparticles can be estimated as:

$$T_0 \approx \frac{E_{dip}}{k_B} \qquad (1.13)$$

The influence of dipolar interaction can produce an increment in the effective anisotropy, increasing the blocking temperature of nanoparticles, inducing a kind of modified SPM behavior [28,44]. Increasing particles concentration or particle's moment, dipolar interactions increase their magnitude and a collective behavior emerges, which, due to the intrinsically anisotropic character of the dipolar interactions, leads to frustrated order (**figure 1.7**) like in a spin-glass like or superspin glass (SSG) behavior [43,45].

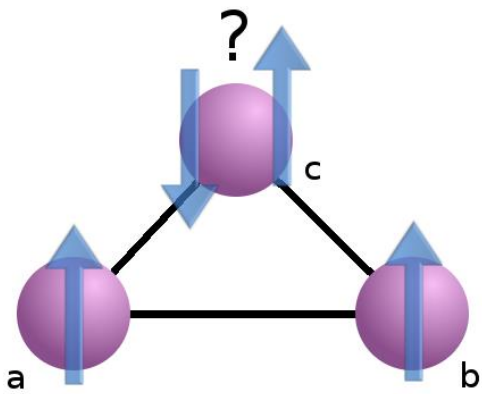

Figure 1.7: Typical example of frustration arising from a triangular arrangement of spins.

In case of particles in close contact, *exchange coupling* can occurs for surface atomic spins trough the overlapping of magnetic orbitals (direct exchange). Such effect has been observed as the origin of increment of anisotropy energy in close packed hematite nanoparticles, when the small uncompensated moment due to the AFM order cannot produce a dipolar coupling strong enough to explain such effect [46]. An exchange coupling effect can be responsible of an enhanced anisotropy in nanostructures, like AFM-FM core-shell structures or core-matrix, where this new source of anisotropy can strongly increase the blocking temperature [47]. Interparticle exchange interactions can be described by using the Heisenberg spin Hamiltonian [35,36]:

$$\mathrm{H}_{exc} = 2\sum_{i,j} J_{i,j}\,\vec{S_i}\,\vec{S_j} \qquad (1.14)$$

where $J_{i,j}$ is the exchange integral describing the magnitude of coupling between the spins $\vec{S_i}$ and $\vec{S_j}$. Such interactions are responsible for range magnetic order, in particular, superferromagnetic (SFM) behavior is expected for an assembly of strong exchange coupled superspins [28,48].

In case of particles embedded in an insulating matrix, intermediate atoms or ions (e.g., oxygen) can act like bridge for indirect superexchange interactions among magnetic atoms [35]. On the other hand, for metallic particles in a metallic matrix, RKKY (Ruderman–Kittel–Kasuya–Yosida) interactions can occurs among electrons of inner *d*

or *f* shells trough conduction electrons [49–51]. Indirect exchange interactions can manifest also by tunnel effect, but only in case of few tenths of nm among particles surface [52,53].

1.3.1 Interface Interactions

The magnetic interaction between two different phases at nanoscale represents an additional source of anisotropy, which can be exploited to modify and improve the magnetic properties, designing new composite materials. In 1956 Meiklejohn and Bean reported a new source of anisotropy arising from the interface exchange coupling between an AFM and a FM material [29]. They studied an FM/AFM core/shell structure of Co/CoO. When such system was cooled from $T_N < T < T_C$ to a temperature $T < T_N$ under an applied magnetic field, AFM spins were aligned parallel to FM spins at interface. Measuring the M(H) loop at that temperature, the exchange coupling make easier for the FM component to align parallel to the surface spins of AFM phase, requiring an higher opposite field to reverse the magnetization, and producing a loop shifted toward negative fields (**figure 1.8**).

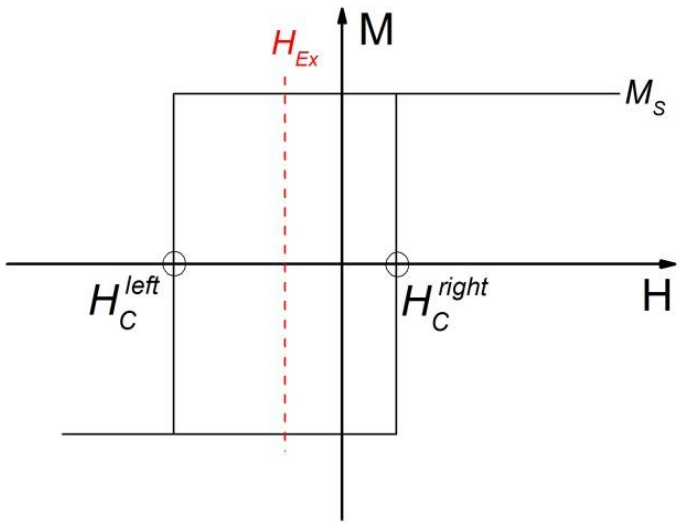

Figure 1.8: Sketch of an M(H) curve showing exchange bias after field cooling.

The field corresponding to the shifting of the loop is defined as exchange bias field (E_{ex}), which is evaluated with the relation:

$$E_{ex} = \frac{\mu_0 H_C^{left} + \mu_0 H_C^{right}}{2} \qquad (1.15)$$

where $\mu_0 H_C^{left}$ and $\mu_0 H_C^{right}$ are the coercive field measured in the negative and positive part of the field axis, respectively (**figure 1.11**). This effect have been reported to increase the anisotropy energy of a Co/CoO system embedded in a CoO matrix, up to 2 orders of magnitude [47]. Nowadays, the exchange coupled bi-magnetic hard/soft and soft/hard magnetic core/shell nanoparticles represent a strong field of interest to develop new materials. They allow to combine and improve the magnetic properties of the original materials creating new multiphase compounds which find applications in several fields, from permanent magnets, to magneto-recording, microwave adsorption or biomedical applications [31].

1.4 Tuning the magnetic anisotropy at the nanoscale

The knowledge of the nanoscale phenomena represents a bridge into the future of technological application, not only in order to improve the properties of materials but also to modulate the matter on a low level to design new ones. In this sense, tuning the anisotropy energy represents a perfect way to control the properties of a magnetic material.

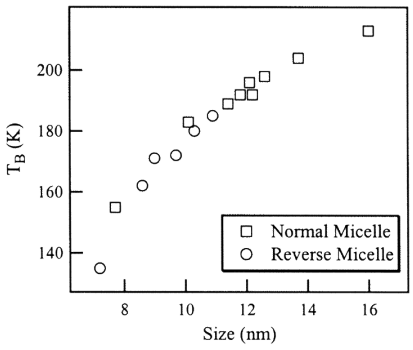

Figure 1.9: Size dependence of blocking temperature under a 0.01 T field for $CoCrFeO_4$ nanoparticles prepared by the normal and reverse micelle procedures. Reprinted with permission from C. Vestal, Z. Zhang, Synthesis of $CoCrFeO_4$ nanoparticles using microemulsion methods and size-dependent studies of their magnetic properties, Chem. Mater. (2002) 3817–3822.

http://pubs.acs.org/doi/abs/10.1021/cm020112k. Copyright © 2002 American Chemical Society.

According to the relation (1.7), particles volume owns a fundamental effect on the anisotropy energy. A wide range of wet chemistry synthesis processes have been developed to produce magnetic nanoparticles with controllable size; among them some of the most diffuse are sol−gel [54,55], micellar [56,57], hydrothermal processing [58], surfactant-assisted high-temperature decomposition techniques [59–61], and polyol process [62–64].

Often, to optimize NPs based application specific values of particles size are demanded, e.g., to optimize the hysteresis losses in magnetic hyperthermia treatments [65]. In this framework a perfect example comes from the research on materials for ultrahigh-density digital data storage [66]. In order to increase the storage density above 0.5 – 1 Tbit/in^2, monodomain nanoparticles as small as 2-3 nm are necessary. Furthermore, another fundamental aspect is to strictly control the particle size distribution; indeed to improve the signal to noise ratio (SNR) the magnetic and structural distributions must have standard deviation under 5 % [67]. Thus, the distribution of switching fields represents a crucial aspect in the synthesis of magnetic nanoparticles and more generally an accurate morphology description of magnetic nanoparticle is necessary especially for the rising interest of biomedical applications such as drug delivery [68].

All the attempts of nanotechnology devoted to device miniaturization face strong finite-size effects when reducing particle size to a few nanometer scale. On this very low size-scale, a usual increment in the effective anisotropy is observed. It is related to the surface to volume ratio, which becomes so high that the influence of the surface anisotropy can overcome the magnetocristalline component, strongly affecting the overall magnetic behavior of nanoparticles. Such anisotropic component is related to the non-collinear surface spins [69], thus, within such context, the role of organic molecules bonded on particles surface can be very important. Colloidal magnetic nanoparticles are prepared with the help of organic surfactants, which allow to produce particles with controllable size and shape [59–64]. Furthermore, they make them dispersible in a medium avoiding particles direct contact.

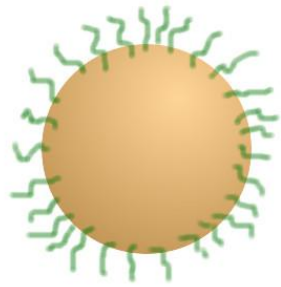

Figure 1.10: Sketch of a surfactant coated nanoparticle (e.g., oleic acid).

Anyway the role of surfactant is not limited to the synthesis process, indeed it can affect also the magnetic properties of particles, as in case of the oleic

acid, one of the most employed. It bonds at particles surface (**figure 1.10**) through the carboxylic group, restoring the local coordination of surface cations and providing a crystal field splitting energy that reduces the spin-orbit coupling and so the local surface anisotropy [70]. Such effect can be large enough to modify the whole particle anisotropy [71], furthermore it can also induce a larger saturation magnetization [72,73].

Among nanoparticles synthesis processes the high thermal decomposition of metalorganic precursors is widely diffused. It is employed to produce high crystalline particles in a wide range of size, with a narrow size distribution, furthermore controlling particles shape [74–76], which can get a fundamental role in magnetic properties of nanoparticles. Cubic and spherical particles own isotropic demagnetizing factors in the three dimensions, so there is no source of shape anisotropy, anyway the breaking of the crystalline symmetry induces surface defects in the magnetic structure at a different degree for the two shapes, leading to a greater magnitude of surface anisotropy for spherical particles [76–78] (**figure 1.11**). As result, a larger effective anisotropy is exhibited by spherical particles compared to cubic ones, considering particles with the same volume [78].

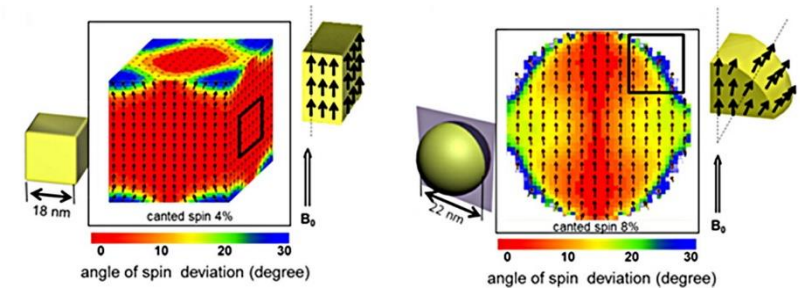

Figure 1.11: Simulated magnetic spin states of cube (left) and sphere (right) by using OOMMF program. The color map indicates the degree of spin canting with respect the external magnetic field B_0. Cube and sphere exhibits a canted spin rate of 4% and 8%, respectively. Reprinted with permission from S.-H. Noh, W. Na, J.-T. Jang, J.-H. Lee, E.J. Lee, S.H. Moon, et al., Nanoscale magnetism control via surface and exchange anisotropy for optimized ferrimagnetic hysteresis, Nano Lett. 12 (2012) 3716–21. doi:10.1021/nl301499u. Copyright © 2012 American Chemical Society.

Several experimental and theoretical studies have demonstrated that interparticle interactions own a strong influence on nanoparticles SPM relaxation process [79–81]. The progress in nanotechnology pass through the continuous miniaturization of devices, producing highly concentrate systems in which interparticles interactions are enhanced. Within this framework, an increasing interest is devoted in understanding the physics of interacting ensembles of magnetic particles in terms of interplay between the single particle anisotropy and the interparticle interctions energy [45], in order to design optimal systems for specific applications.

In most of the applications of magnetic nanoparticle-based materials (e.g., magnetic recording, energy transformation), the most important requirement is that the nanoparticles maintain their magnetization stable with time and temperature. However, with decreasing particle size, the magnetic anisotropy energy becomes comparable to the thermal energy, and superparamagnetic relaxation occurs. In this regard, *beating the superparamagnetic limit* [47] becomes fundamental to design material for specific applications, e.g., to design materials for high-density magneto-recording. The increase in areal bit density implies a concomitant reduction of the bit size maintaining at the same time a sufficient signal-to-noise ratio (SNR). This means to produce the individual grains that constitute a given bit approaching the superparamagnetic limit. To obtain a high thermal stability, a high uniaxial anisotropy is desired, but it is limited by the resulting magnetic fields required for switching the bit magnetization, which cannot exceed the capabilities of current write heads. As described in **1.3.1**, the exchange interactions between different magnetic phases (FM-FiM/AFM), induce a further term of anisotropy, which can be employed to tune the magnetic behavior. Indeed, to face the high density magnetorecoding problem, new exchange-coupled composites have been proposed [82]. In particular, coupling soft/hard material, can represent a useful approach to reduce the coercive field while preserving the thermal stability of the magnetization, as recently proposed by micromagnetic simulations [83].

Chapter 2
The volume and surface effects on magnetic nanoparticles

For the simplest case of spherical particles with uniaxial anisotropy, the MAE can be defined by the relation:

$$E_a^{eff} = K_{eff} V \sin^2 \theta \qquad (1.7)$$

Several authors have shown the dependence of the anisotropy energy by the average particles size [84], anyway, a careful analysis is necessary when particles size are reduced to few nanometers (diameter < 10 nm) and the surface to volume ratio has a great increment (**figure 2.1**). In particular, below the 5 nm limit, the surface contribution can overcome the bulk magnetocrystalline one resulting the main agent in characterizing the particles anisotropy.

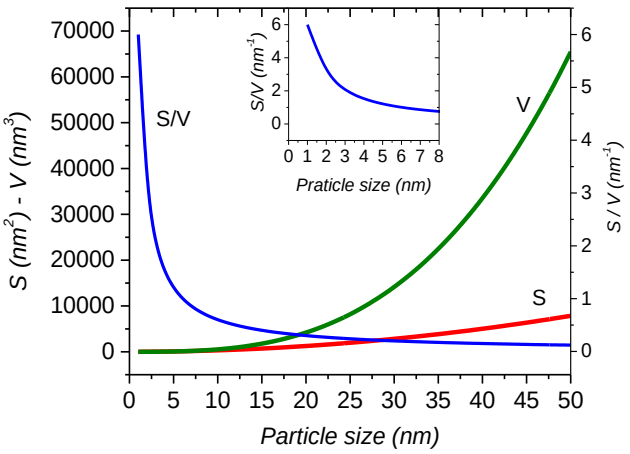

Figure 2.1: Assuming nanoparticles with spherical shape, their surface (S) and volume (V) are calculated and plotted as function of the particle diameter.

When particles surface becomes so influent, the surfactant acts a main role on magnetic behavior. It can be effective in protecting particles from oxidation, solubilize particle in specific solvent, or to functionalize them for specific porpoises, but furthermore it can be able to reduce the magnetic disorder arising at particle surface due to the incomplete coordination of cations [70,85,86].

2.1 Evolution of magnetic anisotropy with respect particles size

To analyze the effect of particles size on the magnetic behavior of nanoparticles ensembles, 3 spinel iron oxides samples have been prepared by high temperature thermal decomposition (HTD) of acetylacetonate precursors [87–89]. These samples have been synthetized with average particles size in the range 4 - 8 nm (**table 2.1**), where the surface/volume ratio owns a strong increment. In order to study the effect of a molecular shell on magnetic properties, the samples have been synthetized using an oleic acid coating. In addition, a sample with bigger particles (≈ 13 nm) was prepared without this coating, to observe both the effects of bigger size and the absence of surfactant.

2.1.1 Synthesis

To prepare 5 nm Fe_3O_4 nanoparticles iron(III) acetylacetonate (Janssen Chimica 99%, 2 mmol), 1,2-exadecanediol (Aldrich 97%, 10 mmol), oleic acid (Aldrich 90%, 6 mmol), oleylamine (Aldrich <70%, 6 mmol), and phenyl ether (Aldrich 99%, 20 ml) were mixed into a three-neck, round bottom flask and magnetically stirred. The mixture was heated gradually to 200 °C and kept at this temperature for 30 min. Then, the temperature was increased rapidly up to 300 °C, and the mixture kept for 30 min at this temperature under reflux. The starting solution changed color from orange-red to dark black, indicating the formation of the magnetite nanoparticles. The mixture was cooled to room temperature by removing the heat source. Ethanol (40 ml) was then added to destabilize the mixture, and the black product separated via centrifugation. After several washing cycles with ethanol, the powder was finally dispersed in hexane. Before magnetic measurements, the dispersion was destabilized once again with ethanol, recovered by centrifugation, and dried at 40 °C overnight to evaporate residual alcohol.

With the same method were prepared 7 nm Fe_3O_4 nanoparticles (MAG2), but using benzyl ether (20 ml) instead of phenyl ether. For this sample, the reflux time was 2 h at 200 °C and 1 h at 300 °C.

For 8 nm Fe_3O_4 nanoparticles (MAG3) the iron(III) acetylacetonate (2 mmol) was added to 84 mg of MAG2 (dispersed in hexane), to obtain a seed-mediated growth. The synthesis procedure was the same of MAG2.

For 13 nm Fe_3O_4 nanoparticles (MAG4) were used iron(III) acetylacetonate (3 mmol), oleylamine (45 mmol) and benzyl ether (15 ml). The reflux time was 1 h at 110°C and 1 h at 300 °C.

2.1.2 Structural characterization

All samples exhibit a crystalline structure compatible with iron spinel oxide (**figure 2.2**). The analysis of TEM images (**figure 2.3**) has allowed evaluating particle size distribution. In addition, MAG1, MAG2, and MAG3 samples show almost spherical particles, while MAG4 owns particles with irregular shapes. This suggest that the control on particle shape is lost without the use of surfactant.

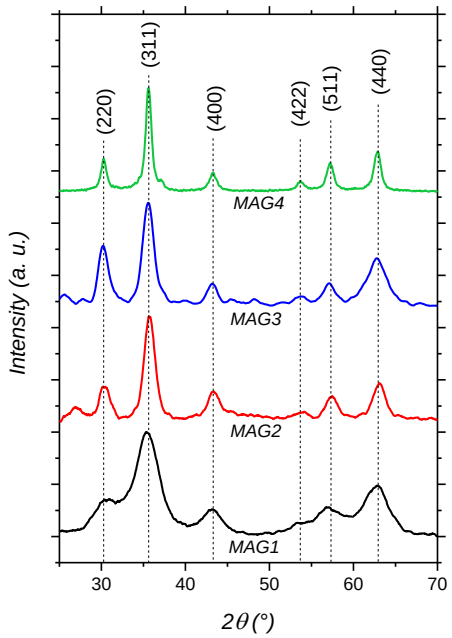

Figure 2.2: XRD pattern of the iron oxides samples prepared by HTD process.

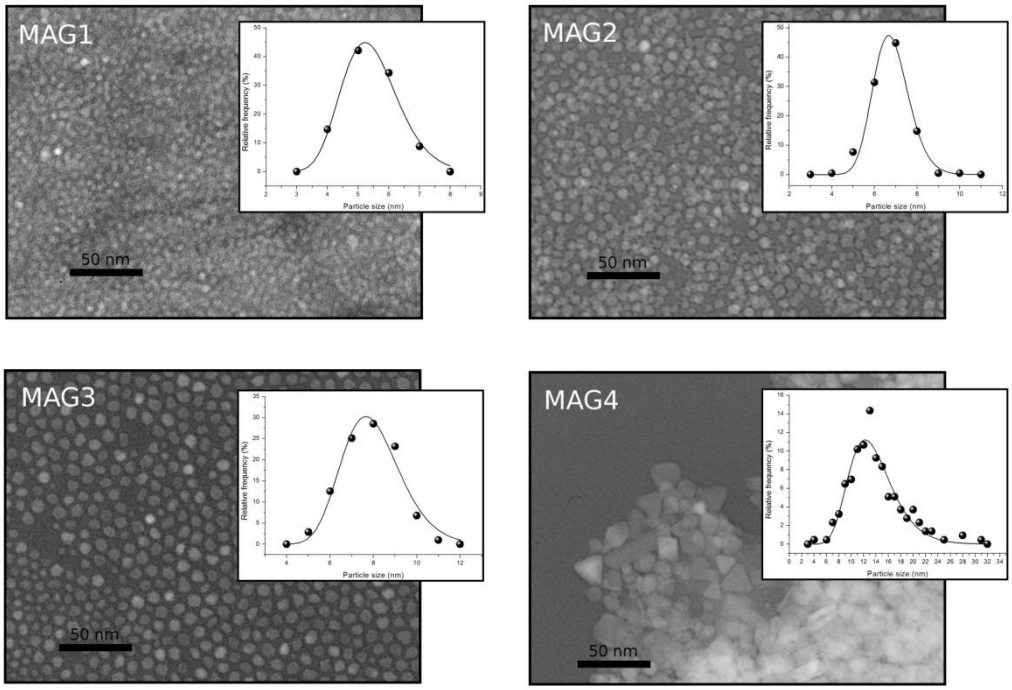

Figure 2.3: TEM images of the samples. The irregular morphology of MAG4 particles is evident. The corresponding particles size distributions are reported in inset.

Sample	***<D_{TEM}> (nm)***	***PD (nm^{-1})***
MAG1	5.4(1)	3.2(1)
MAG2	6.8(4)	1.8(1)
MAG3	7.9(1)	2.2(1)
MAG4	13.2(2)	2.1(1)

Table 2.1: Average particles diameter <D_{TEM}> and the relative polidispersity PD evaluated from TEM images.

The presence of the oleic acid (OA) in MAG1, MAG2 and MAG3 has been confirmed by FT-IR spectroscopy (**figure 2.4**). Such organic coating is reported to be attached on particles surface by a bidentate bonding trough the carboxyl groups [60].

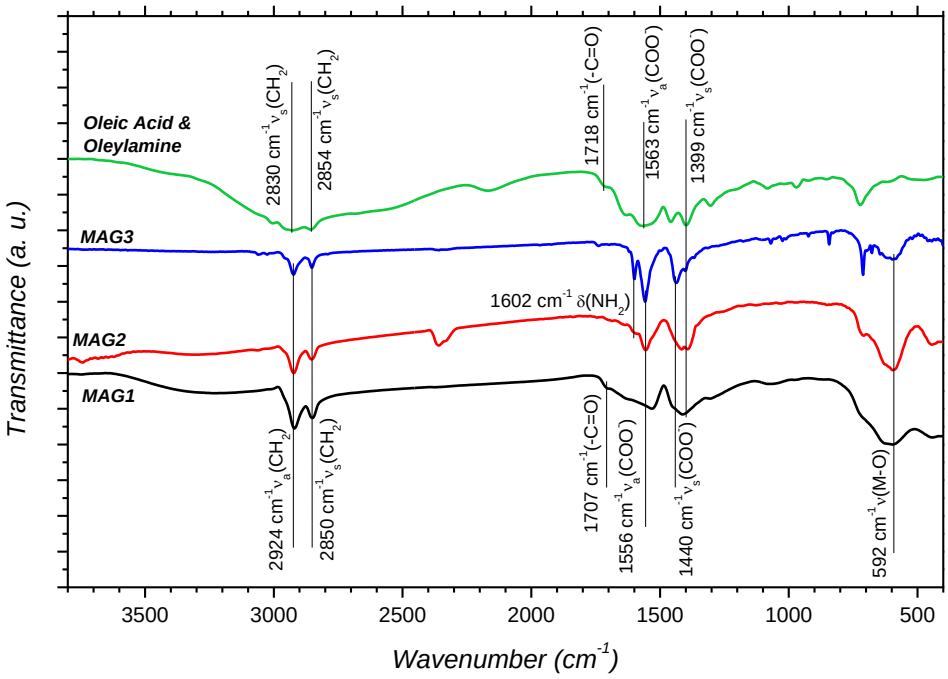

Figure 2.4: FT-IR spectra of samples MAG1, MAG2 and MAG3 confirms the presence of oleic acid coating.

2.1.3 **Magnetic properties**

The zero field cooled (ZFC) and field cooled (FC) curves (**appendix 8.2.1**), measured with an applied field of 2.5 mT, exhibit the effect of the volume on anisotropy energy (**figure 2.5**). As particles size increase from ≈ 5 to ≈ 13 nm, the temperature corresponding to the maximum of ZFC curve (T_{max}) increases. T_{max} is related to the average blocking temperature (T_B) :

$$T_{max} = \beta T_B \qquad (2.1)$$

where β is a proportionality constant, depending on the type of size distribution. For a lognormal distribution, the value of β is typically in the range 1.5-2.5 [90,91]. At the same time, the irreversible temperature between ZFC and FC curves (T_{irr}), which is associated with the blocking of the biggest particles, increases almost proportionally. We have taken T_{irr} as the temperature where the difference between M_{FC} and M_{ZFC}, normalized to its maximum value at the minimum temperature (5 K), becomes smaller than 3%. Due to its larger particles size, MAG4 T_{max} is evidently above the room temperature (maximum temperature used for these measurements).

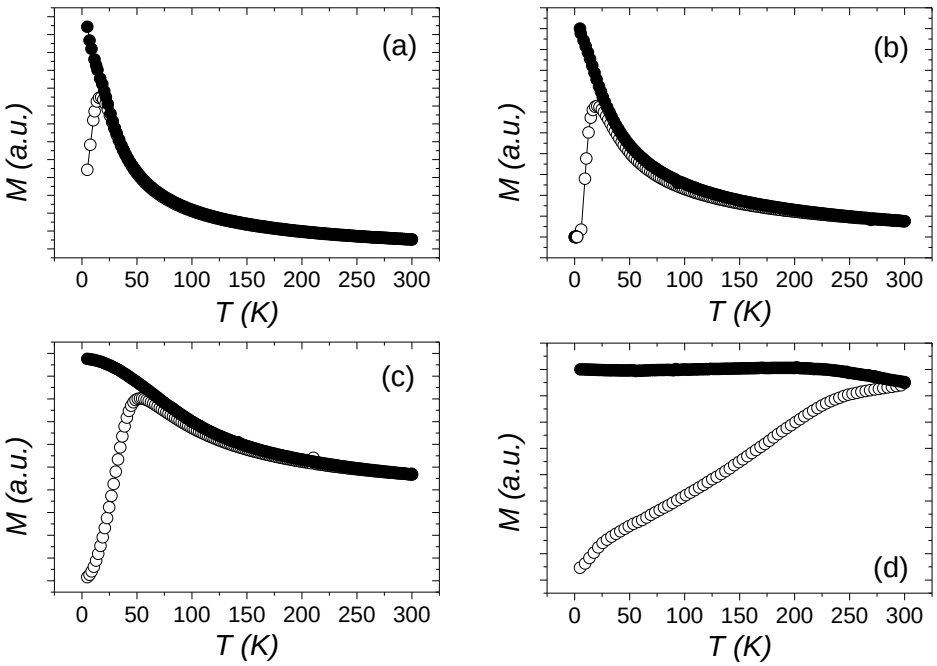

Figure 2.5: ZFC (empty circles) and FC (full circles) curves for sample MAG1 (a), MAG2 (b), MAG3 (c), and MAG4 (d), measured with an applied field of 2.5 mT.

The M Vs H curves measured at 5 K (**figure 2.6**), offer a better picture of the particles volume effect. Each particle owns an anisotropy energy produced by its volume and relative orientation of the magnetization (equation 1.7), thus for the whole ensemble it is possible to identify an average anisotropy energy. This is proportional to the

coercive field $\mu_0 H_C$, which corresponds to the field necessary to average out the magnetization of the sample.

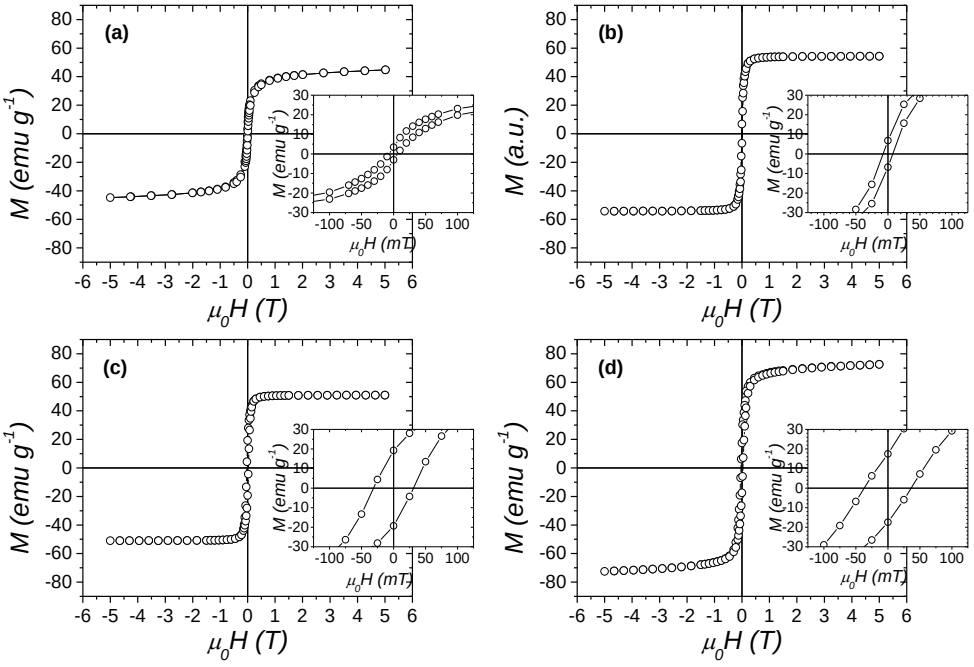

Figure 2.6: M Vs H curves measured at 5K for sample MAG1 (a), MAG2 (b), MAG3 (c), and MAG4 (d). The respective insets show a magnification at low field.

The point of irreversibility of M Vs H curves (measured as the point in which the difference between the branches is under the 1% of their maximum value) can be taken as the saturation field $\mu_0 H_{SAT}$, which can be considered as the maximum field that is necessary to apply to reverse even the moments with the highest anisotropy energy. For both the coercive and the saturation field their dependence on particles size is shown in **figures 2.7a** and **2.7b**, respectively. It is evident that the average effective anisotropy is mainly determined by the magnetocrystalline contribution, which increases according with the increment of average size (**figure 2.7a**), as observed by Roca et al. [92]. On the other hand, from the analysis of $\mu_0 H_{SAT}$ a different trend appears, with a value higher than expected for MAG1 (**figure 2.7b**). The big difference between

$\mu_0 H_{SAT}$ and $\mu_0 H_C$ values for MAG1 suggests that it owns an additional irreversible component of magnetic anisotropy.

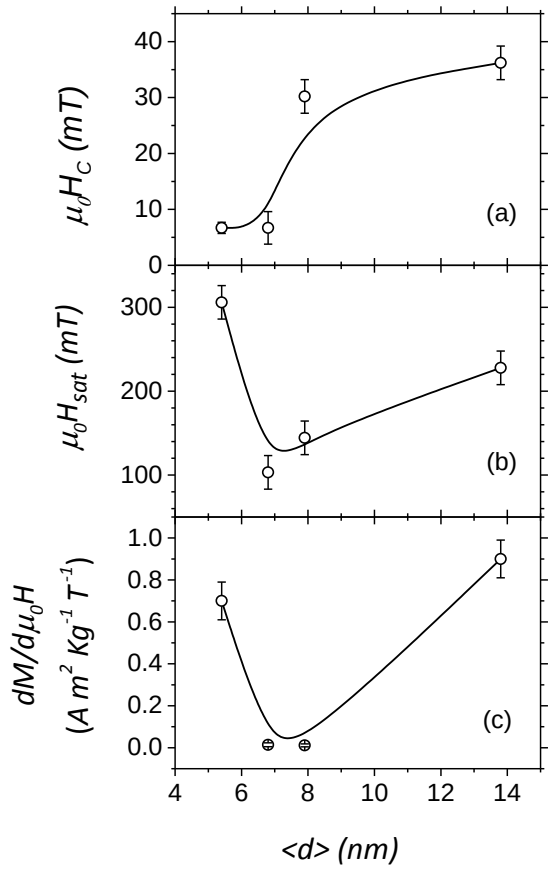

***F**igure 2.7: Particle size dependence for the coercive field ($\mu_0 H_C$), the saturation field ($\mu_0 H_{sat}$) and the susceptibility at high field evaluated by the derivative at 5 T ($dM/d\mu_0 H$) is reported in panel (a), (b) and (c) respectively.*

For better understand the origin of such component, the $dM/d\mu_0 H$ measured at 5 T has been analyzed (**figure 2.7c**). Its value can be directly related to the surface anisotropy [93] and it reproduces quite well the saturation field trend. This induces to believe that

the high magnetic anisotropy component of the samples MAG1 and MAG4, can be due to the surface anisotropy. It is known that the oleic acid bonds at particles surface through the carboxylic group and it restores the local coordination of surface cations. Furthermore, due to its nature of π-acceptor, it increases the crystal field splitting energy, thus reducing the spin-orbit coupling and so the local surface anisotropy [70]. This can explain the larger value of surface susceptibility of MAG4 with respect MAG2 and MAG3 samples, being the first synthetized only with oleylamine, which owns a donor nature with an opposite effect with respect OA [94,95]. Anyway, MAG1 is coated by OA but it evidences the largest values. In order to analize the origin of such difference, the magnetic structure has been investigated by means of Mössbauer spectroscopy.

2.1.4 The origin of surface anisotropy: Mössbauer spectroscopy to analyze surface magnetic disorder

The magnetic properties are particularly sensitive to the particle size and, on low size scale, further contributions come from finite size effects and surface effects. Magnetic atoms at the surface experiment a breaking of symmetry originating from broken exchange bonds. The symmetry breaking induces changes in the topology of the superficial magnetic moments and consequently in exchange integrals (through superexchange angles and/or distances between moments) thus leading to a specific surface anisotropy [48,96].

Mössbauer spectroscopy [97,98] represents a powerful tool to analyze the magnetic structure of iron, in addition, the application of an intense magnetic field during the experiments allows a reliable distinction between T_d and O_h Fe site components in the case of ferrimagnets [91,99,100]. The applied field is usually added to the T_d-site hyperfine field and subtracted from the O_h-site one, being negative the dominant Fermi contact term. Furthermore, in presence of an external magnetic field parallel to the γ-ray direction, the relative areas of the intermediate lines (2,5) give relevant information about the degree of alignment of the atomic Fe magnetic moment with the applied field.

The spectra have been recorded at 10 K, with a magnetic field of 8 T applied parallel to the gamma ray direction (**figure 2.8**).

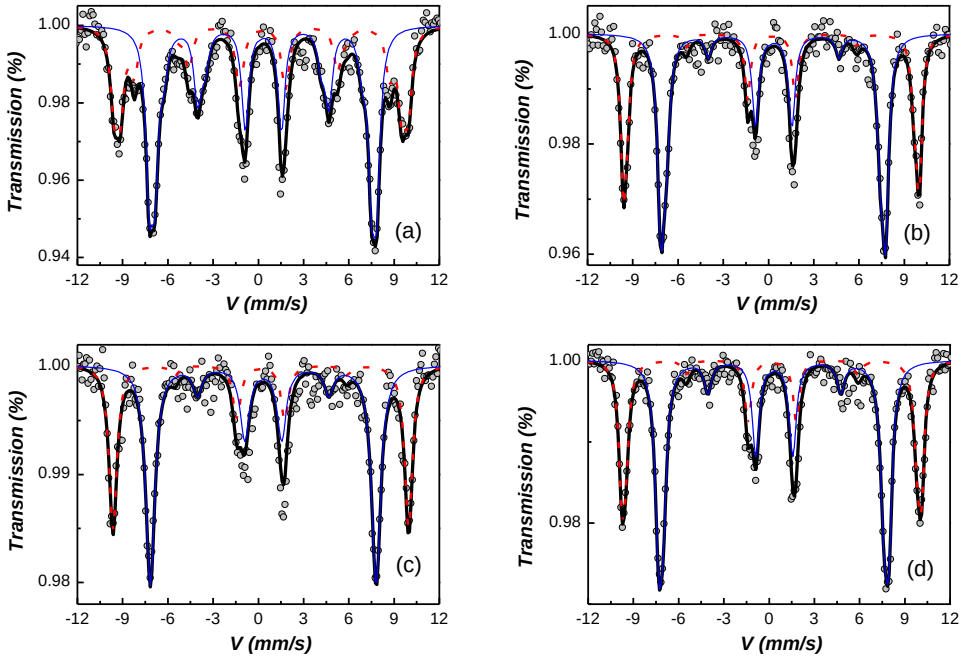

Figure 2.8: Mössbauer spectra measured at 10 K under an applied field of 8 T is reported for sample MAG1 (a), MAG2 (b), MAG3 (c), and MAG4 (d).The experimental data (circles) have been fitted with a sextet for both tetrahedral (dashed line) and octahedral (thin line) components. A bold line describes the total fit.

Under these conditions, the temperature is low enough to suppress the thermal activated magnetization switching and the spectra appear as a magnetically blocked sextet. From the modelling of the in-field Mössbauer spectra a direct estimation of both the effective field B_{eff} and the angle ϑ (angle defined by the direction of the effective field and the γ-beam direction) have been obtained for both tetrahedral and octahedral iron components, with their respective hyperfine field B_{hf}. The angle ϑ is calculated from the ratio of areas of second and fifth lines ($I_{2,5}$) on those of first and sixth lines ($I_{1,6}$). When the second and fifth lines have a non-zero intensity, they evidence a canted structure for Fe^{3+} magnetic moments with respect to the applied field (non-collinear magnetic structure) [100,101] (see **notes 2.3** at the end of the chapter for supplementary information). The lines 2 and 5 have non-zero intensity; this suggests that some of the spins is not aligned parallel or antiparallel to the external magnetic

field. Thus, being known the splitting of each component, it is possible to evaluate the average canting angle.

Sample	*Site*	δ *(mm s^{-1})*	2ε *(mm s^{-1})*	B_{eff} *(T)*	θ *(°) ±10°*	B_{hf} *(T)*	*%*
MAG1	A	0.41	-0.08	56.8	36	50.5	39
	B	0.49	-0.01	44.8	40	51.2	61
MAG2	A	0.36	-0.03	60.1	19	52.6	39
	B	0.49	-0.03	45.3	19	52.9	61
MAG3	A	0.32	0.00	60.5	17	52.9	38
	B	0.48	0.00	46.2	25	53.6	62
MAG4	A	0.33	-0.04	60.0	27	53.0	38
	B	0.49	-0.05	46.0	28	53.2	62

Table 2.2: From the fitting of Mössbauer spectra the isomer shift (δ), the quadrupole shift (2ε) the effective field (B_{eff}) the average canting angle (θ), the hyperfine field (B_{hf}) and the % area of each component are evaluated.

As reported in **table 2.2**, the hyperfine fields have values typical of maghemite for all the samples. All iron is oxidized to Fe^{3+}, and vacancies are distributed in both T_d and O_h sites in place of Fe^{2+}. All samples show some spin canting: samples MAG2 and MAG3 present similar value of canting angles, while MAG4, which is not coated by oleic acid, shows clearly larger values. Furthermore, an even larger mean angle is measured for MAG1; this explains the strong surface anisotropy of the sample.

This investigation has confirmed that the larger surface anisotropy component perfectly match with larger values of canting angles, explaining the surface anisotropy as a surface magnetic disorder effect. Furthermore, the oleic acid reduces the spin disorder in MAG2 and MAG3 with respect MAG4, but it seems to not be able to reduce the largest values of canting exhibited by MAG1, suggesting that the magnetic behavior of particles under 5 nm is dominated by the surface defects, which the oleic acid cannot completely reduce.

2.2 Case study: Using an organic coating to tune magnetic properties of $CoFe_2O_4$ nanoparticles

Nowadays the growth of technological applications asks for the device miniaturization at a scale of few nanometers. For nanoparticles with very small size (≤ 5 nm), the surface component of magnetic anisotropy becomes influent as bulk magnetocrystalline one, deeply affecting the whole behavior of a system. Nanoparticles on such scale are usually prepared trough colloidal synthesis, which make use of surfactants to obtain narrow size and shape distribution [102], to protect particles from oxidation, disperse them in specific solvents [103] or functionalize them for specific applications, as for biomedical ones (MRI, drug delivery, hyperthermia [104,105]). In addition, several authors have shown that the action of the surfactant extends also on the magnetic properties of NPs, and they have analyzed the influence of different ligands on magnetic parameters such as the coercive field [95] and the saturation magnetization [73].

Within this framework, tuning the organic coating of NPs becomes an interesting approach to manipulate the surface properties, even after the synthesis, in an exchange ligand process. Small cobalt ferrite nanoparticles has been synthetized by polyol process [6–8], in order to prepare high crystalline 5 nm particles, thus small enough to enhance the surface effects contribution. Such particles have been treated to exchange DEG with oleic acid, analyzing the different magnetic behavior produced by the two surfactants.

2.2.1 Exchange ligand process

Cobalt ferrite nanoparticles coated by diethylene glycol (DEG) were prepared by polyol process (a description of typical synthesis is reported in **4.5.1 synthesis**, where DEG is substituted by triethylene glycol, TEG). The sample was labelled as CFO-DEG.

For the exchange ligand process half of the original after-synthesis solution was taken apart in a 100 ml becker, and an equal volume of 0.2 M of oleic acid (OA) in cyclohexane was added. The two solutions were immiscible and initially the transparent oleic acid solution remained on top while the polyol with black nanoparticles formed a dark solution at the bottom (**figure 2.9a**). The solution was mechanically stirred for 24 h. After this process, the top cyclohexane solution contained the nanoparticles now coated by oleic acid and soluble in the organic solvent, while the yellow residual polyol remained at the bottom of the becker (**figure 2.9b**) (the yellow color is an effect of DEG

thermal degradation after synthesis). The dark solution with NPs was separated, washed with acetone and ethanol and centrifuged to collect NPs, which were finally dried overnight in oven at 60°C. These particles were labelled as CFO-OA.

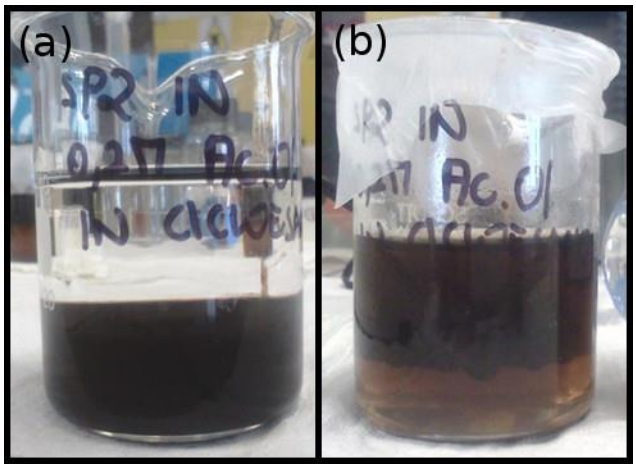

Figure 2.9: The pictures describes the the solution before (a) and after (b) the exchange ligand process.

The polyol is linked to the metal cations at NPs surface trough electrostatic interactions of the oxygen [106,107], on the other hand it is reported that oleic acid owns a stronger covalent bonding [60], this explains the preferential attachment of OA with respect DEG.

The TGA-SDTA analysis (**figure 2.10**) confirms the difference in the organic coating with a shift toward higher temperatures of the exothermic decomposition peak produced by the oleic acid compared to DEG.

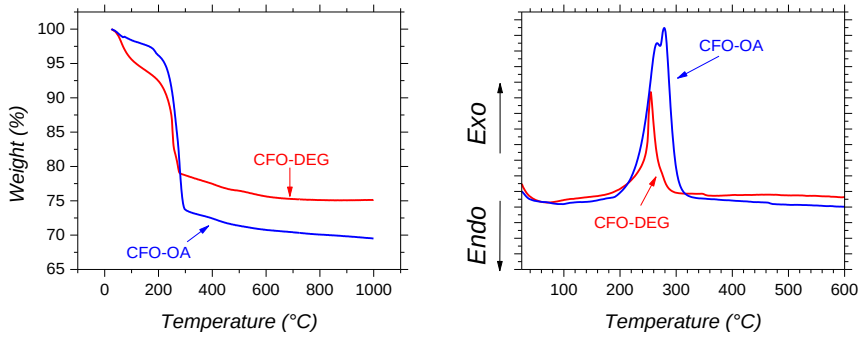

Figure 2.10: TGA (a) and simultaneous DTA (b) curves of CFO-DEG and CFO-OA samples.

FT-IR analysis supports the same picture (**figure 2.11**). The presence of spinel ferrite structure is confirmed by the signals around 590 cm^{-1}, referred to the stretching vibration of the metal in tetrahedral site and the oxygen, while the signal around 400 cm^{-1} is the analogous for the octahedral site [56,108]. The symmetrical and asymmetrical stretching of C-H (signals between 2922 and 2850 cm^{-1}) are typical of both surfactants but their intensity increase with the longer chain of OA. The C-O stretching (around 1100 cm^{-1}) confirms the polyol presence [63]. In particular, the interaction between polyol oxygen and metal cations at particles surface finds evidence both in the small shift to lower frequencies of the C-O signals with respect to the pure polyol [107], and in their different intensity profile [106,109], with two signals in place of the small three of the pure DEG. The signals around 3377 and at 1616 cm^{1} are referred to the stretching and bending modes of O-H of polyol and adsorbed water [63]. Finally, the complex profile between 1500 and 1400 cm^{-1}, shows the emerging of COO^- stretching signals after the substitution with OA.

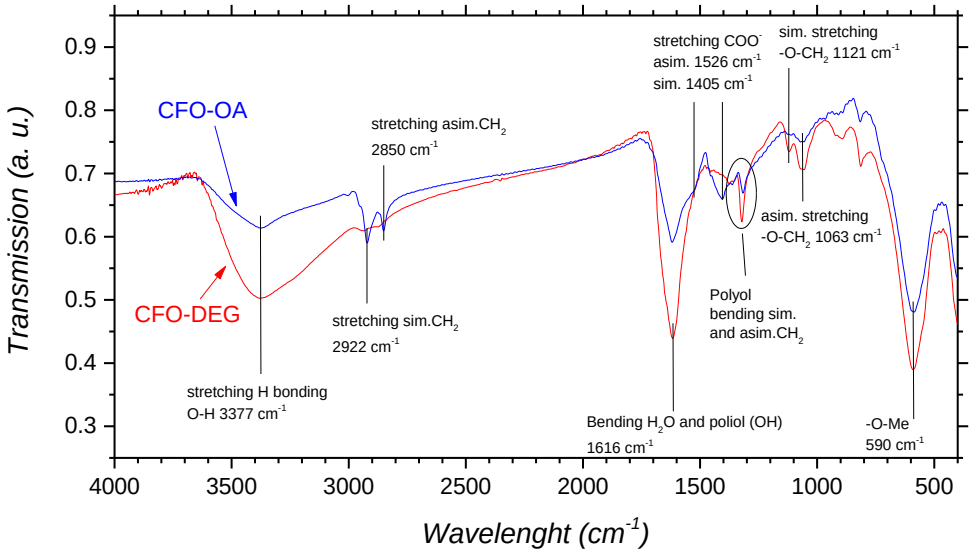

Figure 2.11: FT-IR spectra of CFO-DEG and CFO-OA.

2.2.2 Influence of molecular coating on magnetic properties

The M Vs H curves of both samples are compared in **figure 2.12**. The curves, measured at 5 K, show a hysteretic behavior, but with a strongly higher saturation magnetization for CFO-DEG. This suggests that the DEG coating owns a better effect in reordering magnetic spins at particle surface with respect oleic acid.

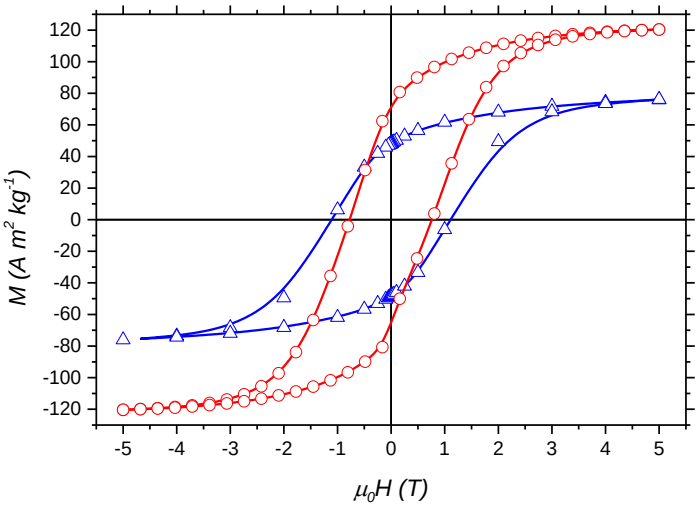

Figure 2.12: M Vs H curves measured at 5 K for CFO-DEG (circles) and CFO-OA (triangles).

This is confirmed by the lower coercive field, and in the even more pronounced reduction of saturation field of CFO-DEG (**table 2.3**).

Sample	***M_S***	***$\mu_0 H_C$ (T)***	***$\mu_0 H_{SAT}$ (T)***	***$dM/d\mu_0 H$ ($A\ m^2\ kg^{-1}\ T^{-1}$)***
CFO-DEG	120(10)	0.77(1)	3.44(2)	1.3(1)
CFO-OA	84(5)	1.11(1)	3.93(2)	1.9(1)

Table 2.3: The saturation magnetization M_S, the coercive field ($\mu_0 H_C$), the saturation field ($\mu_0 H_{SAT}$) and the susceptibility at 5 T ($dM/d\mu_0 H$) for the two samples are compared.

Such reduction of the high anisotropy component can be related to particles surface, considering that is coupled with a corresponding lower value of susceptibility at high field.

The differentiated remanence curve of M_{DCD} (see **appendix 8.2.3**) with respect to $\mu_0 H_{reverse}$ ($\chi_{irr} = dM_{DCD}/d\mu_0 H$), represents the irreversible component of the susceptibility. This quantity can be considered as a measure of the energy barrier distribution which, in a nanoparticles system, is associated with a distribution of particles coercivities and it is generally called the switching field distribution (SFD) [11,70,110]. It is worth to mention that the SFD (**figure 2.13**) evaluated for both samples, are perfectly comparable once normalized for the saturation magnetization.

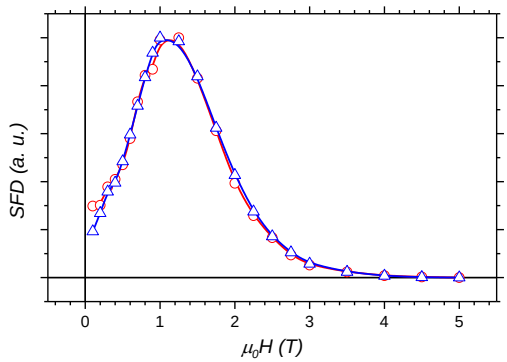

Figure 2.13: The switching field distributions of CFO-DEG (circles) and CFO-OA (triangles).

This evidences that the difference produced by the exchanged ligand is only related to an irreversible part of the magnetization, such type of contribution that is usually related to surface spins.

The effect of the surfactant is usually explained in terms of restoring the coordination at particles surface. The crystal field splitting energy (CFSE) is enlarged by the metal-surfactant bond, thus reducing the spin-orbit coupling, responsible of single ion anisotropy [95] (**figure 2.14**). As results, increasing the CFSE, the surface anisotropy is reduced explaining the reduced coercive field measured for coated Vs bare particles [70]. This restored coordination has been analyzed with density functional calculations, evidencing as the oleic acid coated particles exhibits a condition closer to the bulk with

respect bare particles, since the coating reproduces in part the bulk crystalline coordination. This induces similar electronic bands occupation, which translates in a magnetization closer to the bulk value [72]. The donor/acceptor nature of the surfactant is linked to the effect on the CFSE. The π-acceptor behavior has a stronger splitting effect, thus it reduces the anisotropy energy, leading to a lower coercive field with comparison to π-donor coated particles. Furthermore, for a given head-group, increasing the length of the surfactant chain induces higher surface anisotropy [71].

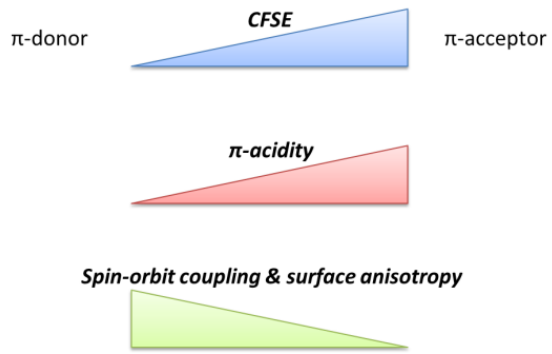

Figure 2.14: Graphical sketch of the correlation between the crystal field splitting energy and the donor-acceptor nature of surfactants, and how it reflects on spin-orbit coupling and magnetic anisotropy.

Thanks to the exchange ligand process, it is possible to modulate the interparticles distance selecting surfactants according to their chain length. Relation (1.12) roughly describes the influence of particles distance on the dipolar interactions energy:

$$E_{dip} \approx \frac{\mu_0}{4\pi}\frac{\mu^2}{d^3} \qquad (1.12)$$

According to that, a clear difference is expected between samples. Indeed, the oleic acid owns a chain length of ≈ 2 nm [70] and attaches perpendicular to particles surface. On the other hand, DEG attaches parallel to particles surface [107], producing a coating estimated in ≈ 0.5 nm. The analysis of ΔM-plot (**figure 2.15**) provides useful information

on the interacting regime among particles (see **appendix 8.2.3** for further details on such protocol). It evidences negative deviation in the curve of both samples, sign of the prevalence of dipolar interactions. The reversal field for both samples is similar (around ≈ 0.85 T), confirming the result of the SFD, but the intensity of the deviation, proportional to the intensity of interparticles interaction energy, is more than two times larger for CFO-DEG.

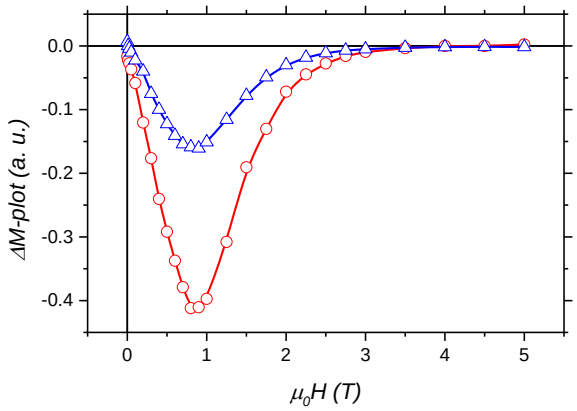

Figure 2.15: ΔM-plot of CFO-DEG (circles) and CFO-OA (triangles) samples.

As expected, the larger interparticle distance produced by the oleic acid coating, translates in less intense interparticle interactions. The intensity of the negative deviation for CFO-DEG is ≈ 2.5 times that of CFO-OA, almost the same ratio obtained between the two estimated dipolar energy (≈ 37 K Vs 14 K).

The interparticle interactions are responsible of influencing the blocking temperature of SPM nanoparticles. Analyzing the ZFC-FC and TRM curves, and the blocking temperature distribution extracted by the TRM derivative (**figure 2.16**, see **appendix 8.2.1** for the detailed procedure to evaluate it), a higher anisotropy energy is shown by CFO-DEG, where the interparticle interactions exhibits stronger intensity. This increment in the anisotropy energy is small and disappears with the application of field larger than that (2.5 mT) used for measure such curves. This explains why this effect is no more visible in M Vs H and SFD distributions.

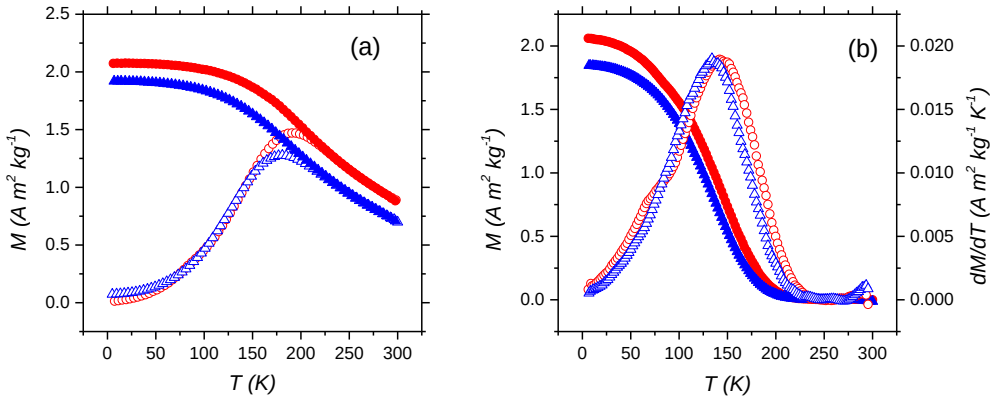

Figure 2.16: The ZFC (empty symbols) and FC (full symbols) for sample CFO-DEG (circles) and CFO-OA (triangles) are showed in panel (a). Panel (b) reports the TRM (full symbols) and the corresponding derivative curves (empty symbols) for sample CFO-DEG (circles) and CFO-OA (triangles), respectively.

The exchange ligand process was employed to study the effect of diethylene glycol and oleic acid on the same batch of 5 nm cobalt ferrite particles. A detailed magnetic investigation has shown that a strong modification can be produced by this approach, controlling the magnetic behavior of surface component of each nanoparticle. Furthermore, each surfactant produces a specific distance among particles, which translates in different interparticle interactions, influencing the effective anisotropy energy. This study can be considered as a first step in the analysis of the role of the organic coating, indeed the same approach can be expanded to other surfactants and materials in order to develop new device at nanoscale.

2.3 Notes: Average canting angle evaluated from Mössbauer spectroscopy in high field

^{57}Fe Mössbauer spectra have been recorded at 10 K under a magnetic field of 8 T (B_{ext}) applied parallel to the γ–beam. For such setup, when the second and fifth lines have a non-zero intensity, they evidence a canted structure for iron magnetic moments with respect to the applied field (non-collinear magnetic structure) [100,101]. In case of a non-collinear spin structure, the measured effective nucleus field (B_{eff}) forms the angle θ with the external field (B_{ext}) as graphically illustrated in **figure 2.17**.

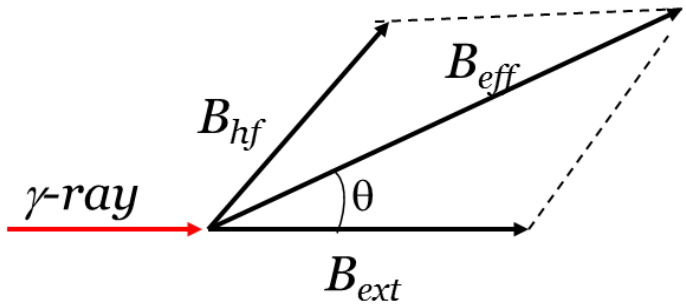

Figure 2.17: The setup for ^{57}Fe Mössbauer spectroscopy and the relation between the hyperfine field (B_{hf}) the measured effective nucleus field (B_{eff}) and the external field (B_{ext}), with evidenced the average canting angle θ.

For a thin sample, where thickness effects are negligible and where the direction of the hyperfine field is random with respect to the gamma ray direction, the relative area of the Zeeman sextet are in the ratio:

$$3: 2p: 1: 1: 2p: 3 \qquad (2.2)$$

where p is dependend on the eventual canting angle angle θ:

$$p = \frac{2\sin^2\theta}{1+\cos^2\theta} \qquad (2.3)$$

By normalizing the total area to 1, the area of lines 2-5 ($A_{2,5}$) is equal to:

$$A_{2,5} = \frac{1}{2}\sin^2\theta \qquad (2.4)$$

From such value, the average canting angle ϑ is determined [100]:

$$\theta = arcsin\sqrt{2A_{2,5}} \qquad (2.5)$$

Chapter 3
Advanced analysis of nanoparticles morphology from TEM images

Particle it morphology (i.e., size and shape) owns a key role in tuning MAE; it appears equally important to control the distribution of morphology in an ensemble of NPs, in order to minimize the different magnetic anisotropy among particles obtaining a more homogeneous response of the whole system. In this framework, it emerges the need of a precise statistical analysis of the size and shape distributions in order to understand and tune the MAE [65,111,112].

Here, a complete approach to study nanoparticles morphology by TEM analysis is proposed introducing the concept of *aspect map* (AM) [113]. It correlates size and shape, providing a comprehensive overview of an ensemble of nanoparticles and allowing to extract additional and relevant information from TEM images. In order to demonstrate the rigorous approach used to obtain our results, all the steps necessary to get aspect maps will be discussed in detail. Finally, the potentiality of the AMs in describing the morphological features of a sample will be shown trough a case study; aspect map will be employed in the analysis of high temperature thermal decomposition synthesis, allowing tuning a pre-synthesis vacuum step to increase particles size and improve size distribution.

3.1 Software and methods

The software nowadays available for digital images analysis introduce new perspectives in nanoparticles size and morphology investigation. The first aim of the digital elaboration here described is to obtain black and white (B&W) binary images, which would preserve the original shape and size for each particle. The great advantage of using this approach is the possibility to use semiautomatic tools managing thousands of particles and collecting more detailed information. It allows conducting a morphological analysis, minimizing the effects of subjective choice of the operator in the measurements process. Of course several, important shrewdness have to be taken in order to avoid artifacts and wrong information.

For each image a multistep analysis routine is usually employed [114,115]. The first step involves the enhancement of the image contrast to evaluate the right particles perimeter, which needs to have particles with a surface as smooth as possible. To remove artifacts and reduce noise, it is possible to employ some filters, without altering the original information and the real shape of the particles. Finally, a segmentation process produces the final B&W binary image ready to be studied by a digital analysis software. Nowadays a wide range of commercial and free software are available; for our purpose we have performed the analysis using the free image processing suite "Fiji"[116].

3.1.1 **Size evaluation**

The use of software like Fiji allows collecting a lot of information about individual particle such as the minimum and maximum length and width, as well as the area and perimeter of the projected image. For spherical-like particles, one way to evaluate the average diameter is to calculate the mean value between the maximum width and length of the particle. This allows a good estimation of the diameter, regardless the particle shape. Finally, the frequency counts of particles size are fitted with a lognormal function [117]:

$$\mathrm{P} = \frac{100}{\mathrm{D\ w}\sqrt{2\pi}} \exp - \left[\frac{\ln^2\left(\mathrm{D}/\langle \mathrm{D_{TEM}} \rangle\right)}{2\mathrm{w}^2}\right] \qquad (3.1)$$

where $\langle D_{TEM} \rangle$ is the median of the variable "diameter", often used to estimate the average diameter of nanoparticles [118–120] and w is the standard deviation of the natural logarithm of the variable D. To estimate the polydispersity of the sample with respect to the average particle size, the empirical parameter PD [nm^{-1}] has been defined:

$$PD = 100 * \frac{w}{\langle D_{TEM} \rangle} \qquad (3.2)$$

3.1.2 **Shape evaluation**

To analyze the particle morphology, the shape descriptor termed as “circularity” (C) has been used:

$$C = 4\pi \frac{A}{P^2} \qquad (3.3)$$

where *A* and *P* are particle’s area and perimeter. This parameter is widely used to define the deviation from a perfect spherical shape [121,122], that is represented by a value of 1, while lower values describe square, triangular or more complex shapes.

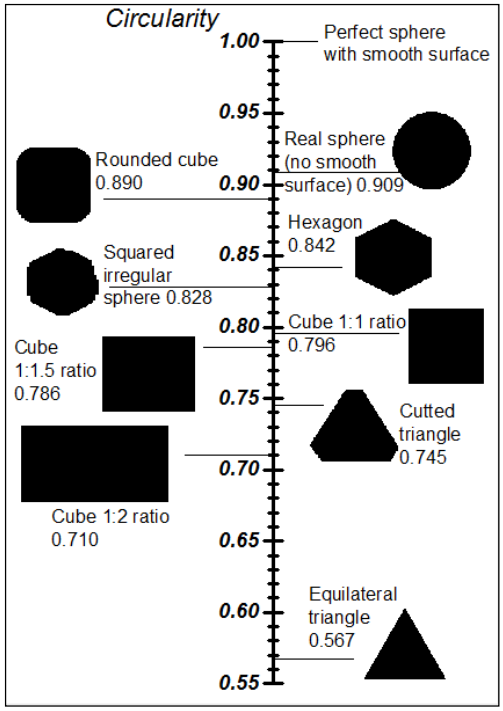

Figure 3.1: Circularity values for typical particles and ideal geometrical shape. The reported values have been evaluated by Fiji software.

Figure 3.1 shows some examples of shapes and the effective results obtained through “Fiji” analysis of the circularity. It is worth mentioning that due to the digital nature of images, particles perimeters do not describe a perfectly smooth curve but present a somehow rough appearance that results in lower circularity values, in particular for smaller particles. As example, the sphere reported in **figure 3.1** shows a circularity of 0.909, though it owns the aspect ratio of a perfect sphere.

3.1.3 **Detailed morphological analysis of nanoparticles**

Figure 3.2a presents an example of a high contrast TEM image used for a detailed digital analysis. **Figure 3.2b** shows the same image after an editing process that has removed the background noise by accurately tuning the curves, and has increased the contrast. Such edited image can be converted into a B&W binary version (**figure 3.2c**).

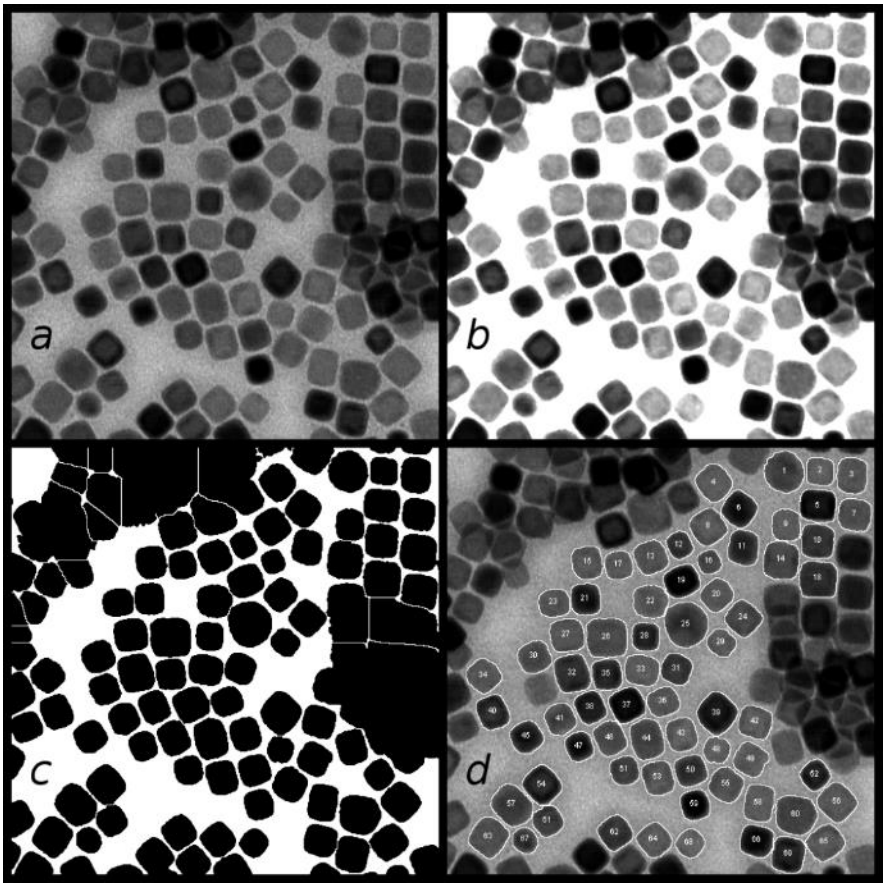

Figure 3.2: (a) original TEM image. (b) Adjusting levels and curves, the background noise was removed, and particles were isolated using "despeckle" and "remove outlines" filters. (c) Using the proper threshold and the "watershed" filter, the image was transformed in a binary version with clearly separated particles. (d) The final particles (with white borders and numbers) are superposed to the original image to confirm their correct identification, proving the accuracy of sampling and analysis.

Often some regions of the initial image are useless for the analysis and/or they present particles superimposed to each other which can create artifacts in the segmentation

process [123]. For this reason, such regions must be excluded from the process, carefully setting specific criteria, i.e., a range of area and/or circularity. If only square and spherical particles are present, a lower threshold of 0.6 can be imposed for circularity, knowing that under this value we are considering only elongated or triangular shapes, those are absent in the real image. **Figure 3.2d** presents a final example of a good elaboration and the particles effectively measured. The numerical data evaluated from this image are now ready for a statistical analysis.

3.2 Aspect map: practical example

As model system for morphology analysis, cubic and spherical particles of $CoFe_2O_4$ have been synthetized by high temperature decomposition of metalorganic precursors. Two sets of TEM images by two different ensemble have been considered; the first one with almost spherical shape nanoparticles (**figure 3.3a**) and the second one with cubic shape with rounded edges (**figure 3.3b**). Spherical particles of the first sample present a rough surface resulting in a mode value for circularity of 0.93(1) (**figure 3.3d)**. The cubic particles instead have rounded edges, which increase the circularity from the ideal 0.785 to 0.89(1), towards that of a more spherical shape **(figure 3.3d)**. Individual size distributions are centered on 12.7(1) and 15.7(1) nm for spherical and cubic particles, respectively (**figure 3.3c**).

We have created a single image from a set with different magnification, scaling all of them to the same size. This was done to simulate a single sample that contains two well-known size and shape distributions. The results of the analysis are shown in **figure 3.4**. More than 4700 particles were collected allowing to use a binary step of 0.5 nm, which is very small and allows an higher resolution with respect the typical particles size analysis proposed in literature. Nevertheless, there is not a clear signature of the two particles size distributions, since a unique lognormal curve fits the distribution with a good accuracy (**figure 3.4a**). The circularity distribution presents a clear peak around 0.93 (**figure 3.4b**), and a small shoulder around 0.89, as the original individual samples. Trying to analyze the particles size distribution with two log normal curves (**figure 3.4c**), the goodness of the fit evaluated by both the adjusted R^2 and the reduced χ^2 parameters improves, but the results of the single fit components do not well represent the expected ratio (≈ 2:1) between the two original shapes (3000 spheres Vs 1757 cubes).

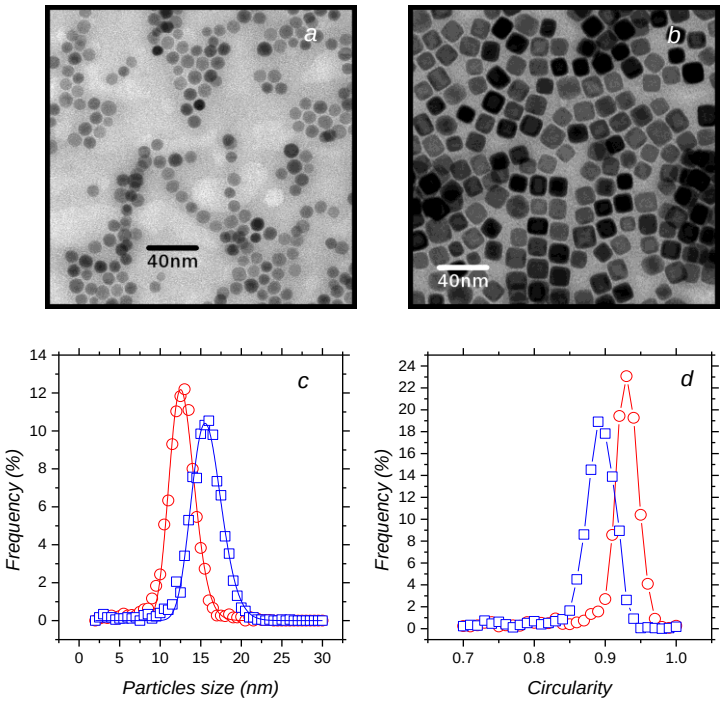

Figure 3.3: TEM images of ensembles of spherical (a) and cubic (b) nanoparticles. A comparison between particles size distributions is shown in panel (c), while circularity distributions are reported in panel (d), using circles and squares to represent data for spherical and cubic samples, respectively.

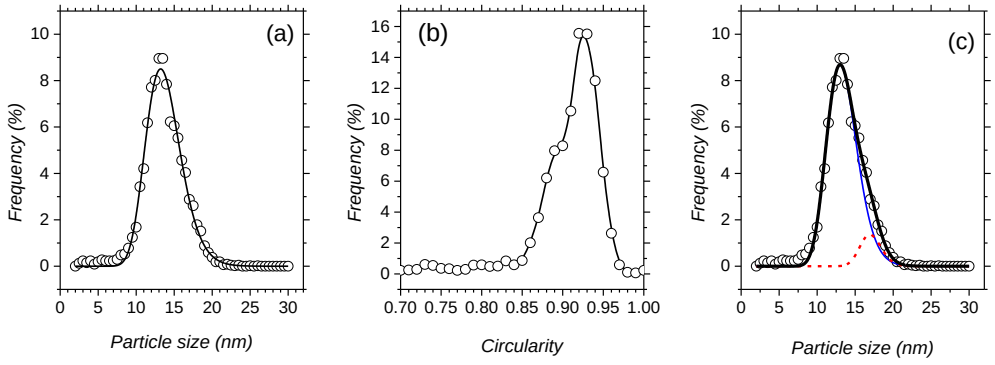

Figure 3.4 The particle size distribution of the "composite" sample is shown in panel (a) while the lognormal fit is presented as a line. Panel (b) describes the circularity distribution of the sample. A couple of lognormal curves (continuous and dashed line) are used to fit the particle size distribution in panel (c); the total resulting fit is represented as a bold line.

Moreover, the calculated mean size values are not sufficiently accurate, being 13.2(1) and 17.0(3) nm for spheres and cubes, to be compared with the real values of 12.7(1) and 15.7(1) nm of the original samples. In addition, it is worth to mention that no correlation between the average size and the corresponding particle shape is provided by this kind of analysis.

For a deeper and more accurate analysis of morphology, an aspect map was extracted (**figure 3.5**). The aspect map gives a complete description of nanoparticle, correlating for each one size and shape identifying a point on a surface, which represents the parameter called “aspect”. This allows a simpler and faster identification of each particle, distinguishing two of them not only for a difference in size, but also for a difference in shape. As in the case of a particle system, where the difference in diameter is too low to be able to clearly distinguish two groups, but the difference in volume is large enough to clarify the presence of a bimodal distribution, in the same way the “aspect” may show different groups of particles otherwise not clearly identifiable.

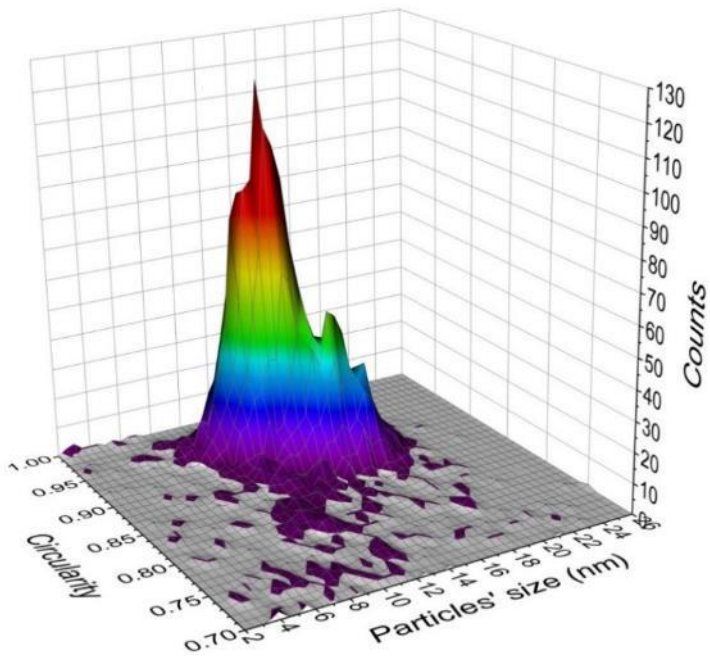

Figure 3.5: Aspect map of the “composite” sample shown as a 3D surface.

The potential of aspect maps is well demonstrated by the results in **figure 3.5**, where the presence of two peaks, centered around the corresponding values of 13.0(5) nm (diameter) and 0.93(1) (circularity), and 15.5(5) nm (diameter) and 0.89(1) (circularity), is clearly evidenced. These values match perfectly with those of the original individual samples, confirming the validity of the method to analyze particles aspect and distinguish the presence of different groups.

3.3 Case Study: Effect of the oxygen content in the reaction environment on size and shape of $CoFe_2O_4$ nanoparticles studied by aspect maps.

Advanced synthesis approaches, necessary to achieve a strict control of the structural, morphological and chemical properties of nanomaterials, are at the basis of a reproducible manipulation of their unique physical behavior. Nowadays, this is one of the most difficult problems faced by nanotechnology. In fact, any advanced application that takes advantage of nanoparticle systems will also rely on the achievement of such control. This is true in particular for magnetic nanoparticles that are unique and complex physical objects whose properties can greatly differ from their parent massive materials [10,124].

Within this context, the synthesis of spinel ferrite nanoparticles ($MeFe_2O_4$, Me = Fe^{2+}, Co^{2+}, Ni^{2+}, Zn^{2+}, …) with controlled morpho-structural features represents an important subject due to the strong interest in these materials from both a fundamental [95,125–127] and a technological point of view (e.g., MRI [16], hyperthermia [20], drug delivery [16,17], catalysis [128], microwaves applications [129]). In the last 20 years, different approaches have been developed to obtain spinel ferrite NPs with a specific size and composition, for example sol–gel [54,130,131], micellar methods [56,57], hydrothermal processing [58], surfactant-assisted high-temperature decomposition techniques [59,61,132] and polyol process [62,63]. Among them, the high-temperature thermal decomposition (HTD) of metal-organic precursors (acetylacetonates, acetates) has a number of advantages; for example, it allows obtaining highly crystalline products with narrow size distribution [87–89] in a wide range of chemical compositions. Similar size distribution and crystalline degree can be also obtained by metal-oleate based synthesis [75,132], but exploiting a more complex procedure (i.e., the synthesis of the precursors in a separate step [75,132] and several days of aging of the precursor to

obtain NPs with a single ferrite phase [133]). The advantage of metal-oleate based synthesis is the possibility to produce particles size above 12 nm [92,134], which is the size limit of the HTD synthesis based on acetylacetonate or acetates precursors [76,135,136]. In this case, a size increment is obtained by a seed mediated growth approach, which, however, employs more steps and induces a broadening in size distribution, and strain and defects in the crystalline structure [137].

The HTD synthesis process is usually described by the LaMer model [138,139] (**notes 3.3.4** at the end of this chapter). The solution is initially heated slightly above the decomposition temperature of the precursors (e.g., metal acetylacetonates [136]) to produce a high concentration of the "monomers", above their supersaturation limit, initiating the nucleation process. Ideally, this should be very quick, bringing the concentration below the supersaturation threshold, thus avoiding further nucleation. Then, the growth proceeds with monomers addition and the solution temperature is increased to raise the supersaturation limit in order to reduce the formation of new nuclei. When almost all monomers are depleted, the solubility of particles increases and Ostwald Ripening (OR) may occur [138,140,141]. In the OR process, the particles under a critical size re-dissolve, producing new monomers that can feed the growth of the biggest particles, thus broadening the size distribution (i.e., defocusing). For surfactant coated NPs, this is usually quite a slow process that produces visible effects on size distribution only while retaining the solution under reflux for several hours. Indeed, due to the organic coating acting as a protective layer, the coalescence of primary particles can be considered negligible. The nucleation step in HTD synthesis involves almost all the precursors, leaving a relatively small amount available for the particle growth. This is a critical step for controlling the size of the nanoparticles.

In most cases, HTD synthesis protocol makes use of a nitrogen flow [92,136,142] to reduce the oxygen content, creating a more homogenous environment and consequently leading to narrower size distributions. For the same reason, initially, the solution is often kept slightly above 100 °C to degas the system [74,143,144]. Despite the wide spread use of HTD approach, a systematic investigation on the influence of residual oxygen (RO) dissolved in the reaction solution has not been previously reported. In addition, a mechanistic approach to control the nanoparticle size beyond varying temperature and surfactants has never been attempted. Furthermore, as previously discussed, another key challenge of HTD is to obtain particles larger than 12

nm in a single step, while preserving both the crystalline phase and the chemical composition.

The present study investigates the effect of residual oxygen dissolved in the reaction environment on the reaction kinetics and the morphological properties of $CoFe_2O_4$ nanoparticles. The amount of RO was controlled by degassing the reaction environment at a different extent and monitoring the values of total residual pressure. It will be demonstrated how the control of RO is a powerful tool to tune the size of nanoparticles up to ≈ 19 nm, while retaining a narrow size distribution. Cobalt ferrite particles represent a model system for this study; furthermore, they are of interest in several fields, e.g., $CoFe_2O_4$ NPs in the 19-25 nm size have attracted attention for the design of new exchange coupled nanocomposites for applications as permanent magnets [145,146]. Moreover, the specific attention on obtaining a narrow size distribution emerges from applications that demand the switching of the magnetization in a very small range of magnetic applied field (e.g., magnetic hyperthermia [65]), which can be obtained with a sharp size distribution. The evolution of particles morphology was described by an analysis of S(T)EM images, correlating size and shape using aspect maps (AMs). Highlighting the various steps of growth with respect the RO amount, the formation mechanism of NPs was analyzed.

3.3.1 **Results**

All syntheses were carried out using a standard Schlenk line setup. For the synthesis of $CoFe_2O_4$ (CF) nanoparticles, 0.67 mmol of iron (III) acetylacetonate (97%, Sigma-Aldrich), 0.33 mmol of cobalt(II) acetylacetonate (97%, Sigma-Aldrich) and 8 mmol of 1,2-hexadecanediol (90%,Sigma-Aldrich) were mixed with 16 mmol of oleic acid (90%, Alfa Aesar), 4 mmol of oleylamine (70%, Sigma-Aldrich) and 20 ml of benzyl ether (98%, Sigma-Aldrich) in a two neck flask connected to a condenser and equipped with a thermocouple connected to a temperature controller. A vacuum pump with digital controller was used to degas the solution for 60 min at a temperature of ≈ 110 °C at a fixed pressure. Later, the vacuum was turned off, and the solution temperature was raised and kept at 200 °C for 30 min under argon atmosphere. Finally, the solution was kept under reflux at 290 °C for 60 min. After cooling the solution to room temperature, the nanoparticles were precipitated by adding hexane and excess of isopropanol and collected by magnetic separation. The nanoparticles were washed two times with hexane and acetone to remove the excess amount of surfactant. The final product was dried under ambient atmosphere. A similar protocol was used to prepare 5 samples

while degassing the solution at ≈ 110 °C at different pressure, that is at ≈ 1000, 40, 0.8, 0.3, and 0.17 mbar for samples CF1, CF2, CF3, CF4, and CF5, respectively (**table 3.1**).

All the samples showed x-ray diffraction (XRD) patterns with typical reflections of a cubic spinel structure, in agreement with the presence of the $CoFe_2O_4$ phase (PDF Card 22−1086). No peaks of other phase were detected; as an example, the XRD pattern of sample CF4 is presented in **figure 3.6**.

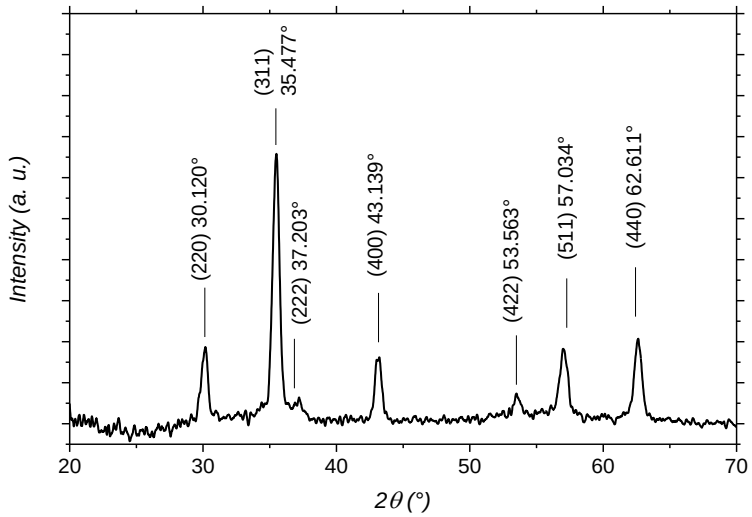

Figure 3.6: XRD pattern of sample CF4, synthesized with a residual pressure setting of ≈ 0.30 mbar.

An accurate description of particles morphology was derived from a statistical analysis of more than 2000 particles for each sample, as observed in S(T)EM images (**figure 3.7**). In order to evaluate the particle shape, an analysis of circularity distribution was carried out (**table 3.1).** In real particle systems, the spherical shape is associated with values of circularity *C* between 0.9 and 1, while the cubic one has *C* around 0.8 (**figure 3.1**). As shown in **figure 3.7i-l**, the observed circularities were in the range 0.88 and 0.92, which are in good agreement with a spherical-like shape.

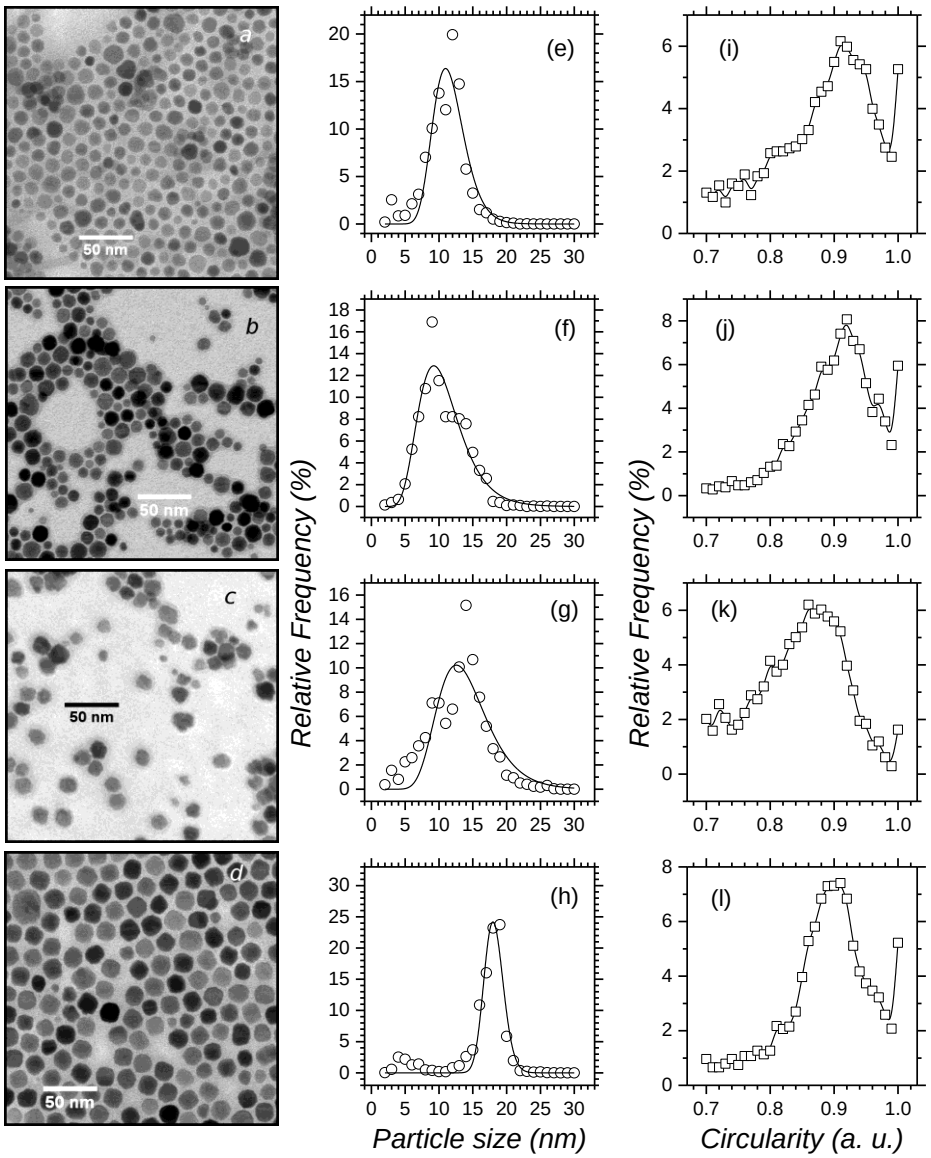

Figure 3.7: TEM images of sample CF1 (a), CF2 (b), CF3 (c), and CF4 (d). For each samples, the particles size distribution (empty circles) and the result of a lognormal fit (black line) are presented in (e), (f), (g), and (h), respectively. The circularity distributions (empty squares) are reported in panels (i), (j), (k), and (l), with the black line being a guide to the eyes.

For a deeper and more accurate analysis, aspect maps are calculated. **Figure 3.8** reports the 2D and 3D aspect maps of samples CF1, CF2, CF3, and CF4, with numerical data summarized in **table 3.1**.

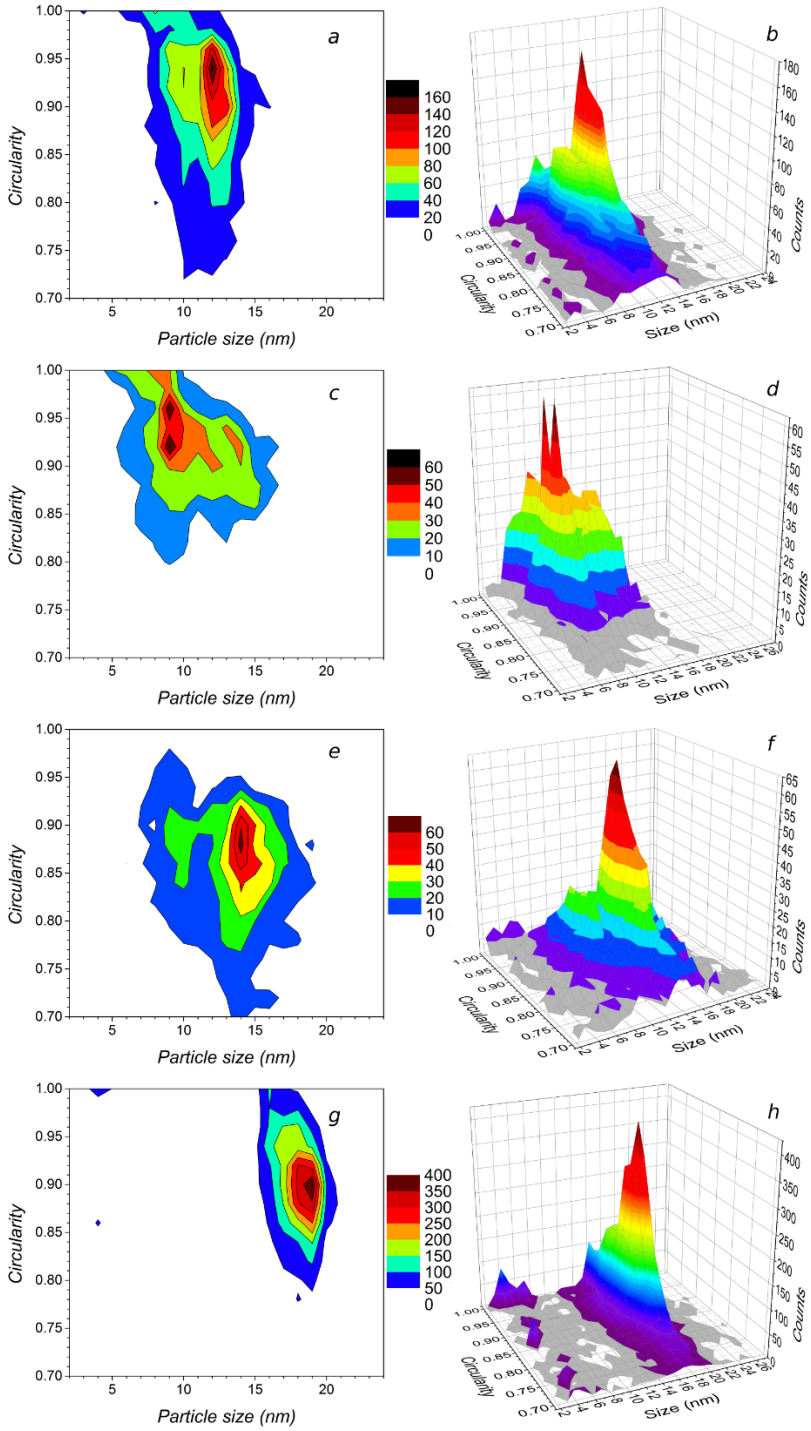

Figure 3.8: 2D and 3D aspect map for sample CF1 (panel a and b, respectively), CF2 (c and d), CF3 (e and f), and CF4 (g and h).

RP (mbar)	*Sample*	*$\langle D \rangle_{TEM}$ (nm)*	*C*	*PD (nm^{-1})*	*D_{map}^1 (nm)*	*C_{map}^1*	*D_{map}^2 (nm)*	*C_{map}^2*
R. A.	CF1	11.4(2)	0.91(1)	1.8(1)	10.0(5)	0.94(1)	12.0(5)	0.94(1)
4.0(1)	CF2	10.2(2)	0.92(1)	3.1(1)	9.0(5)	0.94(1)	14.0(5)	0.92(1)
0.8(1)	CF3	13.6(4)	0.88(1)	2.1(1)	9.0(5)	0.90(1)	14.0(5)	0.88(1)
0.3(1)	CF4	18.1(1)	0.90(1)	0.4(1)	-	-	19.0(5)	0.90(1)

Table 3.1: For each sample the residual pressure (RP) during the synthesis step at 110 °C, the average size evaluated by a lognormal distribution ($\langle D \rangle_{S(T)EM}$), the mode value of circularity (C), and the polydispersity (PD) are reported. From data extracted by aspect maps (figure 3.8), the mode values for size (D_{map}^1 and D_{map}^2) and for circularity (C_{map}^1 and C_{map}^2) are reported, distinguishing the subgroups with different apex. Uncertainties on the last digit are indicated in brackets.

The sample degassed at ≈ 1000 mbar (CF1) showed a lognormal size distribution with an average particles' diameter of 11.4(2) nm, agreeing closely with the reported size limit of 12 nm in acetylacetonates-based HTD method. Aspect maps provided a more detailed description, showing two peaks with the most intense one centered at a diameter D_{map}^2 = 12.0(5) nm, and the second one at D_{map}^1 = 10.0(5) nm. The average value of circularities (C_{map}^1 and C_{map}^2) was equal to 0.94(1) for both peaks. The effect of degassing in sample CF2 (residual pressure of ≈ 4 mbar) seems to lead to a reduction of particles size (lognormal fit average value of 10.2(2) nm), but aspect maps evidenced a more complex behavior. The main mode values D_{map}^1 = 9.0(5) nm and C_{map}^1 = 0.94(1) were identified, with an additional intense tail centered at D_{map}^2 = 14.0(5) nm and C_{map}^2 = 0.92(1). The lognormal fit of sample CF3 size distribution (residual pressure of ≈ 0.8 mbar) was centered at a higher value (13.6(4) nm). The sample showed an aspect map with two modes, D_{map}^1 = 9.0(5) nm (C_{map}^1 = 0.90(1)) and D_{map}^2 = 14.0(5) nm (C_{map}^2 = 0.88(1)), with the second one presenting a much higher frequency count value, leading to a larger average size with respect CF2 and a C value still compatible with a spherical shape. Finally, the sample CF4 (residual pressure of ≈ 0.3 mbar) presented an average size of 18.1(1) nm (C = 0.90(1)). Moreover, a careful analysis showed that experimental data are left-skewed and are not perfectly reproduced by the lognormal curve. From the AMs a value of D_{map}^1 = 19.0(5) nm (C_{map}^1 = 0.90(1)), which is more representative of the measured size distribution, was deduced. Furthermore, it is worth to underline that

the sharp size distribution of this sample is associated with a polydispersity (PD) of 0.4 nm^{-1}, which is lower than the value observed in CF1 (1.8 nm^{-1}).

Preliminary investigation of the magnetic properties of CF1 and CF4 was performed in order to highlight the differences between the sample prepared by classical HTD procedure (CF1) and the one prepared with a highly reduced residual oxygen content in the synthesis environment (CF4). In both samples, the temperature dependence of magnetization recorded by zero-field cooled and field cooled protocols (not reported here) showed irreversibility in the temperature range 5-300 K. This indicates that the superparamagnetic blocking temperatures are higher than 300 K, as expected for $CoFe_2O_4$ NPs in the size range 12-18 nm [76,147]. The field dependence of magnetization was recorded at 5 K (**figures 3.9a, b**), and the saturation magnetization (M_S), the reduced remanent magnetization (M_R/M_S), the coercive field ($\mu_0 H_C$) and the saturation field $\mu_0 H_{SAT}$ [93] extracted from hysteresis loops are reported in **table 3.2**.

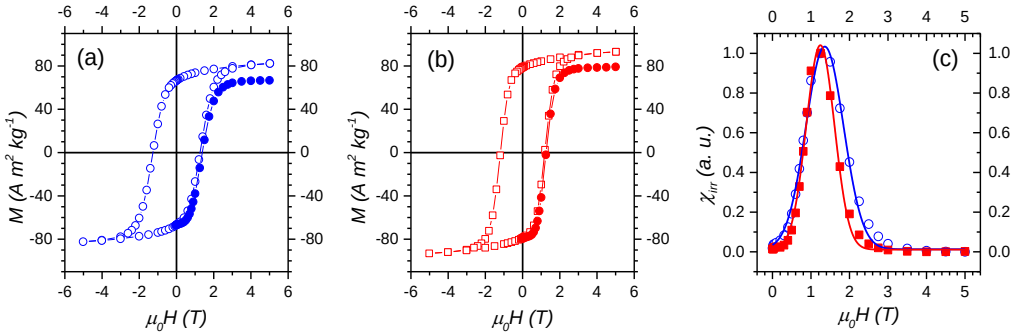

Figure 3.9: M Vs H (empty symbols) and M_{DCD} (full symbols) curves for sample CF1 (a), and CF4 (b). The switching field distributions obtained by M_{DCD} of CF1 and CF4 are reported in panel (c), as empty circles and full squares respectively, with the respective normal fit represented as a line.

Both samples showed M_S values quite close to bulk values (83 - 90 A m^2 Kg^{-1})[148], as also reported for highly crystalline cobalt ferrite nanoparticles [111]. In addition, they exhibited similar values of reduced remanent magnetization (M_R/M_S), indicating a tendency towards a magnetic anisotropy with cubic symmetry [70]. The reversal mechanism of the magnetization was further investigated studying the field dependence of remanent magnetization using the DCD protocol [149] (full symbols in **figures 3.9a** and **b**).

Sample	$\langle D \rangle_{TEM}$ (nm)	S/V (m^{-1})	$\mu_0 H_C$ (T)	M_S ($A\ m^2\ kg^{-1}$)	M_R/M_S	$\mu_0 H_{SAT}$ (T)	$\mu_0 H_C^{SFD}$ (T)	σ^{SFD} (T)
CF1	11.4(2)	0.53(1)	1.26(1)	87(9)	0.76(2)	3.4(5)	1.36(1)	0.49(1)
CF4	18.0(1)	0.33(1)	1.18(1)	98(9)	0.80(2)	2.7(6)	1.24(1)	0.37(1)

Table 3.2: The average size evaluated by a lognormal distribution ($\langle D \rangle_{TEM}$), the surface to volume ratio (S/V), the coercive field ($\mu_0 H_C$), the saturation magnetization (M_S) the reduced remanent magnetization (M_R/M_S) and the saturation field ($\mu_0 H_{SAT}$) are reported for samples CF1 and CF4. In addition, from a normal fit of switching field distribution, the average coercive field ($\mu_0 H_C^{SFD}$) and the standard deviation (σ^{SFD}) of the distribution, are proposed.

3.3.2 **Discussions**

As reported in literature, the synthesis without degassing (CF1) produced a quite narrow particle size distribution with PD = 1.8(1) nm^{-1}, related to the presence of two distinct steps for nucleation and growth. The drawback of this procedure is the relatively large amount of precursor depleted during nucleation, so that only the small residual quantity can contribute to the growth of nanoparticles (**figure 3.10a and b**). This leads to the relatively low size limit of 12 nm, usually reported for $CoFe_2O_4$ NPs obtained by the acetylacetonates HTD procedure [76,135,136]. It is reported that altering the nucleation step in such a way that the number of initial nuclei does not deplete the monomers, their concentration can be maintained above the supersaturation limit, thus leaving space to further nucleation [150]. This leads to a broad size distribution with a large number of small particles which can very likely re-dissolve producing OR, and so a further broadening is induced. The broad size distributions of samples CF2 and CF3 (PD of 3.1(1) nm^{-1} and 2.1(1) nm^{-1}, respectively), suggested that a lower amount of oxygen in the reaction environment reduces the reactivity of the monomer toward nucleation, which does not occur anymore in a quick single event.

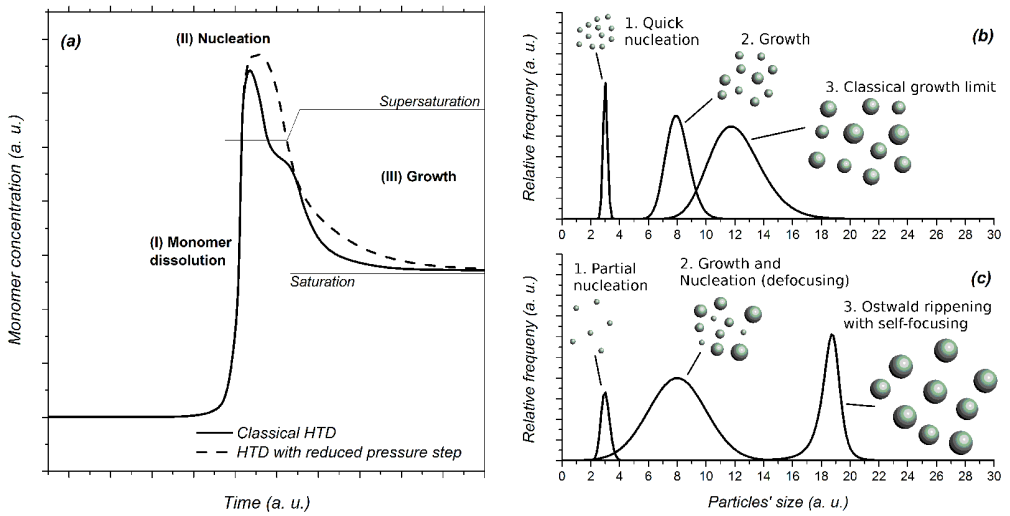

Figure 3.10: (a) The monomer concentration vs reaction time is reported to compare the HTD process at ambient and in vacuum atmosphere (continuous and dashed lines, respectively). For the classical synthesis (b), a single quick nucleation is followed by a temporally separated growth step. In the modified approach (c), a superposition between a longer nucleation step and the growth of particles can be supposed; this could be responsible of a wide defocusing, but carefully tuning the vacuum, a subsequent self-focusing effect can be induced, resulting in a mean particle size above the limit of the classical method.

As result, a double mode aspect distribution appeared in CF2 and CF3's AMs, with values centered at 9.0(5) and 14.0(5) nm, where particles growth beyond the 12 nm limit is visible. This effect is stronger in CF3, where the lower residual oxygen resulted into an increasing fraction of particles' size around 14 nm. In CF4, the double size distribution disappeared and a clear narrowing (i.e., focusing effect) of the distribution was observed.

The achievement of a narrow size distribution in the synthesis of nanoparticles, that is, the reduction of differences in size among small and big nanoparticles, depends on many factors whose rigorous control is required to obtain the so-called *size focusing* effect. Such factors are the concentration of monomers in solution, the particle solubility, which on turn depends on their size, since small particles dissolve faster than the bigger ones, and their rate of growth, which also depends on their size, since smaller particles grow faster due to their higher free energy. This last case is observed, for example, in a diffusion-limited growth [138,151]. The presence of coating on the

nanoparticles influences the growth process too, since the coating is a dynamic barrier that adsorbs and desorbs on the particles' surface, interfering with material exchange, and so it can be considered as a limiting factor for diffusion. Indeed, the growth by HTD synthesis can be considered diffusion-limited [152]. The focusing effect can also be obtained by Ostwald Ripening, exploiting the dissolution of sacrificial material (a fraction of smaller particles or a secondary crystalline phase) [153,154] that quickly dissolves producing new monomers used by the big particles to grow further [155]. In our nanoparticle system, a similar OR mechanism can be invoked to describe the particle growth. Indeed, the high concentration of NPs the solution (≈ 3 mg/ml) leads to a short interparticle distance, estimated in ≈ 45 nm under the hypothesis of <D> ≈ 12 nm $CoFe_2O_4$ particles at the beginning of the self-focusing. The smaller particles quickly dissolve and their monomers produce an interparticle-diffusion that directly feeds the growth of the neighboring bigger particles, in an accelerated ripening with self-focusing effect [152,156]. This framework describes the focusing observed in sample CF4, coherently with the analysis of aspect maps, and graphically summarized in **figure 3.10a** and **c.** The small reduction of oxygen in CF2 synthesis induces multiple nucleation events, which lead to a clear defocusing effect with respect to CF1. A further reduction of oxygen gives origin to a small focusing effect in CF3, which is completed in CF4. Only in this sample the RO pressure had the optimal value to produce the initial large defocusing, needed to produce enough sacrificial small particles to feed the ripening process, and then lead to a strong "re-focusing", completed in 60 min under reflux. To further confirm this growth mechanism, an additional sample, labeled CF5, was synthesized at a lower oxygen content (residual pressure ≈ 0.17 mbar). The sample was analyzed after 10, 30 and 60 min of reflux at the temperature of 290 °C (**Table 3.3**).

RP (mbar)	*Sample*	*$\langle D \rangle_{TEM}$ (nm)*	*PD (nm^{-1})*	*D_{map} (nm)*	*C_{map}*
	CF5 10 min	3.8(1)	6.5(1)	4.0(5)	-
0.17(1)	CF5 30 min	13.2(2)	1.8(1)	15.0(5)	0.94(1)
	CF5 60 min	18.3(3)	1.2(1)	19.0(5)	0.90(1)

Table 3.3: Sample CF5 was prepared with a residual pressure of ≈ 0.17(1) mbar, and analyzed after 10, 30 and 60 min under reflux. In table are reported the mean size ($\langle D \rangle_{TEM}$) and the polydispersity (PD), calculated from lognormal fit of particles size distribution obtained by TEM images. In addition, the mode value for size (D_{map}) and shape (C_{map}) obtained from 3D aspect map are reported. A circularity value could not be estimated after only 10 min of reflux. Uncertainties on the last digit are reported in brackets.

Aspect maps (**figure 3.11b, d** and **f**) showed a continuous increase of the average size with respect time under reflux, from 4.0(5) (10 min), to 15.0(5) (30 min) and to 19.0(5) nm (60 min). It was impossible to measure the circularity value of the sample at 10 min, but it was possible to obtain a circularity value of 0.94(1) and 0.90(1) after 30 min and 60 min of reflux, respectively. This was accompanied by a significant increase in size, a small focusing of the shape distribution and a reduction of the PD (from ≈ 1.8 to 1.2 nm^{-1}).

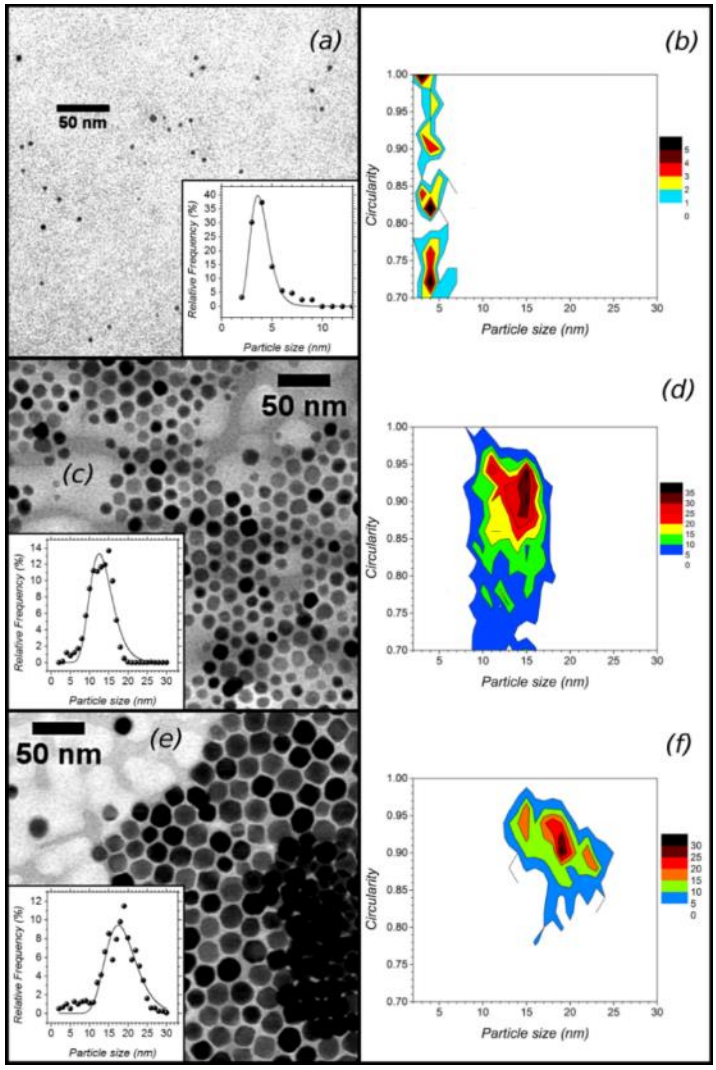

Figure 3.11: TEM images of sample CF5 after (a) 10 minutes, (c) 30 minutes and (e) 60 minutes under reflux. For each step the particles size distribution is given in the inset. Panels on the right show the corresponding aspect maps after 10 (b), 30 (d) and 60 minutes (f).

Owing to the low amount of RO in the synthesis of CF5, the reactivity was so low, and the defocusing so wide, that after 60 min the system showed the effect of a strong growth but not a clear re-focusing effect. Actually, after 60 min particles size up to 25 nm were observed, beyond the size limit of the sample CF4 where no particles larger than 21 nm were observed (**figure 3.8g**). This suggests that it is possible to complete the re-focusing, significantly increasing the average size, while keeping the sample under reflux for enough time and using a lower value of residual pressure.

The magnetic properties (e.g., magnetic anisotropy, saturation magnetization) of monodomain nanoparticles are strictly related to their size and morphology. This correlation is well described by the M Vs H curves measured at 5 K for samples CF1 and CF4 (**Figure 3.9a and b**). Both samples present quite high values of coercivity, as expected considering the high magnetocrystalline anisotropy of $CoFe_2O_4$ NPs [157–159]. The slightly higher value of $\mu_0 H_C$ observed in CF1 may be mainly ascribed to the higher surface anisotropy component due the higher surface to volume ratio of CF1 with respect to CF4 (≈ 0.53 Vs ≈ 0.33 nm^{-1}). The increase of anisotropy was even clearer observing the value of the saturation field, which is 25% higher in CF1. In addition, it should be underlined that, in order to design magnetic nanoparticles suitable for specific applications, it is essential to have very sharp distribution of size and shape. This study shows that the careful control of the RO represents an important tool in this direction, allowing obtaining particles with narrow size distribution and then a more homogeneous magnetic response of the nano-entities. This picture was well confirmed by the field dependence of remanent magnetization measured by the DCD protocol, and the related SFD, which provided additional information about the reversal process of magnetization. Fitting with a normal function the SFDs (**figure 3.9c**), the average coercive field ($\mu_0 H_C^{SFD}$) and the standard deviation (σ^{SFD}) of the distribution were estimated (**table 3.2**). The sample CF4 showed a slightly lower value of 1.24(1) Vs 1.36(1) T, in agreement with the lower $\mu_0 H_C$, but, most importantly, its SFD is clearly narrower, with a 20 %, reduction of the standard deviation, indicating that the sharper particle size distribution is associated with a sharper SFD. This represents a clear advantage, since it corresponds to a sharp reversal of the magnetization of the whole ensemble, and to a narrower distribution of SPM blocking temperatures. These magnetic features are suitable for technological applications, such as magnetic hyperthermia [65], where if the SFD is narrower it is possible to more precisely cut off the heating effect due to the SPM transition of the nanoparticles.

3.3.3 **Conclusions**

This work focused on the influence of the amount of residual oxygen content present in the reaction environment on the growth mechanism of $CoFe_2O_4$ nanoparticles prepared by thermal decomposition of acetylacetonate precursors. The study was conducted by a morphological analysis of NPs from S(T)EM images using a new statistical approach, based on the so-called aspect map that allows to better understand the NPs growth mechanism. The reduction of the oxygen content, i.e., degassing the solution at low pressure, prolongs the nucleation phase. This occurs in multiple events producing a defocusing effect and providing more precursors available for the growth phase. Due to the process conditions (i.e., high particle concentration and initial broad size distribution), an Ostwald ripening accompanied by a strong focusing effect was then favored. By tuning the oxygen content, the defocusing-refocusing process was optimized to produce average particles size of 19 nm (well beyond 12 nm which is often considered a size limit for cobalt ferrite nanoparticles obtained by acetylacetonates HTD synthesis) and very narrow size distribution (polydispersity of 0.4(1) nm^{-1}). In addition, considering the incomplete re-focusing at the lowest residual pressure employed in CF5, even after 60 min of reflux, this method seems promising for obtaining particles size up to 25 nm. It should be underlined that the study of RO is critical, due to the little differences in play; for this reason, the reproducibility of each experiment has been carefully checked.

The rigorous control of the oxygen amount in the reaction environment was effective in producing improved magnetic properties. This work demonstrates it is an optimal strategy to reduce the switching field distribution up to 20 %, leading to an optimized magnetization reversal in a narrower magnetic field range, which represents a critical issue for specific applications. Indeed, it can be used to improve the performance of magnetic materials in several applications, from magneto-recording to biomedical ones. In addition, cobalt ferrite particles in the 19-25 nm size range are of interest for the design of new exchange coupled nanocomposites for applications as permanent magnets [145,146]. Finally, the analysis by aspect maps has been shown to be very powerful providing a tool for understanding growth mechanism, being extendable to the study of many other systems.

3.3.4 **Notes: LaMer synthesis mechanism**

LaMer model [139] is usually employed to describe the formation of colloidal particles [138], e.g., for HTD method.

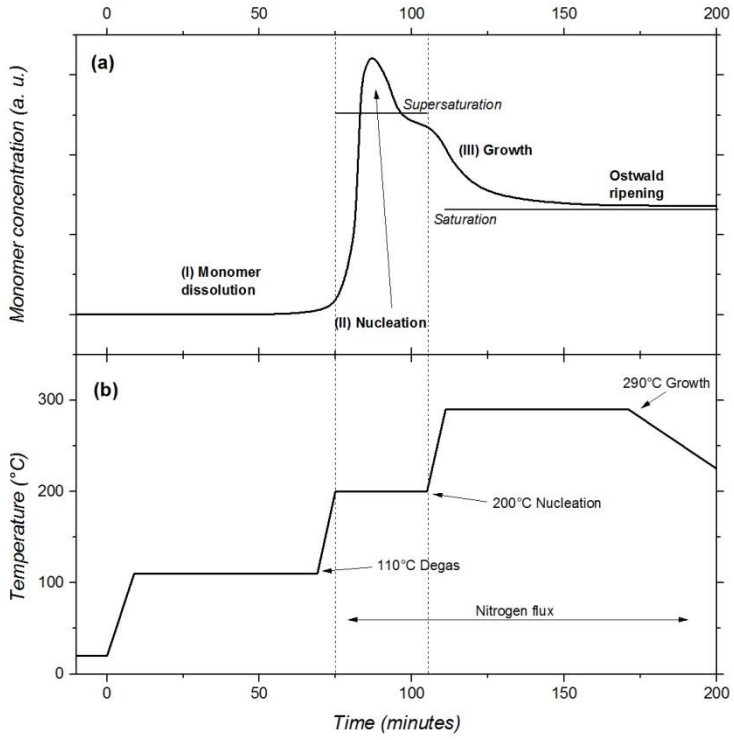

Figure 3.12: LaMer model of reaction (a), and common steps for HTD synthesis (b).

As summarized in **figure 3.12**, we can distinguish different phases:

I. The solution is heated up around 200°C, slightly above the decomposition temperature of the precursors (170-180 °C for cobalt and iron acetylacetonates). The concentration of the "monomer" (metal ions in this case) has a sharp increase.

II. When monomer concentration overcomes the limit of supersaturation, the nucleation occurs. This step should be ideally very quick, producing a few number of nuclei, and dropping immediately the concentration of the

monomer under the supersaturation limit, to avoid successive nucleations. this is possible employing high thermal decomposition of precursors (e.g., acetylacetonates) [136].

III. When the concentration of monomer is under the supersaturation, nuclei ideally grow for monomer addition. Keeping solution at higher temperature, usually around 300°C, increases supersaturation and reduces risk of further nucleations. When almost all monomer is consumed, and its concentration becomes very low, the solubility of particles increases, and Ostwald Ripening can occur [138,140,141]. In OR process, the small particles under a critical size re-dissolve, producing new monomers those feed the growth of the biggest particles, broadening the size distribution. This process further reduces the size of the smaller particles while produce an increment for the bigger ones, broadening the particle size distribution (defocusing). For surfactant coated nanoparticles, this is usually a quite slow process, which produces visible effects on size distribution only keeping the solution under reflux for several hours.

Chapter 4
Tuning the magnetic anisotropy with chemical composition

Beyond the magnetic interparticles interactions, the physics of nanoparticle assemblies is influenced by their finite-size effects and by the modification of the structural and electronic properties at their surface. Among the relevant features of the size reduction of magnetic particles, the presence of a non-collinear spin structure (spin-canting) at the particle surface deserves special attention, as it originates strong modifications in the magnetic properties. The symmetry breaking induces changes in the topology of the superficial magnetic moments and consequently in exchange integrals (through superexchange angles and/or distances between moments), thus leading to a different local surface anisotropy. Recently magnetic disorder has been found to be a key factor in order to improve the performance of nanoparticles based materials for different application, e.g., hyperthermia in cancer treatment [160].

Among nanostructured materials, magnetic ferrites nanoparticles ($Me^{II}Fe_2O_4$; Me^{II} = Fe^{2+}, Ni^{2+}, Co^{2+}, etc) with spinel structure have generated much interest, due to their high chemical and thermal stability coupled with their rich crystal chemistry that offers excellent opportunities for fine tuning the magnetic properties [7]. This makes spinel ferrites ideal systems to be studied from a fundamental point of view [95,125–127], but it also make them optimal candidates for a wide range of technological applications, from electronics [76,95] to biomedicine (e.g., MRI [16], hyperthermia [20], drug delivery [16,17]). Spinel ferrite has a face-centered cubic (fcc) structure in which the oxygen ions are cubic close-packed. The structure contains two interstitial sites, occupied by metal cations with tetrahedral (T_d), and octahedral (O_h), oxygen coordination, resulting in a different local symmetry. In general, the cationic distribution between the two sites is quantified by the inversion degree (γ), which is defined as the fraction of divalent ions in octahedral sites. Super exchange interactions between magnetic atoms located in the same kind of interstitial sites ($J_{Td\text{-}Td}$ and $J_{Oh\text{-}Oh}$) lead to two ferromagnetically ordered sub-lattices. On the other hand, the dominant antiferromagnetic interactions between magnetic ions in the T_d and O_h sites ($J_{Td\text{-}Oh}$) induce a non-compensated antiferromagnetic order between the two sub-lattices

(ferrimagnetism, FiM). A sketch of the magnetic structure in spinel ferrites is reported in **figure 4.1**. The net magnetization can be considered *a priori* proportional to the difference between the T_d and O_h sub-lattice magnetizations. Furthermore, one should also consider the magnetic anisotropy resulting from specific cationic inversion due to the single ion anisotropy of the divalent cations, which depends on interstitial site.

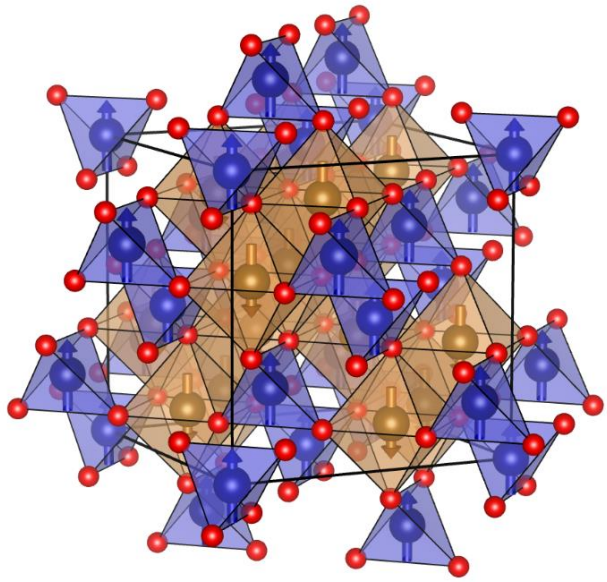

Figure 4.1: Example of spinel ferrite structure. Oxygen ions are represented as small spheres, while the big ones represent the metal cations within the tetrahedral and octahedral-coordinated polyhedra. The atomic magnetic moments are described as vectors aligned along the easy axis [110].

In most of spinel iron oxide nanoparticles (γ-Fe_2O_3, Fe_3O_4), non-linear magnetic structures are attributed to a canted superficial magnetic layer: indeed, the spin-canting originates from the competing interactions between the two sub-lattices together with the structural surface topological disorder induced by the symmetry breaking ace [101,161–163]. This feature has also been confirmed by polarized neutron scattering [164] and Mössbauer experiments [165] in cobalt and copper ferrite, respectively. Recently it has been demonstrated that an unusual correlation between cationic distribution and spin canting was established in some $CoFe_2O_4$ nanoparticles, as resulting from a disordered and non-homogeneous distribution of Fe and Co species

within the nanoparticles [6,32,96,161,166]. This picture allows concluding that the magnetic properties of ferrite nanoparticles with spinel structure are clearly influenced by the complex interplay between two inter-correlated parameters as cationic distribution and spin canting.

Thus, this work aims to the chemical control of the magnetic properties (i.e., saturation magnetization and magnetic anisotropy) of spinel oxide nanoparticles with different content of Co and Ni as divalent cations ($Co_{1-x}Ni_xFe_2O_4$, Ni = 0, 0.25, 0.50, 0.75, 1). The evolution of magnetic structure (i.e., correlation between cationic distribution and spin canting) with the chemical composition has been studied, in order to clarify the dependence of the magnetic properties from the magnetic structure itself. Some examples of similar studies have reported the influence of cobalt substitution in increasing both parameters [167–169], but considering bigger particles, and often with a large difference of mean sizes among samples. In this study, the experimental investigation will be carried out on high crystalline nanoparticles with very homogenous size (diameter: 4.5 ± 0.2 nm) allowing to focus the study on the chemical composition, beyond the effect of particles size.

4.1 Structural analysis

The X-ray diffraction (XRD) patterns (**figure 4.2**) exhibit the common reflexes of a cubic spinel structure (PDF card 22-1086) for all the samples; no other phases are detected. The size of the coherent crystalline domain (**table 4.1**), determined using the Debye-Scherrer formula, is equal for all the samples within the experimental error. The value of the lattice parameter ***a*** becomes smaller increasing the Ni amount [170], as expected due to the larger ionic radius of Co^{2+} (≈ 0.58 Å in T_d and ≈ 0.75 Å in O_h coordination) with respect to that of Ni^{2+} (≈ 0.55 Å in T_d and ≈ 0.69 Å and O_h coordination) [128,171]. It is worth of mention that the lattice parameters ***a*** are larger than expected considering the bulk values of ≈ 8.38 Å and ≈ 8.33 Å for pure cobalt and nickel ferrite, respectively [128,172,173], especially for sample MF5 (pure nickel ferrite).

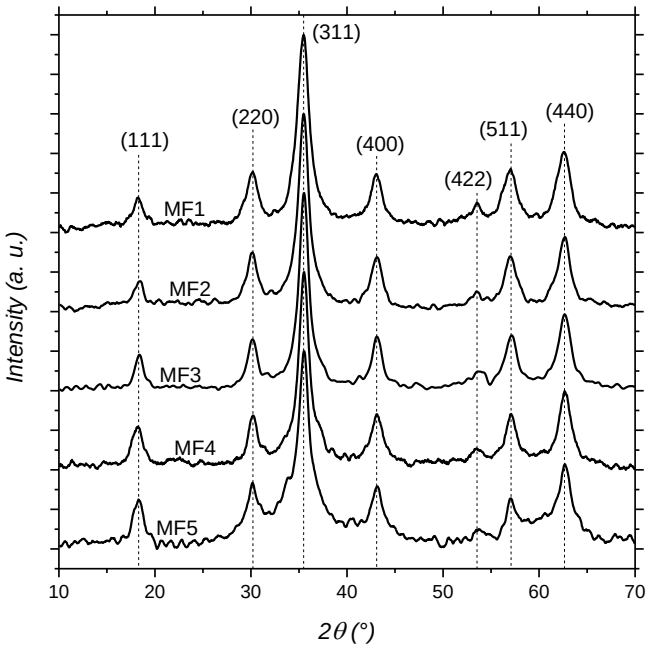

Figure 4.2: XRD patterns of all samples.

Sample	***Experimental Formula***	***<D_{XRD}> (nm)***	***a (Å)***	***<D_{TEM}> (nm)***	***PD (nm^{-1})***
MF1	$Co_{1.00}Fe_{2.00}O_{4.00}$	5.6(6)	8.394(4)	4.5(1)	2.0(1)
MF2	$Co_{0.60}Ni_{0.40}Fe_{2.00}O_{4.00}$	5.9(5)	8.387(4)	4.6(1)	2.4(1)
MF3	$Co_{0.40}Ni_{0.60}Fe_{2.00}O_{4.00}$	6.8(6)	8.378(4)	4.6(1)	2.4(1)
MF4	$Co_{0.30}Ni_{0.70}Fe_{2.00}O_{4.00}$	6.0(7)	8.378(4)	4.5(1)	3.3(1)
MF5	$Ni_{1.00}Fe_{2.00}O_{4.00}$	5.3(6)	8.375(4)	4.3(1)	3.3(1)

Table 4.1: Chemical formula by ICP analysis, mean coherent crystalline domain <DXRD>, lattice parameter a, mean diameter <DTEM>, and polidisperity (PD) evaluated by TEM images. Uncertainties on the last digit are given in parentheses.

TEM images (**figure 4.3**) show high crystalline spherical-like particles with a high degree of aggregation, visible in particular in sample MF5 (**figure 4.3g**). Electron diffraction confirms the presence of a unique spinel phase (a representative example is shown in **figure 4.3f** for sample MF1). Particle size distributions (symbols in **figure 4.3g**) are well fitted by using lognormal functions for all the samples (lines in **figure 4.3g**), showing a relative low polydispersity ranging from 2.0 nm^{-1} for MF1, to 3.3 nm^{-1} for MF5. The mean particles size extracted by TEM are equal for all the samples ($<D_{TEM}> \approx 4.5$ nm), slightly lower that mean crystallite size extracted by XRD ($<D_{XRD}> \approx 5.5$ nm). In order to clarify whether this disagreement can be attributed to the background produced by the organic phase, and/or the strain effect, an estimation of the magnetic diameter has been obtained by the activation volume V_{act} (see **Paragraph 4.5.2** for details). For sample MF3, the one with the largest difference between XRD and TEM diameter, the magnetic viscosity S was measured in the range of the reversal field $\mu_0 H_{rev}$, between 0.2 T and 1.2 T, being the coercivity 0.50 T (see **notes 4.5.2**, **figure 4.7**). Assuming a system composed of spherical particles, the obtained $V_{act.}$ corresponds thus to a mean magnetic grain diameter of 4.7(5) nm, in perfect agreement with TEM measurement of 4.6(1) nm. This result suggests that the larger XRD diameter can be due to the polyol coating (≈ 20 % in weight from TGA evaluation): the background produced by the organic phase can lead to underestimate the peak broadening and thus to overestimate the mean particles size.

ICP analysis provides an estimation of the chemical composition (**table 4.1**) that is almost ideal for all the samples, except for MF2 and MF4, which exhibit a difference with respect the theoretical values. This loss could suggest that there is a better configuration found with composition around a 50% of cobalt and nickel atoms. Similar small deviation toward 50% composition have been already established by other authors [168], anyway a monotonic variation of composition is observed going from sample MF1 to sample MF5.

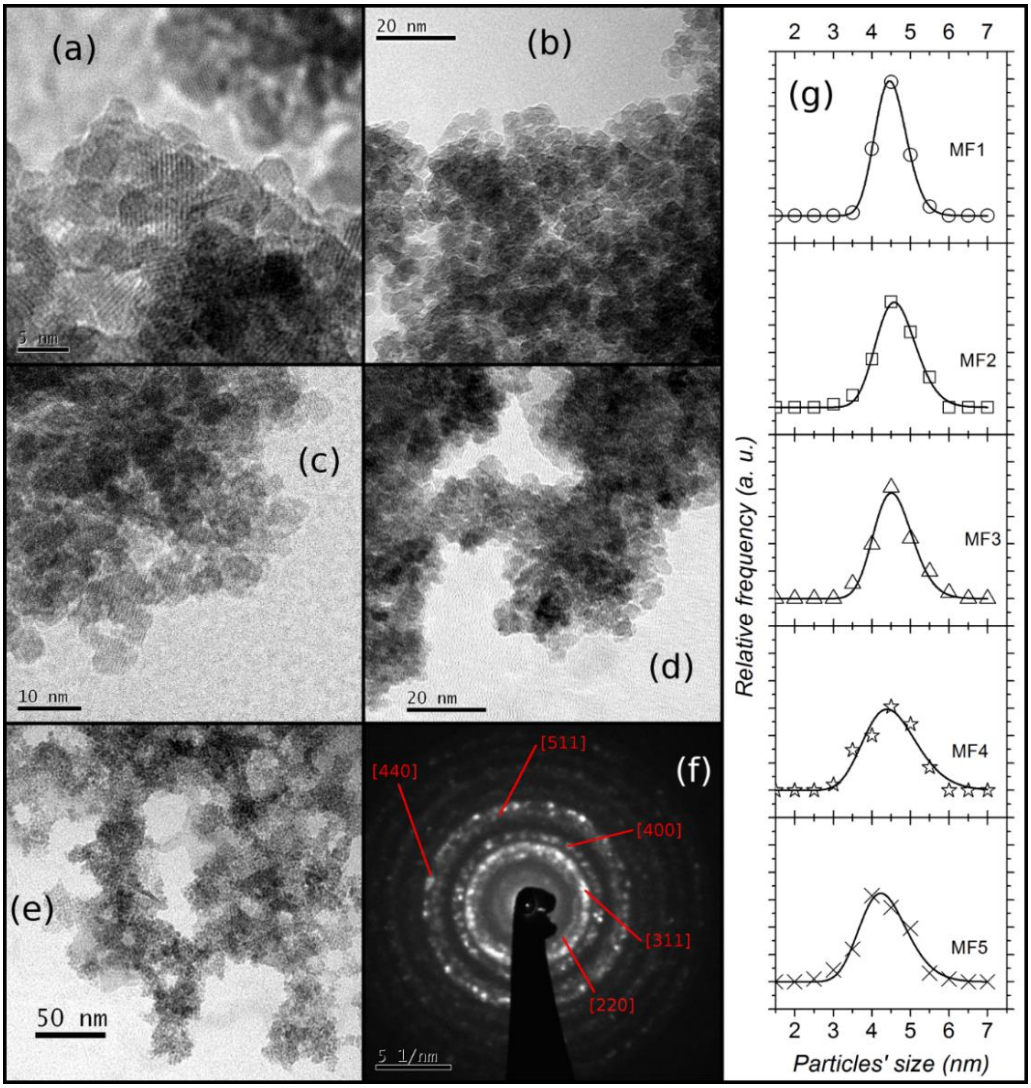

Figure 4.3: TEM images of samples MF1 (a), MF2 (b), MF3 (c), MF4 (d), and MF5 (e). Panel (a) represent an example of the high crystalline nature of the samples; for sample MF1 is also reported an electron diffraction analysis (f) which perfectly matches with the crystalline structure of spinel cobalt ferrite. Particles are quite aggregated in particular for sample MF5 (e). Panel (g) reports the particles' size distributions of all samples.

4.2 Magnetic Properties

All samples own high crystalline spherical particles with the same average size, within the experimental error, therefore, any difference in magnetic properties can be ascribed to the effect of the chemical composition.

At a temperature of 5 K, all samples behave as blocked ferrimagnets (**figure 4.4**); a significant decrease of the magnetic anisotropy is observed with the increase of cobalt content, as shown by the monotonic decrease of the coercive field ($\mu_0 H_C$) and of the saturation field ($\mu_0 H_{SAT}$) (**table 2**). Cobalt ions produce a marked magneto-crystalline anisotropy far above that of nickel and iron ions, indeed its orbital magnetic moment is not quenched by the crystal field, and a spin-orbit coupling occurs, particularly strong for Co^{2+} ions in octahedral sites [142,157,174]. Bulk $CoFe_2O_4$ crystals, have a strong cubic magnetic anisotropy, but such behavior is usually suppressed with particles size under 5 nm, and an uniaxial anisotropy is observed [43,44]. The reduced remanence magnetization (M_R/M_S) should be ≈ 0.8 and 0.5 for cubic and uniaxial anisotropy, respectively [3,44–46]. Analyzing the M_R/M_S value of sample MF1, only a small tendency towards cubic anisotropy is shown, furthermore, reducing the cobalt content, a reduction of M_R/M_S values is observed. The very low value of ≈ 0.29 measured for MF5 could be assigned to the frustrated surface spins [44], or due to the effect of strong dipolar interactions on a relative soft material [177]. On the other hand, due to the distribution of values of magnetic anisotropy energy, it is not possible to exclude that a fraction of particles is in the superparamagnetic state even at 5 K (temperature used for the measurement), thus reducing the M_R/M_S values.

In the simplest approximation of Stoner and Wohlfarth [41] (i.e., single particle with uniaxial anisotropy), the relation between the anisotropy constant *K* and the anisotropy field $\mu_0 H_K$ can be defined as [28,178]:

$$K_{eff} = \frac{\mu_0 H_K M_S}{2} \qquad (4.1)$$

Thus we can roughly estimate the effective anisotropy constant with the same formula, assuming negligible the deviation toward cubic anisotropy and the influence of interparticles interactions [149,179], and considering $\mu_0 H_{sat} \approx \mu_0 H_K$ [93,149]. The estimated values show again a downward tendency with decreasing of Co content

(**table 4.2**), and all of them are higher than those reported for bulk and nanostructured cobalt (≈ 1 – 4 · 10^5 J m^{-3} [149,179,180]) and nickel ferrites (≈ 1 · 10^4 J m^{-3} [181,182]). It is interesting to note, that the susceptibility measured at 5 T, which is usually considered as an evaluation of the surface component of anisotropy [93], follows the same trend of the effective anisotropy. Furthermore, the ratio between the susceptibility at 5 T and the effective anisotropy is ≈ 2 · 10^{-6} for all samples, except for MF5, for which is ≈ 7 · 10^{-6}, suggesting a much higher degree of frustration in its magnetic structure.

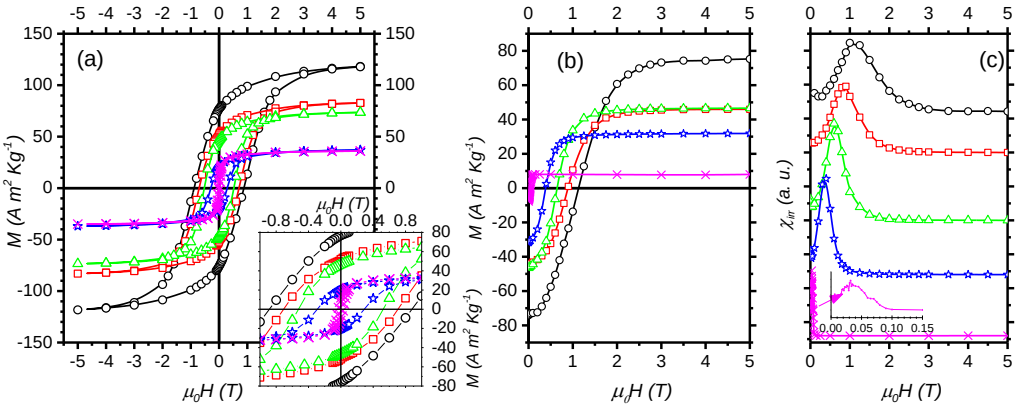

Figure 4.4: The field dependence of magnetization (a), the DCD curves (b) and the Switching Field Distributions (c) for sample MF1 (circles), MF2 (squares), MF3 (triangles), MF4 (stars), and MF5 (crosses).

The switching field distribution (SFD, see **appendix 8.2.3**) [70] of the samples is reported in **figure 4.4c**, giving a qualitative estimation of the energy barrier distribution. Confirming the picture described by M Vs H curves, the average anisotropy energy is reduced by reducing the Co amount with a monotonic tendency.

Sample	M_S (A m^2 kg^{-1})	M_R/M_S	$\mu_0 H_C$ (T)	$\mu_0 H_{SAT}$ (T)	K_{eff} (J m^{-3})	$dM/d\mu_0 H$ 5T (A m^2 kg^{-1} T^{-1})
MF1	130(10)	0.61(7)	0.88(7)	3.1(8)	10.7(1) · 10^5	2.31(1)
MF2	87(4)	0.59(4)	0.71(4)	2.7(1)	6.2(1) · 10^5	1.20(9)
MF3	77(4)	0.61(4)	0.50(1)	2.4(3)	4.9(1) · 10^5	0.79(2)
MF4	39(5)	0.52(8)	0.30(1)	2.0(2)	2.1(1) · 10^5	0.56(3)
MF5	37(4)	0.29(6)	0.028(1)	0.3(1)	0.30(1) · 10^5	0.22(1)

Table 4.2: Saturation magnetization (M_S); reduced remanence magnetization (M_R/M_S); coercive field ($\mu_0 H_C$); saturation field ($\mu_0 H_{SAT}$); effective anisotropy constant (K_{eff}); and the susceptibility at 5 T measured at 5K ($dM/d\mu_0 H$). Uncertainties on the last digit are given in parentheses.

Assuming the spin-only magnetic moment values of 5 μ_B for Fe^{3+}, 3 μ_B for Co^{2+} and 2 μ_B for Ni^{2+} resulting from their electronic configuration [168,183], and considering the antiparallel arrangement of moments between tetrahedral and octahedral sites in spinel structure, the magnetization is expected to decrease when reducing the Co content to increase the Ni one. As listed in **table 4.2**, the experimental values of saturation magnetization confirm this hypothesis. It is worth to mention that MF1 possesses a high magnetic saturation compared to that of bulk (≈ 83 - 90 A m^2 Kg^{-1}) [148], and also to those reported for highly crystalline cobalt ferrite nanoparticles [111]. On the other hand, a relatively low value is estimated in the case of MF5 (M_S of bulk ≈ 55 A m^2 kg^{-1} [184]). In this framework, the interplay between inversion degree and magnetic disorder (i.e., magnetic structure) can play a key role [6,183].

4.3 Magnetic Structure

In order to understand the evolution of magnetic properties with the chemical composition of the materials, a careful investigation of magnetic structure has been performed by ^{57}Fe Mössbauer spectroscopy in presence of intense magnetic field.

Figure 4.5 compares the ^{57}Fe Mössbauer spectra recorded at 10 K under a magnetic field of 8 T applied parallel to the γ-beam on the MF1, MF3 and MF5 samples. The spectra are consistent with a well-blocked ferrimagnetic structure without any

superparamagnetic relaxation state. The hyperfine parameters does not evidence at all the presence of Fe^{2+} ions, and the isomer shift values allow to attribute clearly the two sextets to the Fe^{3+} in tetrahedral and octahedral sites, consistent with a spinel ferrimagnetic structure (**table 4.3**), and to estimate their respective proportions from the relative absorptions areas.

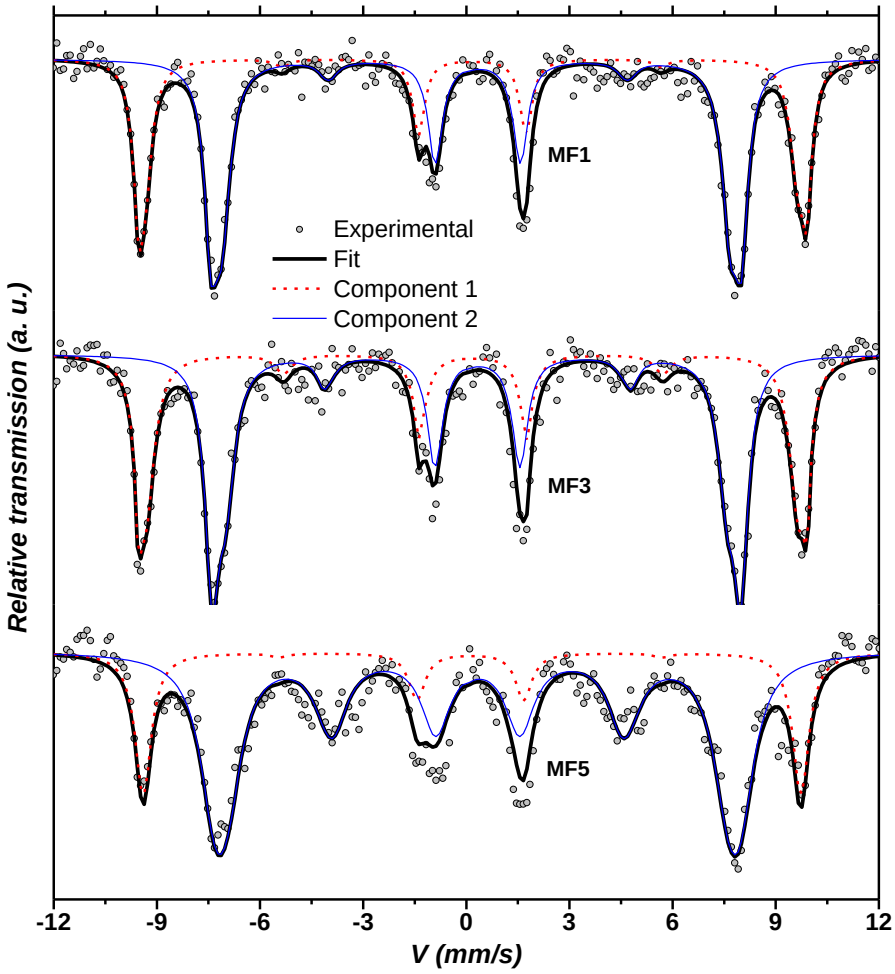

Figure 4.5: In-field Mössbauer spectra recorded at 10 K under an applied magnetic field of 8 T parallel to the γ-beam, for MF1, MF3 and MF5 samples. The experimental data are represented as circles, the fit as a bold line, while the two Fe_{Th} and Fe_{Oh} components are reported as a dashed and a thin line, respectively.

From the modelling of the in-field Mössbauer spectrum the effective field B_{eff} and the angle ϑ (angle defined by the direction of the effective field and the γ-beam direction) have been estimated for both tetrahedral and octahedral iron components, allowing thus their respective hyperfine field B_{hyp} to be calculated (**table 4.3**). A non-zero intensity is shown by the second and fifth lines for both components, evidencing a canted structure for Fe^{3+} magnetic moments with respect to the applied field (non-collinear magnetic structure) [100,101], with the respective canting angle ϑ reported in **table 4.3** (see **2.3 notes** for details on the estimation procedure). It is worth of mention that an asymmetrical broadening of the lines in O_h sites for sample MF5 was observed, probably due to the chemical disordered occupation of these sites, producing a wide range of possible chemical environments of Fe ions.

Sample	*Site*	δ (mm s^{-1})	ε (mm s^{-1})	B_{eff} (T)	B_{hyf} (T)	θ (°) ±10°	$Fe^{3+}_{A,B}$ / Fe^{3+}_{total}
MF1	Fe^{3+}_A	0.34(1)	-0.01(1)	59(2)	51(2)	10	0.37(1)
	Fe^{3+}_B	0.48(1)	-0.05(1)	47(2)	54(2)	18	0.63(1)
MF3	Fe^{3+}_A	0.35(1)	-0.01(1)	59(2)	51(2)	18	0.39(1)
	Fe^{3+}_B	0.48(1)	-0.03(1)	46(2)	54(2)	22	0.61(1)
MF5	Fe^{3+}_A	0.35(1)	-0.05(1)	59(2)	51(2)	12	0.22(1)
	Fe^{3+}_B	0.48(1)	-0.00(1)	46(2)	53(2)	38	0.78(1)

Table 4.3: The isomer shift (δ), quadrupole splitting (ε), effective field (Beff), hyperfine filed (Bhyf), average canting angle (θ), and the ratio of each component evaluated by fitting the in-field Mössbauer spectra, are reported for samples MF1, MF3 and MF5. Uncertainties on the last digit are given in parentheses.

According to the absorption area ratio of the two sextets, the accurate value of the atomic distribution of Fe^{3+} between T_d and O_h sites has been estimated assuming the same values of the recoiless f Lamb-Mössbauer factor for these two species (**table 4.3**). ICP analysis has confirmed the 2:1 ratio between Fe^{3+} and divalent cations (i.e., Co^{2+} and Ni^{2+}), thus, considering the hypothesis of absence of vacancies, and knowing the Fe occupancy of each site, the inversion degree γ has been estimated as the amount of

divalent ions in octahedral sites that should complete their occupancy. γ was calculated as 0.74(1) and 0.78(1) for MF1 and MF3, respectively, in agreement with values usually reported for cobalt ferrite (γ ≈ 0.7 - 0.8 [111,130,185]). For sample MF5 γ was estimated as 0.44(1), significantly different from what expected for pure nickel ferrite (γ ≈ 0.9 – 1) [130,186]. From these results, the cationic distribution was estimated. For Fe^{3+}, $Co^{2+}$and Ni^{2+} have been considered the magnetic moment values of 5 μ_B, 3 μ_B and 2 μ_B, respectively. For simplicity, for sample MF3 has been defined an equivalent divalent cation Me^{2+} formed by a population of 40 % of Co and 60 % Ni, according to ICP data, with an average moment of 2.4 μ_B. Finally, considering the effect of the canting angles, the corresponding theoretical magnetization saturation values have been calculated as 90(1), 78(1) and 89(1) A m^2 Kg^{-1}, for MF1, MF3 and MF5, respectively. Only for MF3 this value is comparable with the experimental one, for this reason, for the other two an unusual cationic distribution was hypothesized. A more representative effective inversion degree γ_{sat} has been calculated considering the effective magnetic moment per unit formula (μ_F^{exp}) calculated on the experimental saturation magnetization. This depends on the magnetic moment of each site by the relation:

$$\mu_F^{exp} = \left[\mu_{Fe-Oh}^{exp} + x \cdot \mu_{Me^{2+}}\right] - \left[\mu_{Fe-Td}^{exp} + (1-x)\,\mu_{Me^{2+}}\right] \qquad (4.2)$$

where μ_{Fe-Oh}^{exp} and μ_{Fe-Td}^{exp} represent the experimental magnetic moment of iron in O_h and T_d sites respectively, and $\mu_{Me^{2+}}$ represents the magnetic moment of the divalent cation, with x its population in O_h sites. x corresponds to the effective inversion degree γ_{sat} and can be evaluated rewriting equation (4.2):

$$\gamma_{sat} = \frac{\mu_F^{exp} - \mu_{Fe-Oh}^{exp} + \mu_{Fe-Td}^{exp} + \mu_{Me^{2+}}}{2\mu_{Me^{2+}}} \qquad (4.3)$$

Fixing the iron distribution in T_d and O_h sites according to Mössbauer results (Fe_{Td} and Fe_{Oh} , respectively), with the correction for their respective canting angles θ_{Td} and θ_{Oh} the effective magnetic moment of iron in T_d and O_h sites can be evaluated as $\mu_{Fe-Oh}^{exp} = 5\mu_B\, cos(\vartheta_{Td})\, Fe_{Td}$ and $\mu_{Fe-Td}^{exp} = 5\mu_B\, cos(\vartheta_{Oh})\, Fe_{Oh}$. Thus, considering an

experimental error of ± 10° for the canting angle [166,187], the values of inversion degree have been calculated as γ_{sat} = 1.00(2), 0.78(2) and 0.00(2), for MF1, MF3 and MF5, respectively. The value for MF3, close to that estimated from in-field Mössbauer spectra, leads to the effective formula $(Co_{0.12}Ni_{0.10}Fe_{0.78})[Co_{0.28}Ni_{0.50}Fe_{1.22}]O_4$, where the parentheses indicate the tetrahedral coordinated cations, and the brackets the octahedral ones. The value of γ_{sat} = 1.00(2) for sample MF1 is translated in the formula $(Fe_{0.74}\square_{0.26})[Co_{1.00}Fe_{1.26}]O_4$, with vacancies in T_d sites and a overpopulation of O_h sites that can justify such elevated value of $M_S \approx 130$ A m^2 Kg^{-1}. This 13 % overpopulation of octahedral Fe introduces only small distortions which are not visible in XRD pattern, but it can explain the slight increment in the lattice parameter with respect the bulk value [188]. The result for sample MF5 leads to the formula $(Ni_{1.00}Fe_{0.44})[Fe_{1.56}\square_{0.44}]O_4$ explaining at the same time the low saturation and the unusual iron distribution from Mössbauer spectrometry. This unusual overpopulation of tetrahedral sites (≈ 44 %) finds a correlation with the quite large lattice parameter (≈ 8.37 Å *versus* 8.33 Å of bulk), although this parameter remains strongly dependent on the synthesis conditions.

These cationic distributions allow to estimate the environment surrounding the Fe^{3+} ions and to explain the measured canting angles. In a spinel ferrite structure each tetrahedral (Fe^{3+}) is surrounded by 12 nearest-neighbors octahedral ions, while an octahedral [Fe^{3+}] ion owns only six tetrahedral nearest-neighbors [189]. As illustrated in **figure 4.6**, we can assume a statistical average environment for each site of samples MF1, MF3 and MF5, involving also the presence of the vacancies. According to the molecular field theory, the superexchange (SE) interaction energy $J_{Td\text{-}Td}$ and $J_{Oh\text{-}Oh}$ are negligible compared to the $J_{Td\text{-}Oh}$ [190]. Thus, in first approximation, considering the energy of Fe^{3+}–O^{2-}–Co^{2+} , comparable to that of Fe^{3+}–O^{2-}–Ni^{2+}, and equal to $J_{Td\text{-}Oh}^1$ = 13.7 K, and for Fe^{3+}–O^{2-}–Fe^{3+} as $J_{Td\text{-}Oh}^2$ = 20.1 K [161,189], we can qualitatively estimate the SE energy for Fe^{3+}. For sample MF1 the SE energy allows an average canting of ≈ 10° for (Fe^{3+}). The lower SE energy for [Fe^{3+}] is the origin of its higher values of canting (≈ 18°). MF3 sample owns a smaller difference between the SE energy of the two sites, which is responsible of the close and relatively high values of ≈ 18° and ≈ 22° for (Fe^{3+}) and [Fe^{3+}], respectively, where the last one owns the lower SE energy and the higher canting angle. Finally, in sample MF5 the large presence of vacancies around (Fe^{3+}) produces a low SE energy giving rise to a canting of ≈ 18°; furthermore the low amount of iron in tetrahedral sites produce an even lower SE energy for [Fe^{3+}], resulting in a strong canting angle of ≈ 38°. This increase of magnetic disorder observed going from MF1 to

MF5 samples can be then ascribed to cationic distribution, influencing chemical surrounding of the iron atoms.

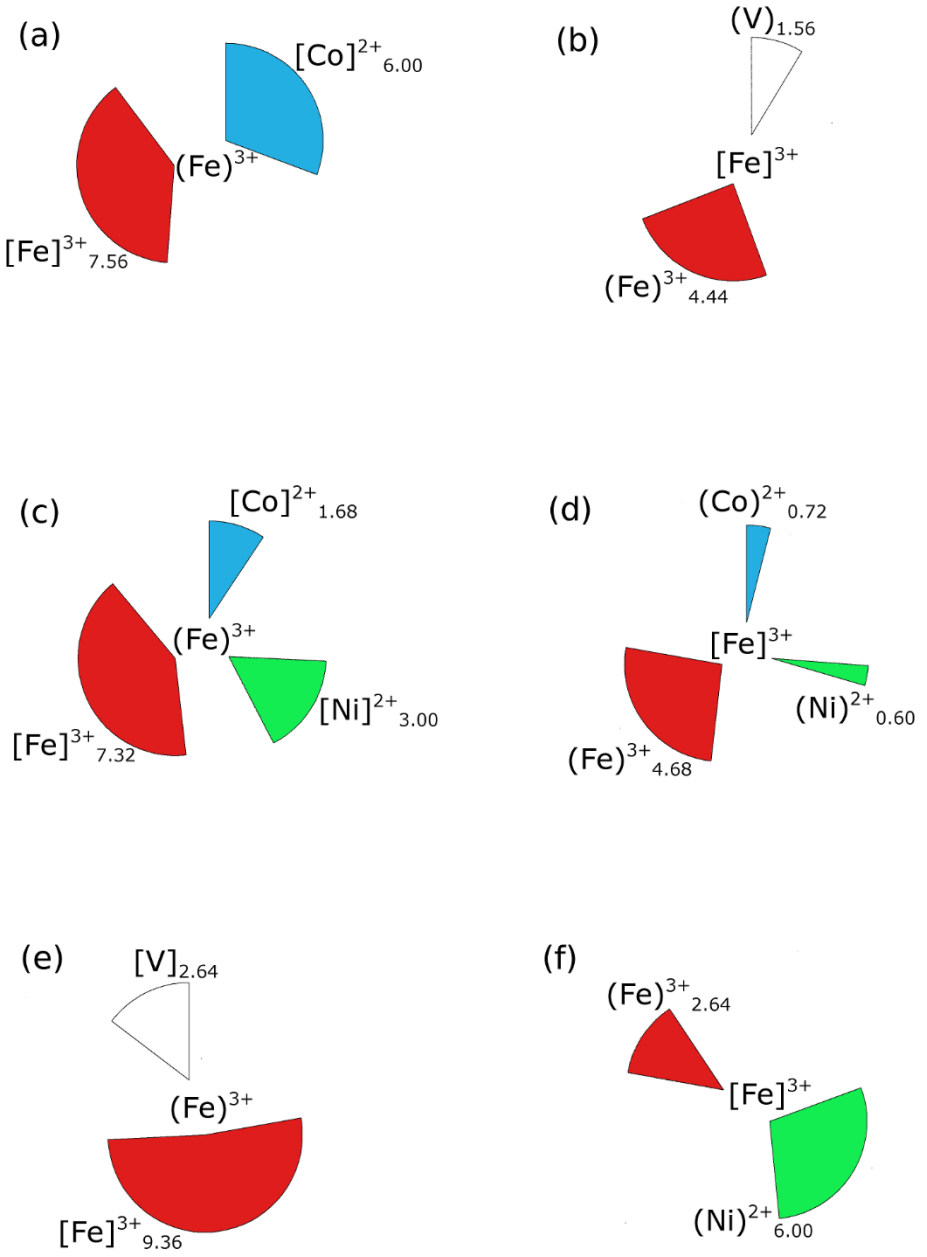

Figure 4.6: The nearest-neighbors for tetrahedral (Fe^{3+}) and octahedral [Fe^{3+}] is graphical schematize for sample MF1 (panels a and b respectively), MF3 (c and d) and MF5 (e and f).

4.4 Conclusions

The properties of spinel ferrites are directly related to their chemical composition. In this work it is shown how it is possible to finely tune the magnetic behavior in Ni-Co ferrite nanoparticles by controlling the chemical composition, beyond the effect of the particle size. The evolution of the magnetic behavior with respect to the different chemical composition has been provided both by M *versus* H and DCD and their derivative curves. It is clear that increasing the cobalt content, a stronger magnetocrystalline anisotropy was produced, and higher saturation magnetization is obtained. To study the magnetic structure of the samples, and in particular to understand the unusual saturation magnetization of samples Co_{100}-Ni_0, Co_{50}-Ni_{50} and Co_0-Ni_{100}, ^{57}Fe Mössbauer spectrometry under intense magnetic field was employed. The cationic distribution between the two Fe sublattices has been estimated, and, matching this information with the saturation magnetization, it was possible to propose a cationic distribution for T_d and O_h sites, with the presence of vacancies and an unusual overpopulation of specific sites. In addition, a spin canted structure was evidenced and explained in terms of superexchange interactions energy produced by the average cationic distribution and vacancies in the spinel structure. This study represents an example of further development in the understanding of the link between the structure and magnetic behavior of ferrite nanoparticles beyond the volume effect. This is of fundamental importance for the development of the engineering of magnetic ferrite nanomaterials for technological applications.

4.5 Notes

4.5.1 Synthesis

All samples were prepared by polyol process [62,186,191], where polyol acts as solvent, reducing agent and surfactant. This method allows to produce a wide range of pure metals and oxides [192,193], with the possibility to tune their chemical composition. In a typical synthesis of $CoFe_2O_4$ (MF1 sample) 2 mmol of iron (III) nitrate nonahydrate (Sigma Aldrich, > 98 %), 1 mmol of cobalt (II) nitrate exahydrate (Sigma Aldrich, 98 %) and 1 ml of distilled water were added to 100 ml of tri-ethylene glycol (TEG, Sigma Aldrich, 99 %) in a round bottom tree-neck flask. The solution, was heated in a mantle to the boiling point and kept under reflux for 2h, using a condenser and mechanical agitation; then it was cooled to room temperature. With the addition of acetone to the solution, the precipitation of a black powder was induced. The product was washed

again with acetone and separated via centrifuge; this procedure was repeated three times, and finally the powder was dried in an oven at 60°C overnight. For all samples, the same procedure has been employed, changing the relative amount of precursors, to obtain the desired nominal composition (**Table 4.1**).

4.5.2 Activation volume

For the study of the low temperature dependence of the magnetic viscosity with respect an external field, the sample was brought at 5 K to a positive saturation field (5 T); then a reverse negative field ($\mu_0 H_{rev}$) was applied and the time dependence of magnetization was measured. *M* versus *t* was investigated, and a logarithmic decay of the magnetization was found according to:

$$M(t) = M_0 - S\ln(t) \qquad (4.4)$$

where *S* is the magnetic viscosity [194]. By fitting the data with equation (4.4), *S* was estimated at different values of the reverse field. By combining the maximum value of magnetic viscosity (S_{max}) with the irreversible susceptibility (χ_{irr}), calculated at the same field from DCD curve, an estimation of the fluctuation field ($\mu_0 H_f$) was obtained:

$$\mu_0 H_f = \frac{S_{max}}{\chi_{irr}} \qquad (4.5)$$

Then the fluctuation field can be used to estimate the activation volume ($V_{act.}$) [194–196], which can be defined as the smallest volume of material that coherently reverses in a single event [196]:

$$V_{act} = \frac{k_B T}{M_S H_f} \qquad (4.6)$$

where k_B is the Boltzmann constant.

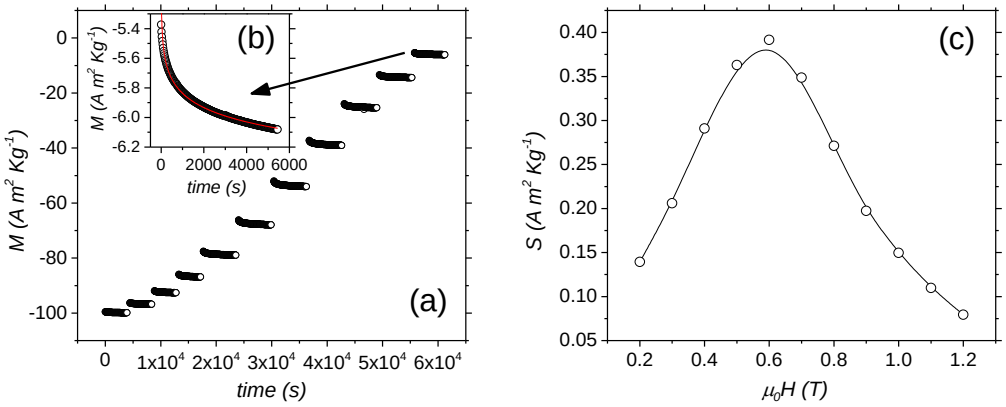

Figure 4.7: For sample MF3, the time dependence of the magnetization reversal is reported in panel (a), with different applied field. For 1.2 T of applied field the experimental data (circles) and the best fit (continuous line) using equation (8.7) are reported in inset. The magnetic viscosity measured at each field is reported in panel (b).

4.5.3 **Surfactant arrangement**

In order to study the interaction of TEG on nanoparticles the FT-IR spectra of the samples (**figure 4.8**) have been analyzed. The presence of spinel ferrite structure is confirmed by the signals around 590 cm^{-1}, referred to the stretching vibration of the metal in tetrahedral site and the oxygen, while the signal around 400 cm^{-1} is analogous for the octahedral site [56,108]. The symmetrical and asymmetrical stretching of C-H (signals between 2937 and 2868 cm^{-1}), and of C-O (around 1100 cm^{-1}) confirm the polyol coating in all samples [63]. In particular, the interaction between polyol oxygen and metal cations at particles surface finds evidence both in the small shift to lower frequencies of the C-O signals with respect to the pure polyol [107], and in their different intensity profile [106,109], with two signals in place of the small three of the pure TEG. The signals around 3400 and at 1646 cm^{1} are referred to the stretching and bending modes of O-H of polyol and adsorbed water [63], respectively. Finally, the complex profile between 1450 and 1250 cm^{-1}, produced by C-H bending [18], has different intensity and shape with respect free TEG, as results of interactions between polyol and NPs surface.

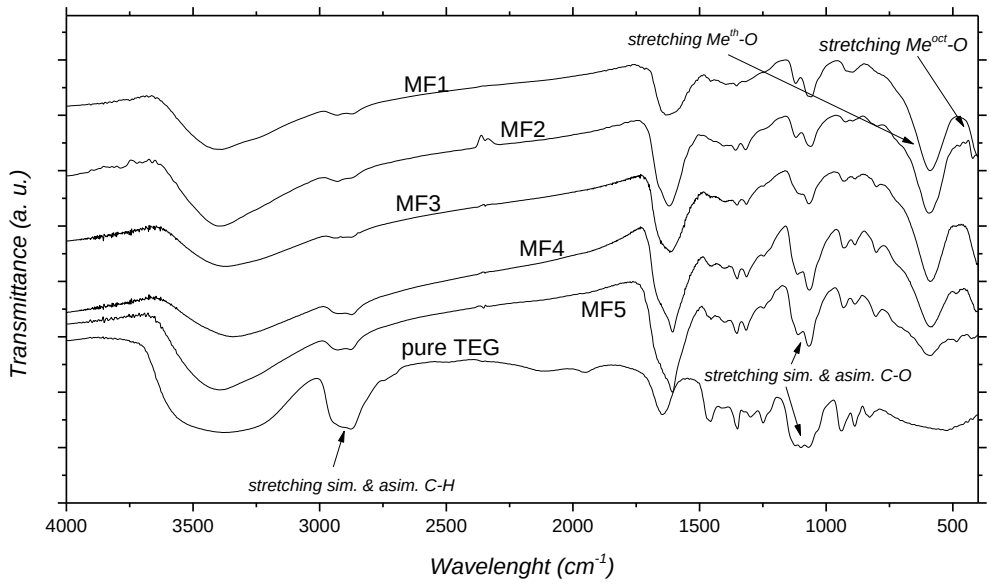

Figure 4.8: FT-IR spectra of all samples and pure TEG for comparison.

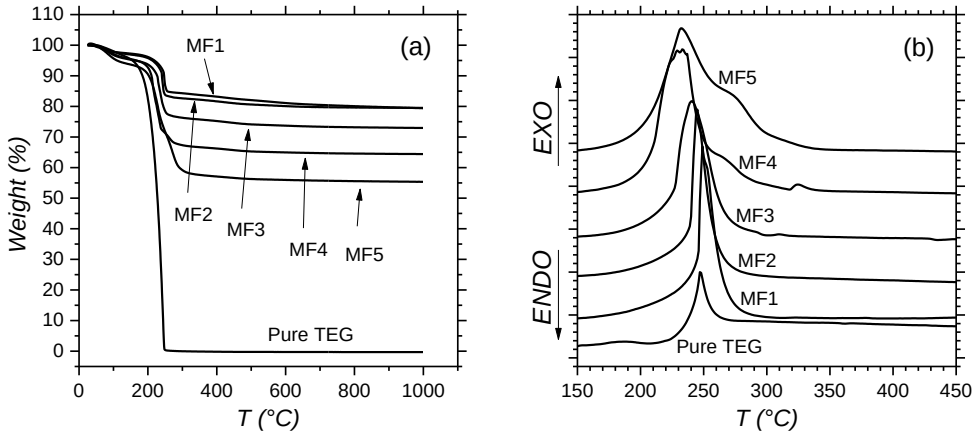

Figure 4.9: Panel (a) reports TGA curves for all samples and pure TEG. The corresponding SDTA curves are shown in the region around 250°C, in panel (b).

Figure 4.9 compares the TGA-SDTA curves of all samples. For each one a small loss in weight, with a corresponding endothermic event, is completed around 100 °C; it is produced by the evaporation of residual water and acetone. The successive main loss around 250 °C is coupled with an exothermic peak, and it is due to decomposition of TEG (decomposition temperature centered at 247 °C for pure TEG). It is worth of mention, that this loss increases with respect the amount of nickel. Suggesting again a stronger interaction between polyol and Ni at particles surface. MF1 shows the corresponding DTA peak centered around 250 °C; for MF2 and MF3, this peak becomes bigger, reflecting the larger amount of adsorbed TEG, and it moves toward 240 °C. For MF4 and MF5 there is a clear first peak around 230°C and a second around 270 °C. These data suggest that the amount of polyol present in MF1 (≈ 13 %) forms a complete single layer of TEG, further amount is not directly bonded at particle surface, and so it decomposes at lower temperature. In addition, in MF4 and MF5 the double peak signal can be associated to a double layer structure, where the first decomposition is related to the external one, while the second inner layer, directly bonded on the particles surface, and protected by the outer shell, decomposes at higher temperature.

Sample	*Polyol (%)*
MF1	13(1)
MF2	14(1)
MF3	19(1)
MF4	27(1)
MF5	36(1)

Table 4.4: For each sample, the amount of polyol evaluated by TGA is reported.

Chapter 5
Competition between single particle anisotropy and interparticles interactions

For monodomain particles of volume *V*, the magnetic anisotropy energy determinates the behavior of the system. The effective anisotropy constant is influence by several contributions such as particles shape, surface distortion of crystalline structure, stress or strain effects, but usually the most important role is acted by the magnetocrystalline contribution. In the previous chapter, we have analyzed the effect of the cobalt and nickel content in a set of spinel ferrite nanoparticles, showing how the magnetocrystalline anisotropy induced by single ion contribution dominates the system behavior. On the other hand, in several magnetic nanoparticles applications, the interparticles interactions cannot be neglected. One can estimated the rough contribution of interparticles dipolar interactions as [43]:

$$E_{dip} \approx \frac{\mu_0}{4\pi}\frac{\mu^2}{d^3} \qquad (1.12)$$

where μ represents the dipolar moment and d the average interparticles distance. Such term adds a relevant contribution to the effective anisotropy energy, deeply influencing the overall magnetic behavior [197]. In concentrated systems, e.g., for high-density magnetic data storage [198], or when high saturation magnetization is an important requisite, as for biomedical applications [12], collective relaxation behaviors or particles agglomeration, due to interactions, may represent a critical issue.

Within this framework, the study of the inter-correlated effect of the single particles anisotropy energy and the interparticles dipolar energy becomes fundamental. Their competitive role will be analyzed in two samples of spinel iron oxides observed in the previous chapter. Samples MF1 ($CoFe_2O_4$) and MF3 ($Co_{0.4}Ni_{0.6}Fe_2O_4$) have been chosen for this study, having a clear different magnetic anisotropy due to the different composition, but similar structure, with particles in close proximity but coated by the

same polyol layer (avoiding exchange interactions), thus presenting comparable interparticles distances.

5.1 Morphostructural characterization

Both samples appear as ensembles of almost spherical particles, with a narrow size distribution centered at ≈ 4.5 nm (**figure 4.3**). They show a complete crystalline form, with XRD pattern (**figure 4.2**) perfectly matching the spinel cobalt iron oxide phase ($CoFe_2O_4$ PDF card 22-1086). The particles are strongly aggregated due to the presence of TEG, the weight of which has been estimated in ≈ 17 and ≈ 19 % for MF1 and MF3, respectively. The most important structural data are reported in **table 5.1**, for a detailed structural analysis see **paragraph 4.1**.

Sample	*Experimental Formula*	*<D_{TEM}> (nm)*	*PD (nm^{-1})*	*Polyol (%)*
MF1	$Co_{1.00}Fe_{2.00}O_{4.00}$	4.5(1)	2.0(1)	17.0(5)
MF3	$Co_{0.40}Ni_{0.60}Fe_{2.00}O_{4.00}$	4.6(1)	2.4(1)	19.0(5)

Table 5.1: For each sample the experimental formula evaluated by ICP analysis, the mean diameter <DTEM> and the polydispersity (PD), evaluated by TEM images, are summarized. From TGA analysis the % weight of polyol bonded to particle's surface has been calculated.

5.2 Evolution of magnetic behavior with chemical composition

As discussed in chapter 4, spinel ferrites own a FCC lattice of oxygen ions with Fe^{3+} and Me^{2+} cations in octahedral and tetrahedral site respectively. The magnetic coupling inside each site produces a parallel ferromagnetic alignment of spins, but the coupling between the two sub-lattices produces an antiparallel arrangement. Due to the different magnetic moment of the two lattices, a net magnetization emerges, producing a final ferrimagnetic ordering [35]. The specific nature of divalent cation produces different results, both in terms of saturation magnetization and magnetic anisotropy, in addition the possible substitution of Fe^{3+} in octahedral sites introduce a "inverse" structure with a further influence on magnetic properties [96,130].

The M Vs H curves of the two samples are proposed in **figure 5.1**, with data summarized in **table 5.2 .** As it has been discussed in **paragraph 4.2**, the reduction of the cobalt amount reduces the saturation magnetization of sample MF3 with respect to MF1. The experimental values of saturation magnetization are ≈ 130 and ≈ 77 A m^2 Kg^{-1} for MF1 and MF3, respectively. The lower saturation magnetization of MF3 is expected, considering the ferromagnetic structure of the ferrites, and assuming the values of $2\mu_B$ for Ni^{2+}, $3\mu_B$ for Co^{2+} and $5\mu_B$ for Fe^{3+}, as result of the electronic configuration. Matching the magnetic data and the Mössbauer analysis, the saturation magnetization were explained in **paragraph 4.3** with a cationic distribution of $(Fe_{0.74}\square_{0.26})[Co_{1.00}Fe_{1.26}]O_{4.00}$ and $(Co_{0.12}Ni_{0.10}Fe_{0.78})[\ Co_{0.28}Ni_{0.50}Fe_{1.22}]O_{4.00}$. MF3 presented an inversion degree γ ≈ 0.78, in agreement with what reported usually reported for cobalt ferrite (γ ≈ 0.7 - 0.8) [111,130,185]. On the other hand, the high value of saturation of MF1 (≈ 130 A m^2 Kg^{-1}) with respect the bulk (83 - 90 A m^2 Kg^{-1} [148]), found justification with its unusual cationic distribution.

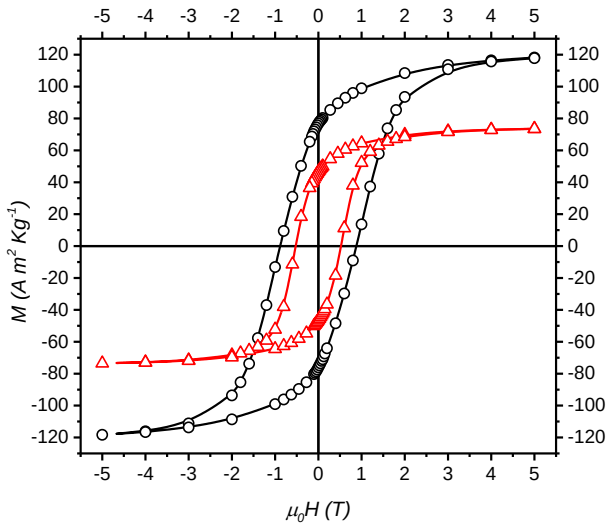

Figure 5.1: Magnetization Vs applied field for sample MF1 (circles) and MF3 (triangles).

Cobalt ions produce a marked magneto-crystalline anisotropy far above that of nickel and iron, indeed its orbital magnetic moment is not quenched by the crystal field, and a spin-orbit coupling occurs, particularly strong for Co^{2+} ions in octahedral sites

[142,157,174]. Reducing the amount of cobalt, the magnetic anisotropy decreases, and this is reflected by the coercive field $\mu_0 H_C$ and the saturation field $\mu_0 H_{SAT}$ (**table 5.2**). Also the susceptibility measured at 5 T, which is related to the anisotropy of the surface component [93], follows the same trend.

Sample	M_S ($A\ m^2\ kg^{-1}$)	M_R/M_S	$\mu_0 H_C$ (T)	$\mu_0 H_{SAT}$ (T)	$dM/d\mu_0 H$ at 5 T ($A\ m^2\ kg^{-1}\ T^{-1}$)
MF1	130(10)	0.61(7)	0.88(7)	3.1(8)	2.31(1)
MF3	77(4)	0.61(4)	0.5(1)	2.4(3)	0.79(2)

Table 5.2: For both samples the saturation magnetization (M_S), reduced magnetization (M_R/M_S), coercive field ($\mu_0 H_C$), saturation field ($\mu_0 H_{SAT}$), and the susceptibility of the high anisotropy component measured at 5 T ($dM/d\mu_0 H$) are reported.

However, the analysis of ZFC-FC curves (**figure 5.2**) suggests a different picture. Despite the reduction of magnetic anisotropy increasing the amount of nickel, T_{max} of ZFC remains almost constant for the two samples. The same behavior is shown by the blocking temperatures distributions (**figure 5.2**) obtained from the derivative of TRM curves, which are directly proportional to the anisotropy energy distribution (a detailed description is provided in **appendix 8.2.1**). In order to better analyze the thermal switching behavior of the samples, Mössbauer spectroscopy analysis has been carried out (**figure 5.3**, data summarized in **table 5.3**). The fraction of particles magnetically blocked for the interval of measurement of Mössbauer technique, is represented by a sextet, while the SPM component produces a doublet (see **paragraph 2.2** for details). It is interesting to note that the fraction of blocked particles at room temperature, leads to similar values for both samples, as for T_B measured by ZFC curves, in contradiction with the anisotropy behavior evinced from M Vs H curves.

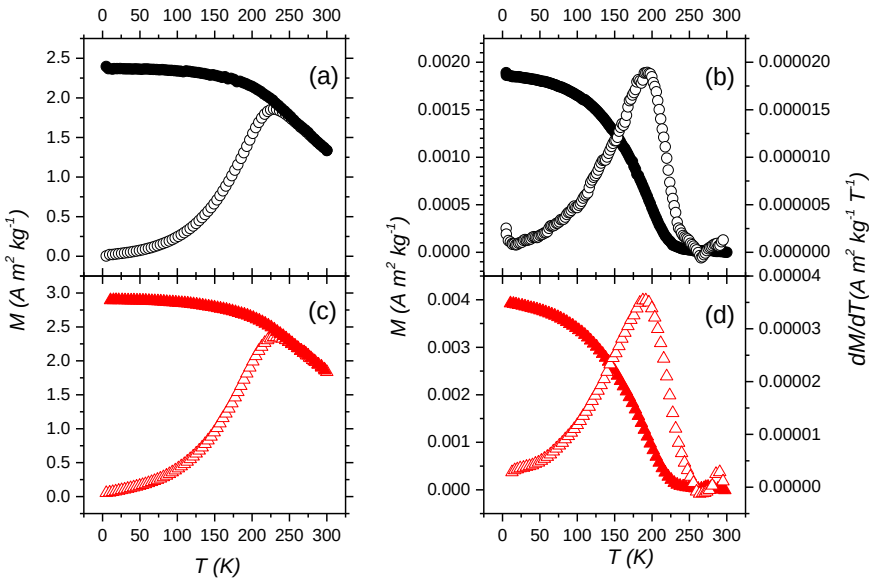

Figure 5.2: ZFC (empty symbols) and FC (full symbols) for sample MF1 (a) and MF3 (c). The TRM curves and their derivative, represented as full and empty symbols, respectively, are shown in panel (b) and (d) for sample MF1 and MF3, respectively.

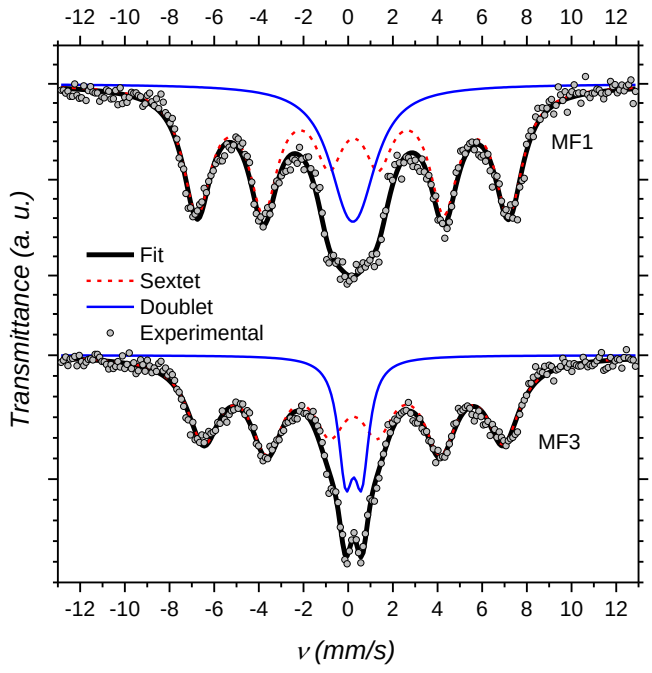

Figure 5.3: Mössbauer spectra at room temperature. The small circles represent the experimental points, while the sextet, the doublet and the total fit are described as dashed, thin and bold lines, respectively.

Sample	T_{max} *(K)*	T_{irr} *(K)*	T_B *(K)*	*Mössbauer blocked fraction at 300 K*
MF1	229(4)	255(4)	174(2)	75(1) %
MF3	231(4)	255(4)	170(2)	82(1) %

Table 5.3: From ZFC-FC curves T_{max} , T_{irr} and the mean blocking temperature TB are reported. Fitting Mössbauer spectra, the perceptual blocked fraction of particles at room temperature is extrapolated

5.3 Interparticle interactions

The interparticles interactions can deeply affect the "blocking" behavior of nanoparticles. In order to clarify this aspect ΔM-plot have been analyzed (**figure 5.4**) (**appendix 8.2.3** for details). The two samples exhibit an interacting behavior, with a strong negative deviation, originated by the prevalence of dipolar interactions. The reversal field and its intensity decrease with respect the amount of cobalt, as expected considering the dipolar interaction energy roughly evaluated as [43]:

$$E_{dip} \approx \frac{\mu_0}{4\pi}\frac{\mu^2}{d^3} \qquad (1.12)$$

where μ is the magnetic moment of single particle and d the distance between particles center (considered as point dipole). The results, scaled for k_B, are reported in **table 5.4**, and represent a roughly estimation of the temperature below which the dipolar interactions can result in an ordering of magnetic moments [43]. From this parameter, stronger interactions emerges for MF1, which cannot justify the similar blocking temperature for both samples.

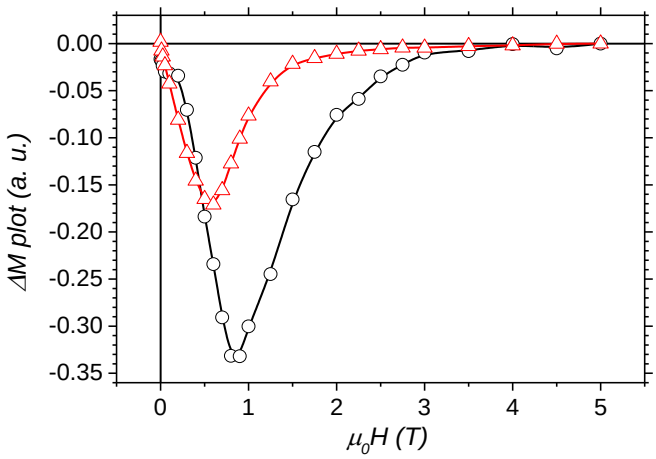

Figure 5.4: ΔM-plot of sample MF1 (circles) and MF3 (triangles) are reported. The solid lines are a guide for the eyes.

Sample	$\mu_0 H_{rev}$ ***(T)***	I_{CM} ***(a. u.)***	E_{dip} / k_B ***(K)***
MF1	0.85(5)	-0.34(1)	44(1)
MF3	0.56(1)	-0.17(1)	12(1)

Table 5.4: From ΔM-plot the reversal field ($\mu_0 H_{rev}$) and the relative intensity of interactions (I_{CM}) are reported. The evaluation of dipolar interaction energy (E_{dip}) has been estimated using equation (1.12).

Very different anisotropy energy are evidenced for the two samples by the M Vs H curves, but measuring the ZFC-FC curves at low field (2.5 mT), and analyzing Mössbauer spectra with no applied magnetic field, similar blocking energy are exhibited. Such results can be related to a kind of collective behavior induced by interactions, which create a condition of higher effective anisotropy, in particular for MF3. This emerges only under low field, and it is suppressed by the high field applied in M Vs H curves, where the single particle anisotropy dominates. To understand this complex behavior a modified Random Anisotropy Model is proposed.

5.4 Random Anisotropy Model

For a strongly correlated nanoparticles ensemble, the magnetic behavior is not only affected by the single particle anisotropy, indeed each particle experiences a random condition created by the surrounding environment. The random anisotropy model (RAM) is usually employed for polycrystalline samples with exchange interactions [199]. Anyway it works regardless the origin of interactions, exchange or dipolar, among particles, and it has been proposed, introducing some modifications, to describe nanoparticles embedded in a matrix [200], ensembles of nanoparticles with different concentration [201] and thin films of cobalt ferrite nanoparticles [202]. According to such modified model, the particles interact inside a correlation length *L* that describes a correlation volume *V* within which a number of particles *N* contributes with their magnetic anisotropy to create an average anisotropy condition. The anisotropy constant K_N for this volume of particles is lower than that of single particles (*K*), but due to the larger volume involved, the anisotropy energy ($E_a \propto K_N V$) of such entities is larger than that of the single particles. As the interparticle interactions increase, the correlation length expands, and the "cluster" anisotropy is mediated by a great number of particles, thus reducing its magnitude due to a statistical random walk effect. Furthermore, increasing the magnetic field reduces the correlation length, and prevents the "cluster" formation. For a non-interacting system the dependence of the blocking temperature from the field $\mu_0 H$ is described by the law [201,203]:

$$T_B = \frac{KV}{B}\left[1 - \frac{\mu_0 H}{\mu_0 H_K}\right]^{\alpha} \qquad (5.1)$$

with α = 1.5 [203], and *B* is a constant defined considering the experimental time in MPMS as τ_m = 10 s, $\tau_0 = 10^{-10}$ s and the Boltzman constant $k_B = 1.38065\ 10^{-23}$ J/K:

$$B = k_B \ln\left(\frac{\tau_m}{\tau_0}\right) = 3.49697 \cdot 10^{-22}\,\frac{J}{K} \qquad (5.2)$$

The anisotropy constant *K* can be evaluated using the relation:

$$K = \frac{M_S\, \mu_0 H_K}{2} \qquad (5.3)$$

where $\mu_0 H_K$ is the anisotropy field and M_S the saturation magnetization of the material. According to the modified RAM model, for an assembly of interacting particles we can modify the (5.1) considering the number *N* of correlated particles within a correlation volume V_N with the effective average anisotropy K_N [201,203]:

$$N = 1 + x\frac{(L^3 - D^3)}{D^3} \qquad (5.4)$$

$$V_N = \frac{\pi}{6}[D^3 + x(L^3 - D^3)] \qquad (5.5)$$

$$K_N = \frac{K}{\sqrt{N}} \qquad (5.6)$$

$$\mu_0 H_K^N = \frac{2K_N}{M_S} \qquad (5.7)$$

where *x* represents the perceptual volume concentration of magnetic phase and $\mu_0 H_K^N$ the effective saturation field for the *N* correlated particles. All these parameters are related to *L*, and so field dependent, according to the relation [201][204]:

$$L = D + \left[\frac{2A_{eff}}{M_S\, \mu_0 H + C}\right]^{1/2} \qquad (5.8)$$

where A_{eff} represents the interaction intensity [199], that for nanocrystalline alloys is the intergrain exchange constant A [200]. The parameter C was introduced for nanoparticles systems to overcome the divergence at $\mu_0 H = 0\ T$. It should take in count the influence of particles concentration on their interactions, assuming a value close to zero for clustered particles and the form $C \approx 2A_{eff} - M_S\, \mu_0 H$ for non-interacting particles [201,203]. Finally, the (5.1) can be re-written as:

$$T_B = \frac{K_N\, \mathrm{V}_N}{B}\left[1 - \frac{\mu_0 H}{\mu_0 H_K^N}\right]^{1.5} \qquad (5.9)$$

The T_B value has been measured from TRM curves at several applied magnetic fields, and the experimental values of T_B *Vs* H have been fitted with the relation (5.9) (**figure 5.5a**). All data are summarized in **table 5.5**. In a condition of zero applied field both samples have a correlation length larger than the single particle diameter, but only for sample MF3 this distance is longer than the distance in which two particles are included (L_{2NP}), considering also the amount of surfactant. Similar situation is present even with a low applied field of 2.5 mT, as for the measurement condition of ZFC-FC-TRM curves, supporting the thesis of a larger effective anisotropy visible only for MF3 in such measurements and Mössbauer spectra. Indeed, with an applied field of 2.5 mT, the correlated effective volume of magnetic material for MF1 and MF3 is ≈ 170 and 660 nm^3 respectively, then, despite a different single particles anisotropy, the average anisotropy energy within this volume is comparable, in the order of $6(1) \cdot 10^{-20}$ J. In this picture, MF1 appears as a strongly interacting sample, where the single particle anisotropy prevails. It shows stronger dipolar interactions, but the higher single particle anisotropy creates a correlation length not sufficient to induce cluster formation. On the other hand, MF3 has the right mix of lower anisotropy, long-range dipolar interactions, and inter-particle distance to produce a correlated state, at least until the applied field remains low. It is interesting to note that for MF3 the $\mu_0 H_{limit}$, the applied field which reduces the correlation length under the limit of L_{2NP} , is around 0.07(2) T (**figure 5.8b**). This explains why such effective anisotropy is visible only at low field. The analysis of M Vs H and ΔM-plot employ quite higher fields, which destroy the correlation length, thus allowing that the single particles anisotropy behavior emerges for both samples.

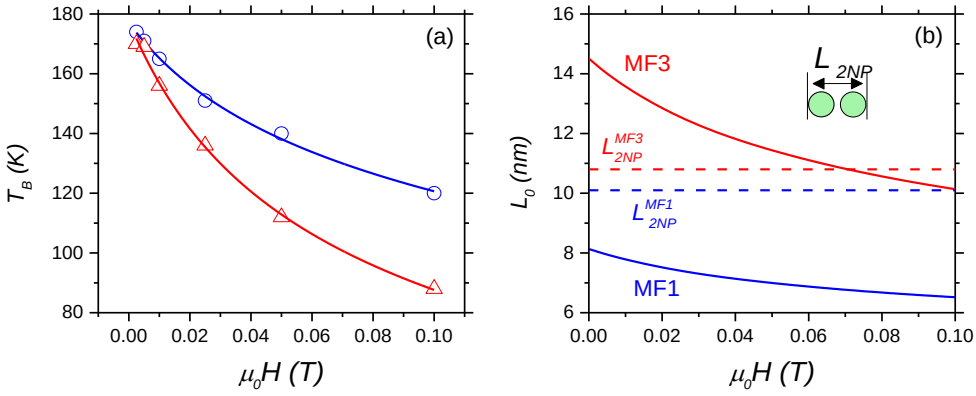

Figure 5.5: Panel (a) shows the dependence of the blocking temperature T_B with respect the applied field for sample MF1 (empty circles) and MF3 (empty triangles), with the RAM fits represented as solid lines. For each sample, the correlation length (L_0) dependence from the applied magnetic field is reported in panel (b), with the respective limit length which enclose two nanoparticles (L_{2NP}) represented as dashed lines.

	MF1	***MF3***
L_{2NP}	10.1(1) nm	10.8(1) nm
L_0 ($H = 0$ T)	8.1(1) nm	14.5(1) nm
L_0 ($H = 2.5$ mT)	8.0(1) nm	14.2(1) nm
$\mu_0 H_{limit}$	-	0.07(2) T

Table 5.5: The linear distance within two aligned nanoparticles, considering also the surfactant (L_{2NP}) is compared to the correlation length (L_0) extrapolated from RAM fits with an applied field of 0 and 2.5 mT. In addition, for MF3, it is reported the maximum field that produces a correlation length sufficient to involve two entire particles in the correlation volume.

5.5 Conclusions

The evolution of the effective magnetic anisotropy with respect the chemical composition was analysed in two samples of pure cobalt ferrite (MF1, $CoFe_2O_4$) and mixed cobalt-nickel ferrite (MF3, $Co_{0.4}Ni_{0.6}Fe_2O_4$) nanoparticles. The magnetization reversal process analyzed through M Vs H curves showed a strong reduction of the magnetic anisotropy introducing nickel in place of cobalt in MF3 sample. On the other hand, the thermal activated switching process of magnetization analyzed with ZFC-FC-TRM protocol with a low field of 2.5 mT, and the Mössbauer spectroscopy at 300 K without applied field, underlined a different picture, where almost the same anisotropy energy emerges for the two samples. The influence of interactions on the anisotropy energy was particularly strong for both samples, as underlined by ΔM-plots, but in first approximation the simple analysis of the dipolar energy did not explain this aspect. The interplay between the single particle anisotropy energy and the interparticles interactions is the key point to understand this ambiguous behavior. Developing a modified random anisotropy model for the two samples, it has been shown as the strong single particle anisotropy prevailed in MF1; on the other hand the right mix between the lower anisotropy and the quite long-range dipolar interactions has produced a correlate state in MF3, which exhibited a blocking temperature higher than expected. This correlation was reduced by the application of an external field, explaining why with an intense applied field the single particle anisotropy behavior emerges.

Chapter 6
Designing new exchange coupled nanocomposites

Transition metal oxides represent an interesting class of materials due to their cross correlated electronic and magnetic properties [205,206]. For example magnetic oxides have been shown to display many interesting (magneto)transport properties, such as the colossal magnetoresistance (CMR) [207], tunnel magnetoresistance (TMR) [208], electroresistance [209], as well as magnetodielectric [210] and magnetoelectric [211] effects. Magnetoelectric multiferroics appear very promising from a technological point of view due to the presence and coupling of ferroelectric with ferromagnetic behavior, permitting the control of the magnetic states using a simple electric field (and conversely inducing an electric polarization by a magnetic field) [212].

It was recently shown that composites including two or more transition metal oxides may be very attractive as their magnetic and electrical properties could be tuned or controlled owing to the interaction of its constituents. For example multiferroic and/or magnetoelectric properties were demonstrated in nanostructures consisting of $CoFe_2O_4$ pillars embedded in $BaTiO_3$ matrix [213] or $BiFeO_3$ pillars embedded in $CoFe_2O_4$ [214]. It was also found that the magneto-transport, and more particularly the tunnel magneto-resistance (TMR), can be tuned in composites formed of micrometer-scale mixtures of strongly correlated materials such as (La,Sr)MnO_3 and $CoFe_2O_4$ [215], owing to the dipolar field exerted by the $CoFe_2O_4$ particles onto the (La,Sr)MnO_3 ones. In another system comprised of Fe_3O_4-$CoFe_2O_4$ core-shell nanoparticles the TMR is dominated by the interface exchange coupling [208].

It is here proposed how to tune and improve the coupling between electrical and magnetic response of composites of strongly correlated oxides by combining the materials on the nanoscale. To prepare such nanocomposites, two synthetic strategies have been used: mechanical mixing of two different nanoparticle systems (N-MIX) and growing nanoparticles of one of the system around nanoparticles of the other (NC), in order to maximize the contact between nanomaterials. NC sample was prepared by a new synthetic approach, based on seed mediated growth self-combustion method.

We have chosen to combine nanoparticles of the well-known $La_{0.67}Ca_{0.33}MnO_3$ (LCMO) and $CoFe_2O_4$ (CFO) oxides, considering CFO-LCMO as a model system to illustrate our approach. It is important to note that sample MF1, in-depth analyzed in **chapters 4** and **5**, is here used as $CoFe_2O_4$. We present the complete structural and morphological characterization of N-MIX and NC as well as their magnetic and magnetotransport behavior to illustrate the relationship between morpho-structural features and physical properties. For the sake of clarity, a detailed description of the synthesis process to design such composite is proposed in the following sections. Further details on the calcination process and cobalt diffusion, and a full description of all magnetic characterization are proposed at the end of the chapter as **supporting information** in paragraph **6.6**.

6.1 Synthesis

6.1.1 N-LCMO and N-CFO nanoparticles and N-MIX

$La_{0.67}Ca_{0.33}MnO_3$ nanoparticles (N-LCMO) were prepared by a polyol sol-gel approach [216]. 4.6 mmol of lanthanum (II) nitrate exahydrate (Fluka analytical, > 99 %), 2.3 mmol of calcium (II) nitrate tetrahydrate (Sigma Aldrich, 99 %) and 6.9 mmol of manganese (II) nitrate tetrahydrate (Sigma Aldrich, > 97 %) were mixed in an equal weight of distilled water in a 250 ml becker. Ethylene glycol (EG, Sigma Aldrich, 99.8 %) was added (1.5 times the volume of water) and the solution was kept at 80°C on a hotplate for 20 minutes, under magnetic stirring. Then, the solution was kept at 150°C until the gel was formed, and finally, the temperature was increased to 300°C to induce the self-combustion. The obtained powder was finally calcinated at 550°C for 2 hours.

Sample N-CFO was prepared by polyol process. It is the sample MF1 in-depth analyzed in **chapters 4** and **5**, whose synthesis is described in **paragraph 4.5.1**.

To prepare N-MIX sample, 80 mg of N-LCMO and 20 mg of N-CFO (effective weight considering also organic coating) were grounded in a mortar with acetone to obtain a fine mixture of the two powders.

6.1.2 Nanocomposites

In order to improve the magnetic coupling between $La_{0.67}Ca_{0.33}MnO_3$ (LCMO) and $CoFe_2O_4$ (CFO) phases, a nanocomposite (NC) was prepared by a seed mediated growth self-combustion method. N-CFO nanoparticles (20% in weight of the final product)

were dispersed in EG (10 ml) to be used as seeds for the growth of LCMO nanoparticles. 4.6 mmol of lanthanum (III) nitrate hexahydrate (Fluka analytical, > 99 %), 2.3 mmol of calcium (II) nitrate tetrahydrate (Sigma Aldrich, 99 %) and 6.9 mmol of manganese (II) nitrate tetrahydrate (Sigma Aldrich, > 97 %) were added to the EG solution (Sigma Aldrich, 99.8 %) with an amount of distilled water equal to their weight. The homogenous dispersion of the CFO seeds and the complete solubilization of the reactants was obtained keeping the solution on a hotplate at 80 °C, under magnetic agitation. Then, the solution was kept at 150°C until a thick and dense gel was formed, tuning the stirring speed in order to obtain a homogenous CFO dispersion. Finally, the temperature was increased to 300 °C and, after few minutes, the gel combustion occurs, producing a very soft and porous grey powder. To ensure the complete crystallization of LCMO, the product was calcinated in an oven at 550 °C for 2 hour.

To perform TMR measurements, both N-MIX and NC were pressed (30 kN) in form of pellet, then they were calcinated at 550 °C for 2 h, in order to obtain a better connectivity among particles and so an improved conductivity trough the LCMO phase. All the structural, morphological and magnetic characterization has been performed on the so treated samples.

6.2 Structure and Morphology

XRD patterns of N-LCMO and N-CFO samples (**figure 6.1**) show reflections of $La_{0.67}Ca_{0.33}MnO_3$ perovskite (PDF card 01-089-6933) and $CoFe_2O_4$ cubic spinel oxide (PDF card 01-079-1744) structures, respectively. No reflections of any other phases are detected. According to TEM analysis, N-LCMO sample is composed of roughly spherical nanoparticles, having size ranging between 10 and 50 nm (**figure 6.2a**). The particles are strongly aggregated and the aggregates have usually a high porosity (**figure 6.2b**). The presence of pores is an expected result of the combustion of organic material and of gas evaporation during the self-combustion process. The introduction of the self-combustion step on the hotplate at 300°C, before proceeding with calcination, allows to conduce it at a relatively low temperature (550°C) (**figure 6.7,** see **paragraph 6.6.1**) and with a quite shorter time (2h) with respect to what usually employed [217–219].

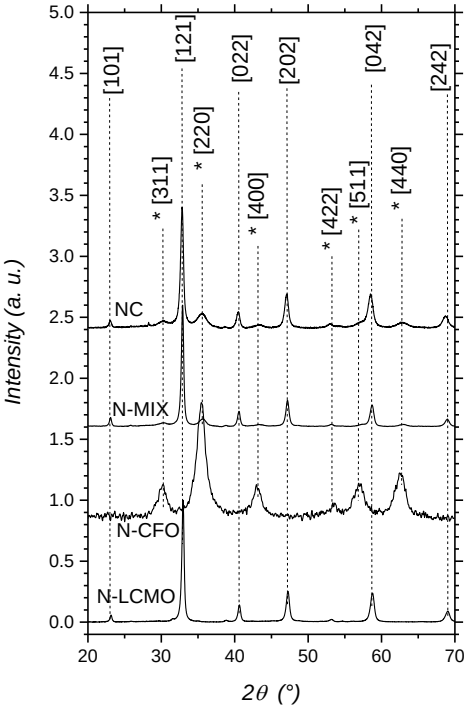

*Figure 6.1: XRD patterns of pure N-LCMO and N-CFO and composites N-MIX and NC. All reflections perfectly match with those of $La_{0.67}Ca_{0.33}MnO_3$ (ICDD card 00-049-0416) and $CoFe_2O_4$ (ICDD card 00-079-1744, reflections marked as *) phases.*

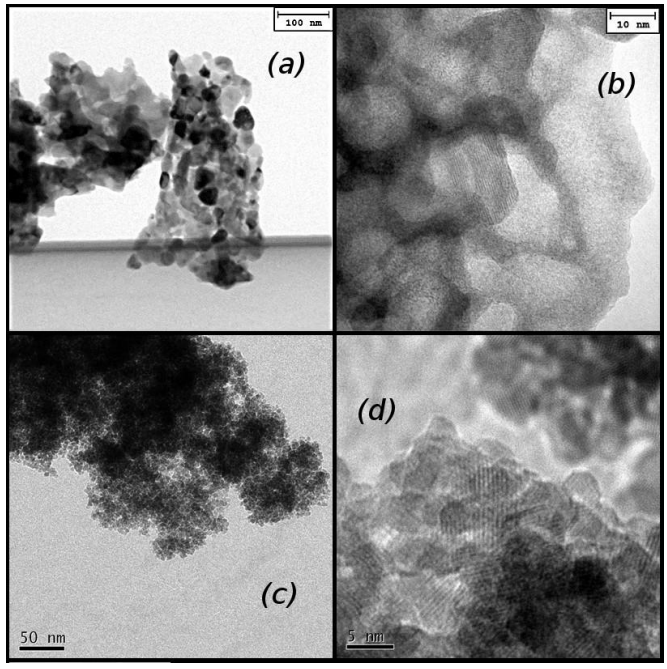

Figure 6.2: TEM images of sample N-LCMO (a and b), N-CFO (c and d) at different magnifications

This relative low temperature has been demonstrated to be enough to obtain high crystalline single-phase perovskite manganite with particles size among the smallest (≈ 28 nm) reported in literature [218,219]. It is worth to mention that the LCMO nominal composition has been confirmed by EDS analysis, within the experimental error (± 5%). N-CFO particles exhibit an average diameter of ≈ 5 nm, with a narrow size distribution and a high degree of crystallinity (**figure 6.2c and 6.2d**). Despite the polyol coating, a strong aggregation among particles is observed.

XRD patterns of both N-MIX and NC (**figure 6.1**) samples show only the main reflections of $La_{0.67}Ca_{0.33}MnO_3$ and $CoFe_2O_4$ crystalline structures and no other phases are detected. The weight fraction of CFO and LCMO, estimated by the Rietveld analysis (**table 6.1**) suggests a ratio of ≈ 30% / 70% and 40% / 60% for N-MIX and NC, respectively. Within the experimental error of ± 5%, almost the same composition can be evaluated for the two composites. In both samples, EDS analysis shows that the stoichiometric formula of the original LCMO and CFO phases have been maintained.

Sample	***<D_{XRD}> CFO***	***<D_{XRD}> LCMO***	***CFO (± 10 %)***	***LCMO (± 10 %)***
N-LCMO	-	28(1) nm	-	100 %
N-CFO	5(1) nm	-	100 %	-
N-MIX	10(1) nm	43(1) nm	30 %	70 %
NC	6(1) nm	32(1) nm	40 %	60 %

Table 6.1: The average coherent crystalline domain size <D_{XRD}> and the CFO / LCMO perceptual evaluated by Rietveld refinement using MAUD. Uncertainties in the last digit are given in parenthesis.

TEM bright field images of the N-MIX sample are shown in **figure 6.3a-d**. The sample consists of two kinds of particles aggregates randomly distributed. In particular, in **figure 6.3c** the circles indicate different LCMO and CFO particles aggregates; the LCMO aggregates are generally larger than the CFO ones, which own an average size around 300 nm. It is important to stress that an intimate mixing between the two phases has never been observed in this sample.

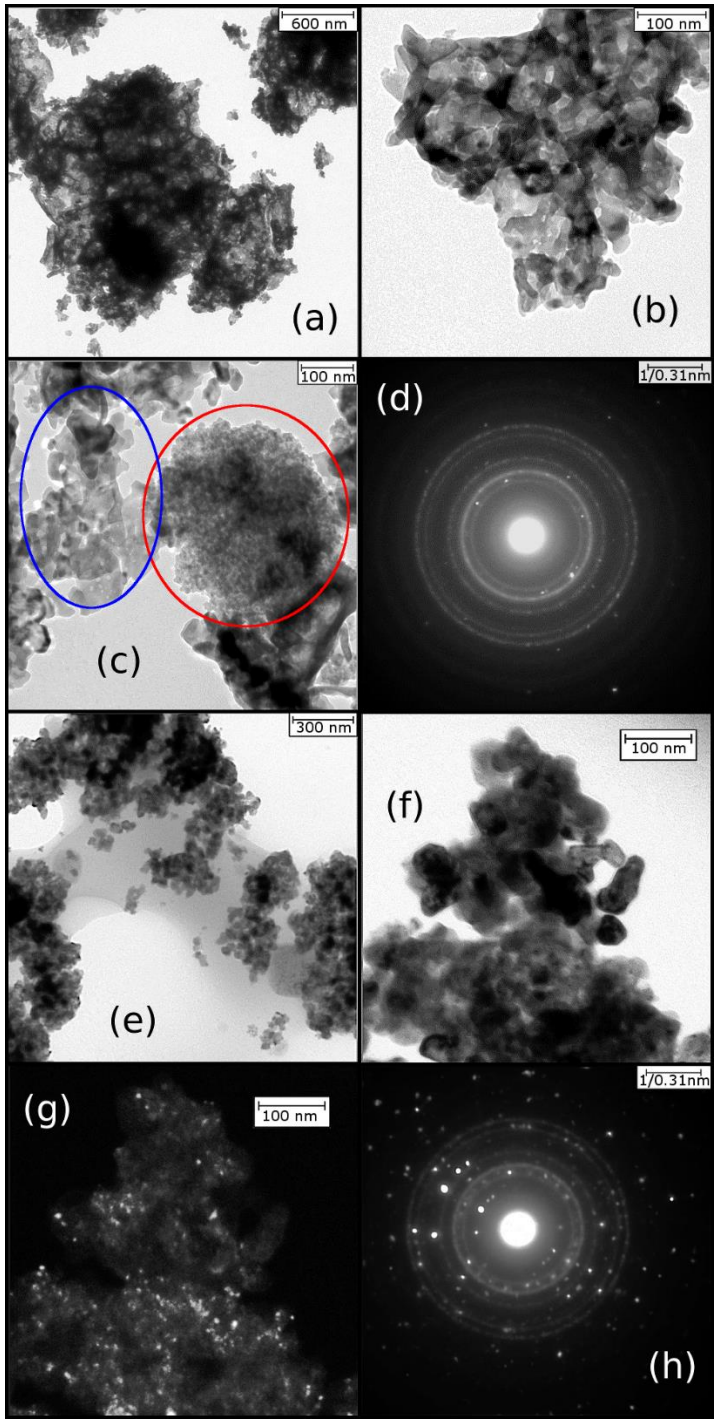

Figure 6.3: TEM images of sample N-MIX are shown in panel (a), (b) and (c), where the two circles identify the CFO and LCMO particles aggregates. Panel (d) reports the electron diffraction image of N-MIX. Panels (e) and (f) show the structure of sample NC; the CFO particles presence can be detected only with a darkfield image as in panel (g). The selected area electron diffraction image (SAED) of NC is reported in panel (h).

On the other hand, the NC sample shows clearly a different morphology: LCMO particles are generally less aggregated, and there is no trace of CFO particles at a first sight (**figure 6.3e and f**). Their presence is only revealed by TEM dark field images. In particular, **figure 6.3h** shows a selected area electron diffraction (SAED) pattern corresponding to the sample area imaged in **figure 6.3f**. It consist of intense diffraction spots, randomly distributed, and weak diffraction rings. Analyzing the interplanar distances obtained by SAED, it is possible to associate the origin of the intense diffraction spots to the presence of quite large LCMO crystals, and the diffraction rings to the presence of small CFO crystals oriented in all the directions. **Figure 6.3g** is the dark field image of **figure 6.3f**, obtained using part of the first diffraction ring. In this way, the CFO particles, responsible for that part of the diffraction ring, appear bright in the image. This picture clearly shows as the CFO particles do not form aggregates and are homogeneously distributed in the LCMO phase. The size of the cobalt ferrite particles is in perfect agreement with that measured for the CFO sample; instead, LCMO particles appear, in some cases, larger than those in N-LCMO. Concerning the particles size, TEM analyzes confirm XRD results. It is worth to note that sample N-MIX presents larger mean crystallite size for both LCMO and CFO phases compared to those of the original untreated compounds (**table 6.1**). On the other hand, sample NC shows LCMO particles only slightly larger than the untreated ones while the CFO particles keep their original size within the experimental error. This suggests that in NC sample the good dispersion of CFO particles inside the LCMO matrix protects them, avoiding their growth during the calcination of the pellet.

6.3 Magnetic properties

The ZFC-FC of N-MIX sample, (**figure 6.4c**) shows the FM/PM transition with the magnetization which falls to zero in both curves above ≈ 260 K, where the T_C for LCMO of this composition is expected (**figure 6.4a**) [220,221]. No evidence of superparamagnetic transition related to CFO nanoparticles is identified, even if its presence has been clearly demonstrated by XRD and the results in M(H) curves. Considering the peak produced by the blocking temperature of pure CFO (**figure 6.4b**), it is reasonable to think that its contribution in ZFC-FC curves, should produce a signal that is hidden by that much stronger of LCMO, which represents ≈ 80% of the sample. To enforce this hypothesis, an artificial curve has been created by summing the contribution of CFO and LCMO curves with a weight ratio of 20 and 80 %, respectively (**figure 6.9** in paragraph **6.6 supporting information**). As expected, this curve exhibited

the same trend of that of N-MIX. Sample NC presents a ZFC curve with two clear peaks (**figure 6.4d**). The peak at ≈ 240 K reproduces exactly that of CFO phase (**figure 6.4b**). On the other hand, the peak around ≈ 110 K could be related to the presence of the nanostructured LCMO phase. This hypothesis is confirmed comparing the ZFC curve with that of a further composite, labelled as NC2, prepared with the same procedure of NC, but employing only 5% in weight of CFO phase. Its ZFC curve exhibits the dominant contribution of LCMO (**figure 6.4d**); the FM/PM transition is shifted toward lower temperature, with a drop in magnetization value, which induces a peak exactly around ≈ 110 K. This landscape can be confirmed and better described the TRM measurements [127] in **6.6.4** (see **appendix 8.2.1** for detailed description of the method).

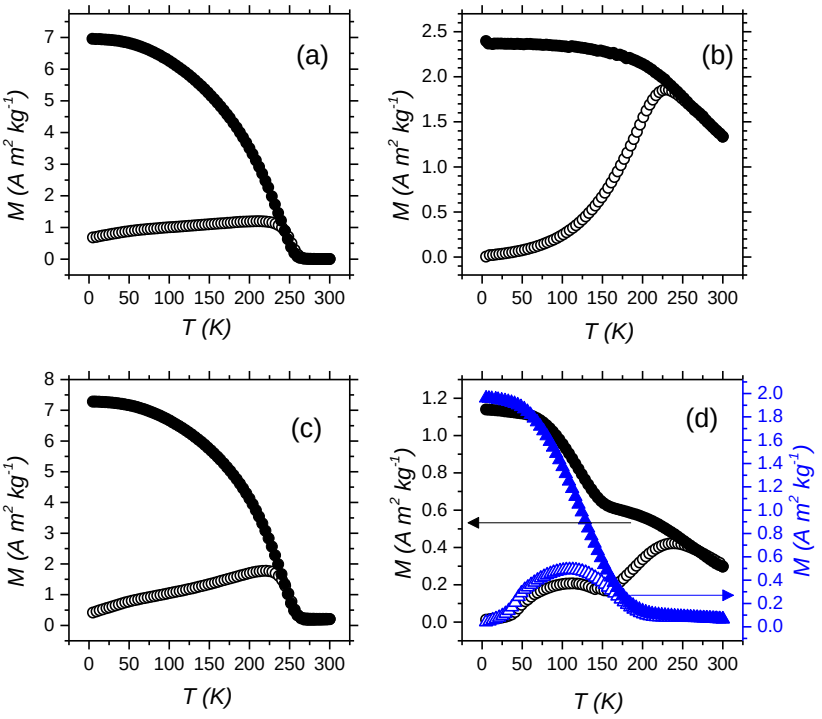

Figure 6.4: The ZFC and FC curves (empty and full symbols, respectively), for sample N-LCMO (a), N-CFO (b) and N-MIX (c) are shown. Panel (d) reports the ZFC-FC curves of sample NC (empty and full circles) and NC2 (empty and full triangles).

6.3.1 **Reversal mechanism of the magnetization**

The field dependence of magnetization recorded at 5 K shows a clearly different behavior for N-MIX and NC samples (**figure 6.5a**). The loop shape of the N-MIX sample is typical of a not coupled system, being close to a simple superposition of the hysteresis loops of pure CFO and LCMO phases (**figure 6.5b** and **c**). Indeed the coercive field $\mu_0 H_C$ reproduces the same value of N-LCMO, while the saturation field $\mu_0 H_{SAT}$ is quite close to that of the pure CFO component (**figure 6.5c** and **table 6.2**). Both LCMO and CFO components are clearly detectable, but they appear acting individually, without a significant coupling. On the other hand, the M(H) curve for the NC sample (**figure 6.5a**) exhibits a nearly single phase behavior, indicating a strong coupling between LCMO and CFO phases. A closer inspection indicates the hysteresis loop is slightly constricted. This suggests a magnetic behavior that is placed in the transition region between that of a rigid magnet, where the soft and hard phases reverse coherently, and that of an exchange-spring system, characterized by an incoherent reversal mode, where the soft phase reverses first and support the switching of the hard component [30].

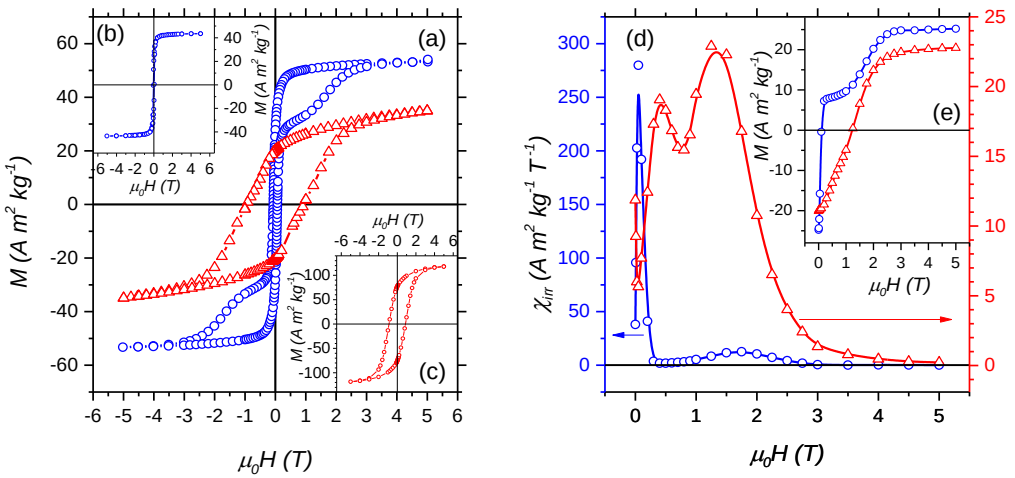

Figure 6.5: M Vs H curve of N-MIX (circles) and NC (triangles) are reported in panel (a). The curves for N-LCMO (b) and N-CFO (c) single phases are reported for comparison. For N-MIX (circles) and NC (triangles) the switching field distributions are reported in panel (d), while the original DCD curves are reported in inset (e).

It should be underlined that the saturation magnetization values (**table 6.2**) of both samples are lower with respect the bulk LCMO (≈ 97 A m^2 kg^{-1}), but the same results have been previously reported [222–224] supposing a magnetically disordered surface as the origin of reduction in saturation magnetization in nanoparticles.

A more detailed investigation of the magnetization reversal has been performed analyzing the field dependence of the remanent magnetization measured by IRM and DCD protocols (**table 6.2** and **figure 6.11, paragraph 6.6.5**, for pure phases). The SFD (see **appendix 8.2.3** for detailed description) of sample N-MIX (**figure 6.5d**) presents a strong contribution centered at low field (≈ 0.05 T) as for the pure LCMO, and only a very weak signal due to high field contribution (≈ 1.73 T) of CFO phase, even at higher field than that of the pure one. It is a matter of fact that sample N-MIX shows the individual contribution of these two phases without a clear coupling. On the other hand, sample NC presents a different picture (**figure 6.5d**): both the contribution of the pure phases are visible but the two average switching fields are shifted closer with respect the original pure phases, as results of a strong coupling between them.

Sample	***M_S ($A\ m^2\ kg^{-1}$)***	***$\mu_0 H_C$ (T)***	***$\mu_0 H_{SAT}$ (T)***	***$dM/d\ \mu_0 H$ at 5T ($A\ m^2\ kg^{-1}\ T^{-1}$)***	***$\mu_0 H_C^{SFD}$ (T)***	***$\mu_0 H_{rev}$ (T)***
N-LCMO	44(2)	0.050(1)	0.3(1)	0.05(1)	0.05(1)	0.07(1)
N-CFO	107(6)	0.83(1)	3.2(4)	1.55(7)	1.10(1)	0.85(5)
N-MIX	54(3)	0.067(1)	3.4(6)	0.26(1)	0.05(2) 1.71(2)	0.07(1) 1.83(5)
NC	44(3)	0.94(1)	3.1(1)	1.5(2)	0.42(5) 0.31(5)	1.25(5)

Table 6.2: Saturation magnetization (M_S), coercive ($\mu_0 H_C$) and saturation field ($\mu_0 H_{SAT}$), susceptibility at 5 T ($dM/d\mu_0 H$), average switching field ($\mu_0 H_C^{SFD}$), and reversal field ($\mu_0 H_{rev}$) measured at 5 K. Uncertainties in the last digit are given in parenthesis.

The magnetic field dependence of the IRM and DCD magnetization is compared in so called *ΔM-plots* [225] in order to study the nature of magnetic interactions (**table 6.2**). Both N-MIX and NC show plots with negative deviations of the curves (**figure 6.12c** and

d), which reveal the prevalence of dipolar interactions [161,226,227]. Furthermore, sample N-MIX exhibits two different dips in the *ΔM* plots, indicating two mechanism of interaction, which are compatible with the independent interactions of LCMO and CFO particles. This is in agreement with the morphology evidenced in the TEM images, where LCMO and CFO particles are shown to form distinct aggregates, thus inducing interactions manly among particles of the same phase. In a stark contrast, sample NC shows a single broad signal centered at ≈ 1.25 T, thus confirming an almost single-phase interaction mechanism between LCMO and CFO, which is strongly related to the morphological structure of this sample. The coupling between CFO and LCMO particles is strong enough to shift the reversal process of the LCMO toward higher fields, far above its original coercive field. It allows an almost single magnetization switching, mostly related to the high field process of the CFO component, remarking the same behavior shown in M(H) curve.

6.4 Magnetoresistance

Coherently with the differences in morpho-structural and magnetic properties, the two nanocomposites exhibit a well distinct electrical behavior. R Vs T curve of sample N-MIX (**figure 6.6a**) shows a peak at a temperature T_R (≈ 123 K) lower than the T_C (≈ 260 K) of LCMO component, when the metal-insulator transition occurs. This behavior is typical for systems in which the resistivity is dominated by grain boundaries [228] and/or surface effects [229]. The measured magneto-resistance (MR) effect (**figure 6.6b**) shows a continuous increment reducing temperature until ≈ 120 K, when all material undergoes the FM-metallic transition. Then it remains almost constant down to ≈ 50 K; on further lowering of temperature an upturn is observed in resistance signifying Coulomb blockade phenomenon that is seen in metallic nanoparticles [230]. The low energy of the charge carriers at a so low temperature cannot contrast the coulomb repulsion and hence reduces the probability of tunneling [231], leading to a new insulating regime. Finally, the application of an external field induces a common spin orientation reducing the electronic scattering [207], as result the overall resistivity is reduced (**figure 6.6a**).

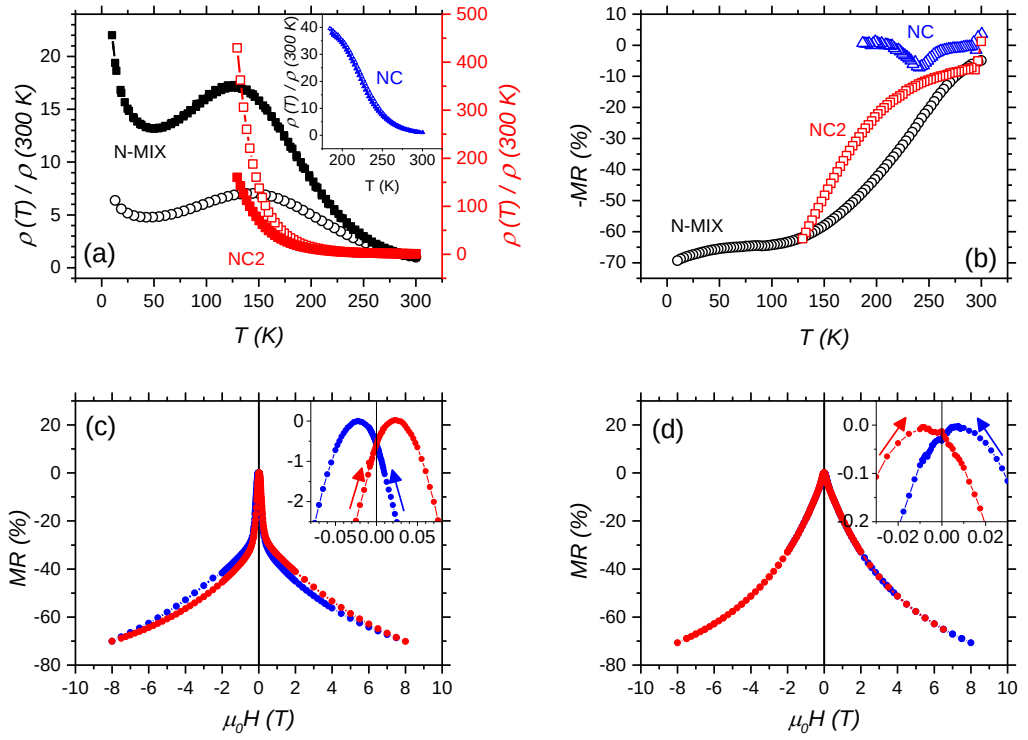

Figure 6.6: The temperature dependence of the resistance is reported in panel (a) for sample N-MIX (circles), NC (triangles in inset) and NC2 (squares) without (empty symbols) and with an applied magnetic field of 5 T (full symbols). It is important to note that for sample NC the two curves are almost superimposed. Panel (b) reports the temperature dependence of the magnetoresistance for N-MIX (circles), NC (triangles) and NC2 (squares). For sample N-MIX, the magneto-resistance measured at 5 K and 150 K are reported in panel (c) and (d), respectively. A magnification at low field is reported in the respective insets, with arrows indicating the direction of field sweeping.

On the other hand, sample NC shows high resistance values with a strong increment on reducing the temperature (**figure 6.6a**), reaching an unmeasurable high value below 180 K. Such strong resistivity can be related to the specific structure of the sample. The CFO component in sample N-MIX does not increase the overall resistivity, since the CFO agglomerates do not represent a significant obstacle for the electric flow within the LCMO phase. On the other hand, the core/shell-like structure of NC owns a very fine and homogenous distribution of the insulating CFO, which promotes an insulating character for the composite [54]. Furthermore, no magneto-resistance effect is visible and the two curves with and without applied field are almost perfectly superimposed.

By the way, one should note that cooling down the sample, the MR curve exhibits a small negative peak (- 8 %) at ≈ 240 K, which could be related to the onset of the FM ordering. Analyzing the R Vs T curve of NC2 sample, an intermediate behavior is observed (**figure 6.6a** and **b**). A magnetoresistance effect is clearly visible but still the absolute value of resistance can be measured only down to ≈ 130 K. This suggests that the conductivity of such core/shell composites can be tuned, e.g., modifying the CFO/LCMO ratio and/or particles size.

The MR behavior of N-MIX sample was further investigated by collecting R Vs H loops at constant temperatures. As shown in **figure 6.6c** the sample at 5 K shows a conventional behavior; sweeping the field from + 8 to - 8 T, a peak in MR is visible with a negative applied field $\mu_0 H_C^{MR}$, while sweeping in the opposite direction, the peaks appears with a positive $\mu_0 H_C^{MR}$. This is in contradiction to the inversion of R(H) loops observed in macroscopic composite of LSMO and CFO [215] . However, measuring the R(H) loops at higher temperatures leads to a decrease in $\mu_0 H_C^{MR}$ and interestingly the R(H) loop is inversed for temperature above 100 K. The MR peak occurs before the switching of the direction of the applied field, reaching a maximum opposite value around 150 K (**figure 6.6d**). Such dipolar biasing effect [215] occurs at a low applied field, when the residual magnetization of CFO produces a stronger local dipolar field that leads to the antiparallel coupling of LCMO, which switches its magnetization, before the inversion of the external field H_{ext}, but the dipolar field effect disappears under 100 K.

6.5 Conclusions

We have reported the novel design of nanocomposites of transition metal oxides with tailored magnetic and electrical properties. We have illustrated the relationship between synthesis methods and morphology-physical properties using the well-known $La_{0.67}Ca_{0.33}MnO_3$ (LCMO) and $CoFe_2O_4$ (CFO) oxides as model systems. The properties of a mechanical mixture of LCMO and CFO phases were compared with those of a nanocomposite prepared by a new synthetic approach. Structural and morphological characterization clearly showed a strong aggregation of CFO nanoparticles in N-MIX sample, hindering an intimate contact between the two magnetic phases. On the other hand, NC sample showed a very homogeneous morphology, with CFO nanoparticles well dispersed in the LCMO matrix. Consequently, a strong magnetic coupling has been shown by the NC sample, with magnetic behavior that can be considered in the

transition region between that of a rigid magnet and that of an exchange-spring system. On the other hand, a very poor coupling has been evidenced for the N-MIX, with independent reversal mechanism for LCMO and CFO phases. Similarly, both samples showed clearly different electrical behavior. While the NC composite is highly insulating, magnetoresistance and dipolar biasing effects are observed in the N-MIX sample.

$La_{0.67}Ca_{0.33}MnO_3$-$CoFe_2O_4$ samples have been used as a model system to illustrate this novel approach, and they represent a first attempt to produce such new nanocomposites of strongly correlated materials. Further improvement can be achieved by tuning the relative amount of CFO and its particles size. As well as creating an inverse core-shell structure, where LCMO represents the core surrounded by a thin CFO layer.

6.6 Supporting information

6.6.1 Calcination process

A calcination process was employed in order to produce the complete crystallization of the manganite phase after the sol-gel synthesis. Performing several attempts at different temperature, the optimal condition has been found at 550 °C (**figure 6.7**), reaching the complete crystallization as the lowest possible temperature in order to retain the smallest particles size.

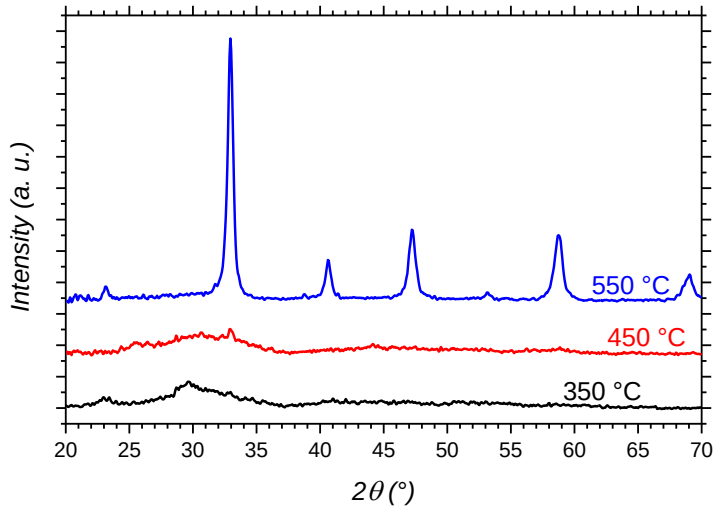

Figure 6.7: XRD pattern of $La_{0.67}Ca_{0.33}MnO_3$ phase calcinated at several temperatures.

6.6.2 **Cobalt doping effect**

In order to clarify the eventual diffusion of cobalt from the CFO to the LCMO phase in NC sample, the $La_{0.67}Ca_{0.33}MnO_3$ (ICSD 155408) and the $La_{0.67}Ca_{0.33}Mn_{0.9}Co_{0.1}O_3$ (ICSD 165817) patterns have been compared with the experimental one. As shown in the pattern magnification in **figure 6.8**, the presence of Co as dopant should produce a quite clear shift in the experimental data. If the Rietveld refinement is conduced considering the two LCMO phases, the best fit corresponds to 1% in weight of the cobalt doped phase, under what can be considered the experimental error on this measurement (estimated around 5 %). Furthermore, if the fitting is forced using only the Co doped phase, but leaving the Co and Mn contents as free parameter, the best fit evaluates the Mn content as 0.9999 and the Co as 0.0001, strongly supporting its absence.

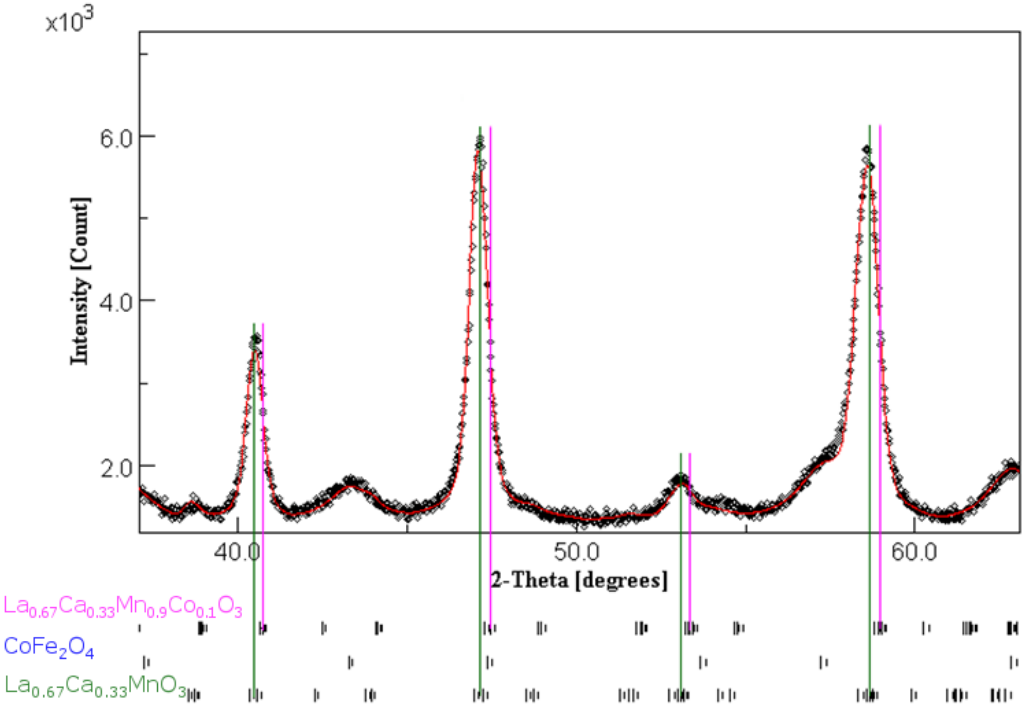

Figure 6.8: Magnification of XRD pattern of NC sample in the range 35-65° (2-Theta).

6.6.3 **Simulated ZFC-FC curves for N-MIX sample**

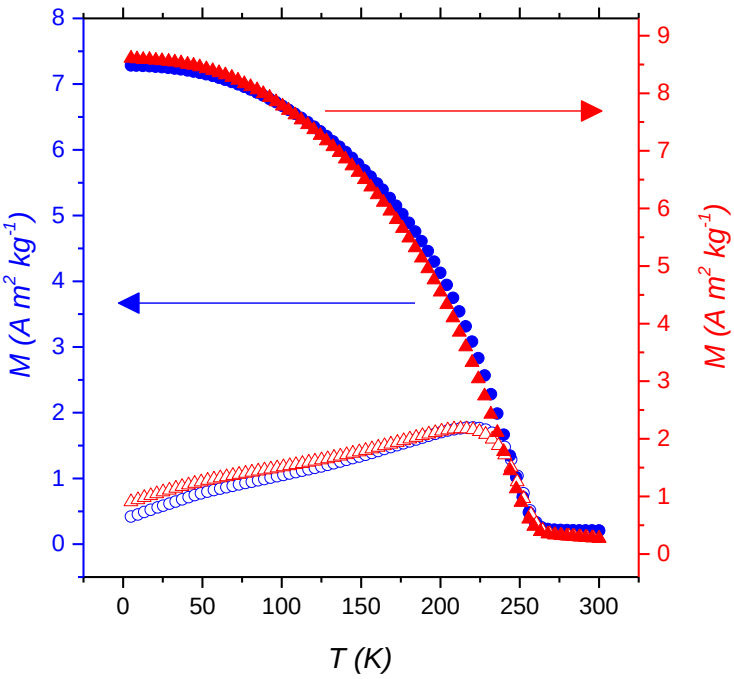

Figure 6.9: The experimental ZFC-FC curve (empty and full circles, respectively) and the artificial one (empty and full triangles, respectively) are shown. The two curves exhibit similar trends, with no clear evidence of the CFO contribution.

6.6.4 TRM and derivative curves analysis

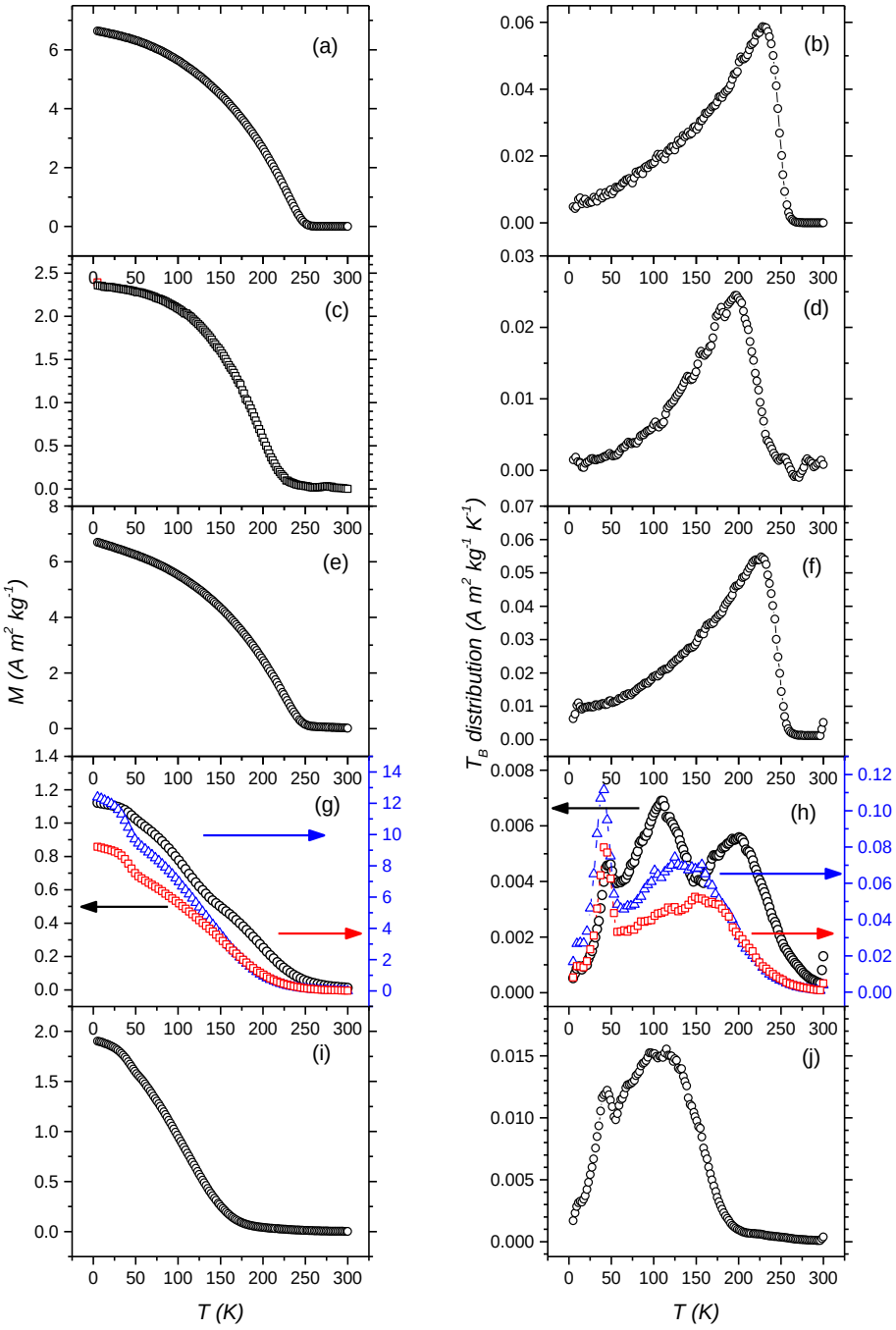

Figure 6.10: The TRM curves and their derivatives are shown for N- LCMO (a and b), N-CFO (c and d), N-MIX (e and f), NC (g and h), and NC2 (i and j). For NC, the curves measured with an applied field of 2.5 mT, 50 mT and 100 mT are represented as circles, squares and triangles, respectively.

d(TRM)/dT curve (**appendix 8.2.1** for a detailed description of the method) of NC sample measured at 2.5 mT (circles in **figure 6.10h)** shows a peak at ≈ 190 K perfectly compatible with the SPM behavior of pure CFO (**figure 6.10d**). Furthermore, two signals, centered at ≈ 111 K and ≈ 50 K are identified. In order to better analyze the nature of these two signals, the TRM and derivative curves have been measured at different fields (**figure 6.10g** and **h**). The peak at highest temperature shows a field dependent behavior, in agreement with the SPM blocking of CFO phase. On the other hand, the peak at ≈ 111 K does not show such field dependence, confirming that it can be related to the drop of the magnetization due to the LCMO FM / PM transition, which occurs at a temperature lower than expected (≈ 260 K). Again, this interpretation can be confirmed by the TRM of NC2 sample reported in **figure 6.10i** and **j**, where a T_C ≈ 200 K can be estimated. Such T_C shift could be ascribed to cobalt or iron doping in LCMO structure, owing to the thermal treatment on the composite. Nevertheless, carefully analyzing the XRD pattern, no trace of such cobalt inclusion has been evidenced (**figure 6.8**). On the nanoscale, a disordered magnetic structure arises at particles surface due to broken lattice symmetry and possible defects. Such defects induce larger Mn-O distance and a corresponding smaller Mn-O-Mn angle, inducing an effect on the local T_C temperature. Reducing particles size, the surface to volume ratio increases and the surface disorder has a strong influence on the T_C of the whole particle, in particular under 40 nm, as experimentally observed by Markovic et al. [233]. Conflicting experimental results have been reported in literature for the particle size dependence of T_C in manganites, probably mainly due to slightly different oxygen content and preparation procedure, which has a strong influence on particles surface. Anyway, Montecarlo simulations have shown that the reduced ionic coordination at particles surface lowers the T_C for NPs [234], as confirmed by a systematic study on the effect of particles size on $La_{0.6}Pb_{0.4}MnO_3$ by Zhang et al. [235]. The monodomain critical radius for manganites has been predicted around 40 nm [236] and a SPM blocking or spin-glass like freezing has been suggested by several authors [219,237,238]. Anyway Markovich et al. [233] have found similar T_C size dependence, observing that the ZFC curve peak has an AC frequency dependence, typical of interacting SPM particles, only for size around 10 nm, enforcing the hypothesis of a simple phase transition origin of the peak.

Finally, in d(TRM)/dT curve of NC, a small peak appears at ≈ 50 K. Several authors have claimed to observe a spin-glass-like behavior in LCMO around ≈ 40-50 K [239–241], but in most of the cases this can be assimilated to the paramagnetic-ferrimagnetic (PM-

FiM) transition of Mn_3O_4 impurities ($T_N \approx 43$ K) [242,243]. This can give a significant magnetic contribution even with an amount that is smaller than the XRD detection limit [244]. A second possible origin for such peak can be the freezing of a disordered surface shell on a ordered FM core, as reported by Zhu et al. for LSMO particles under 50 nm [245]. However, no field dependence of this peak is observed by measuring ZFC-FC-TRM in different fields, instead, an increment of the magnetization compatible with a small fraction of impurities is evident.

6.6.5 IRM, DCD and ΔM-plots

For a more complete analysis of the two composites, a comparison with the pure LCMO and CFO phases has been carried out. For the sake of clarity, the detailed IRM e DCD curves with the respective derivatives are measured for each sample and shown in **figure 6.11**, while the obtained ΔM plots are compared in **figure 6.12** (for a detailed description see **appendix 8.2.3**).

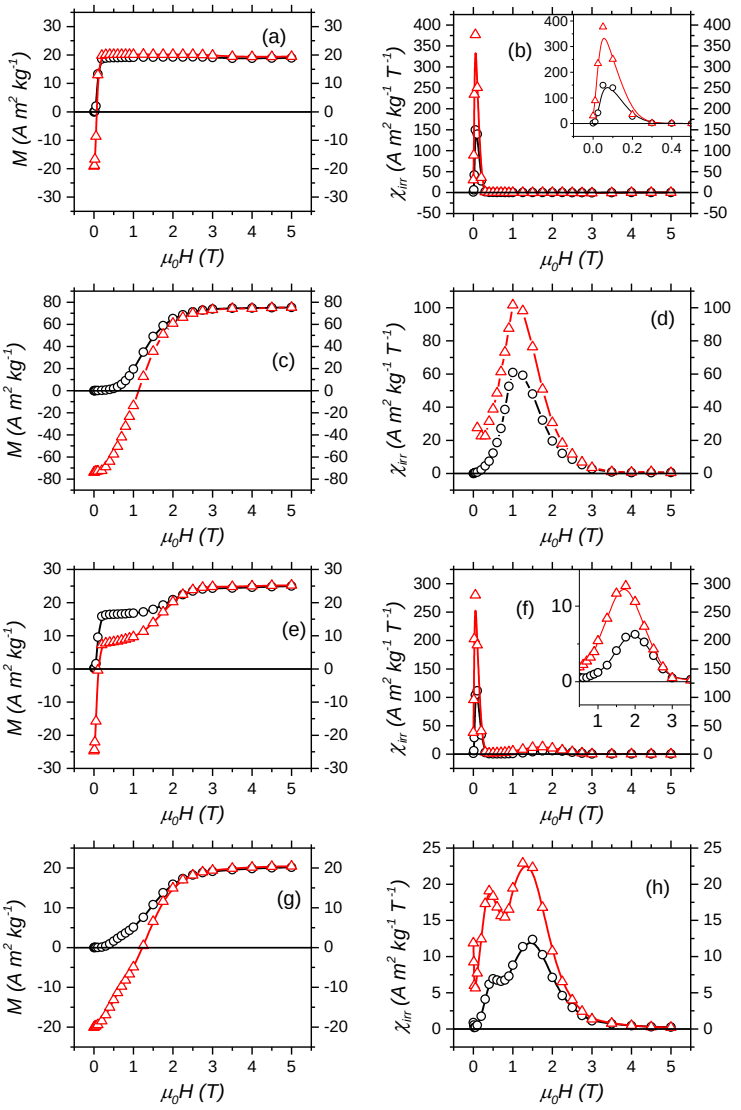

Figure 6.11: IRM (circles) and DCD (triangles) curves of samples N-LCMO (a), N-CFO (c), N-MIX (e), and NC (g). The corresponding derivatives curves $\chi_{irr} = dM_{IRM}/d\mu_0 H$ (circles) and $\chi_{irr} = dM_{DCD}/d\mu_0 H$ (triangles) are reported in panels b, d, f, and h for samples N-LCMO, N-CFO, N-MIX, and NC, respectively, with data magnification reported in insets.

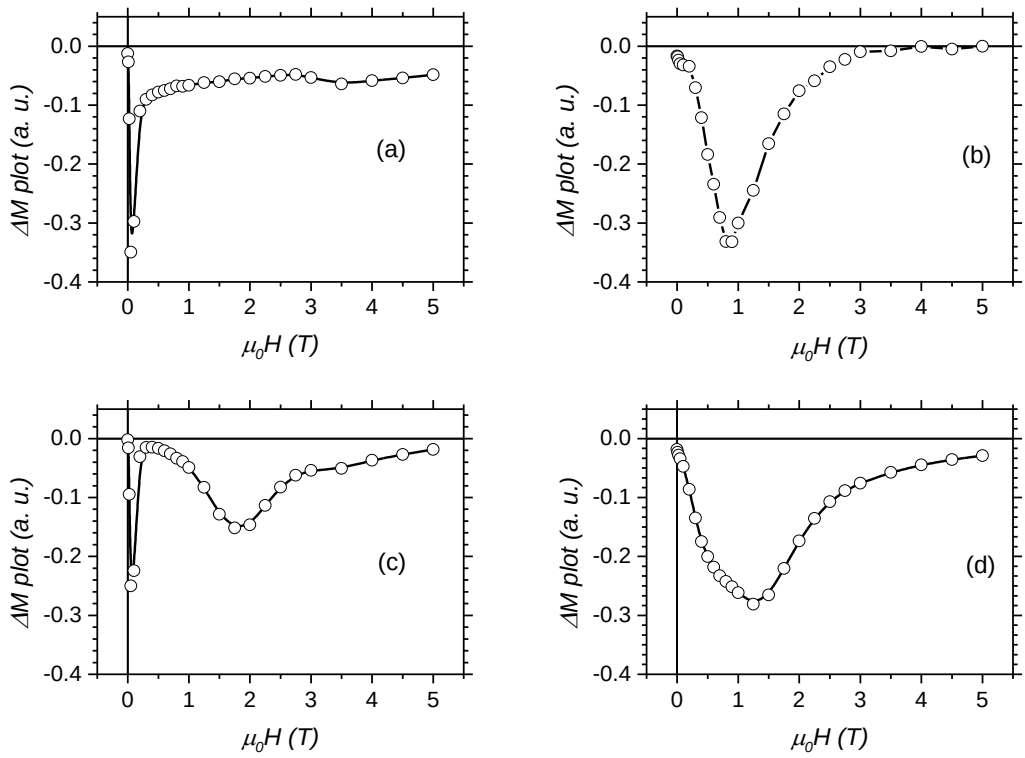

Figure 6.12: ΔM plots of samples N-LCMO (a), N- CFO (b), N-MIX (c), and NC (d).

Chapter 7
Summary and perspectives

The magnetic anisotropy is a key parameter to tune the magnetic properties of nanoparticles. In this view, the main work covered by this thesis has been to explore several ways to tune the magnetic anisotropy in nanoparticles based materials.

It has been observed the effect of particles volume on the MAE, with a particular attention devoted to the importance of the size distribution. The aspect maps have been proposed as a new tool to analyze particles morphology; their potentiality has been practically demonstrated in the study and tuning of the HTD synthesis of nanoparticles. As result, narrower size and shape distributions have been obained, with a clear improvement in the switching field distribution of the system.

Analyzing the properties of particles smaller than 10 nm, it has been shown the strong contribution of the surface anisotropy at this size scale. The origin of the surface anisotropy has been reduced to the symmetry breaking at the nanoparticle's surface, inducing changes in the topology of the superficial magnetic moments and consequently in exchange integrals (through superexchange angles and/or distances between moments). As example of organic surfactant, the wide employed oleic acid coating has been studied, demonstrating its role in providing a more ordered environment around surface spins, thus reducing the surface anisotropy. Anyway, with particles smaller than 5 nm such effect is limited, becoming the surface component of anisotropy comparable to the bulk magnetocrystalline contribution. The oleic acid has been compared to the diethylene glycol, observing as the second reduces the local surface anisotropy better than the first does, showing in addition a much larger saturation magnetization. The analysis of the effect of different coatings is still an open topic, which deserves a particular attention, representing a way to modify the magnetic properties.

In this context, a further step will be to analyze particles with different shape, e.g., spheres, cubes, octapods, in order to study the effect of faces and edges in inducing surface spin ordering and its effect on the local anisotropy.

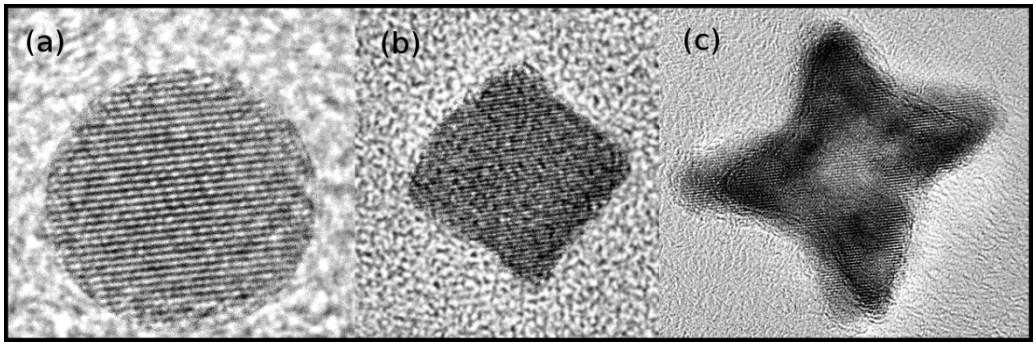

Figure 7.1: Examples of ferrite nanoparticles with spherical (a) and cubic (b) shape. Furthermore, an example of star-like shape (octapod) is shown in panel (c). Synthesis and characterization have been performed at NTNU University in collaboration with Doc. Gurvinder Singh.

A new and interesting development in this field is represented by hollow nanoparticles (HNPs), in which the surface component is maximized at the expenses of particles core (**figure 7.2**). Surface effects are more pronounced due to the availability of extra surface layer (inner layer) in addition to the interface between randomly oriented grains (outer layer), which contributes to enhance the total surface area.

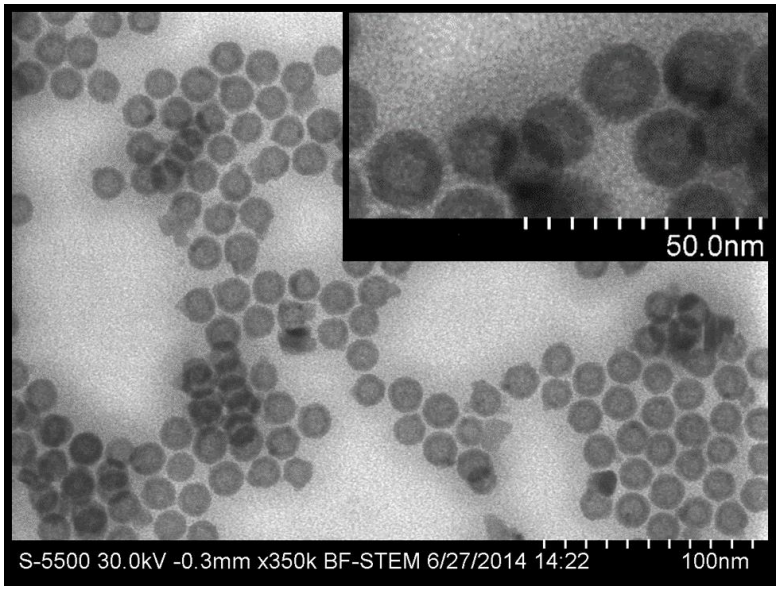

Figure 7.2: Hollow nanoparticles.

Recent studies have been accomplished in order to investigate the effect of such inner and outer spin disorder on the surface anisotropy and its relation with exchange bias [246]. Thus, the large particle anisotropy obtained for hollow nanoparticles can be attributed to the enhanced contribution from both “surface” and “finite size effects” [247]. In addition HNPs are promising materials for several applications, e.g., they can be used in biomedicine, in particular in target drug delivery because of its magnetic properties and hollow structure [12].

Using ferrite nanoparticles as a model system, it has been studied the effect of the chemical composition in tuning their magnetocrystalline anisotropy. Modulating the content of nickel in place of cobalt, it was possible to tune the effective MAE in a range of two order of magnitude. In addition, the same samples have showed an interacting regime in which has been evidenced the competitive role of single particle anisotropy and interparticle interactions. These results have been explained in the framework of a modified random anisotropy model. The conclusion are of interest, not only from a fundamental point of view, but also for their potentialities to design material for specific applications. As demonstrated by the results of the modified RAM study, it is possible to develop systems in which the thermal switching and the field switching of the magnetization can be modified separately, opening new interesting perspectives for technological applications.

Nowadays, several advanced magnetic and magnetoelectronic devices rely on the interface exchange coupling (EC) between different magnetic phases (e.g., magneto-recording, magnetoresistive random access memories, spring magnets, magnetic tunnel junctions, microwave absorption, and permanent magnets), where EC nanocomposites of hard-soft magnetic phases can be advantageous over single magnetic nanoparticles [30,82,248–250]. The great challenge for optimizing the performances of such devices is to control the interface exchange coupling strength through a proper engineering of the nanostructure. This offers a new degree of freedom in order to tune the coercivity, which represents the technological key parameter for any application of magnetic materials. Actually, the exchange interaction across the FM-FiM / AFM interface gives rise to an additional exchange anisotropy, which affects the magnetization reversal process of the whole system, producing significant changes in the coercivity [29,30,251]. Moreover, the increasing demand for miniaturization and enhanced thermal switching stability of magnetic devices stimulates a growing interest on the study of the magnetic properties of FM/AFM

exchange coupled systems, on a nanometric scale in at least one of their dimensions [47]. However, the effects of the size-confinement on the FM/AFM exchange coupling mechanism are still unclear and further fundamental studies are needed in the perspective of future technological applications.

Nanostructured composites, as those proposed in **chapter 6**, represent the starting point to develop exchange coupled FiM/AFM systems. The analysis of different nanostructures has shown that the mechanical mixing induces a small coupling between the two magnetic phases, but it has produced an interesting dipolar bias effect important for the magnetotransport properties of the sample. On the other hand, the core/shell-like approach has demonstrated to represent an optimal way to maximize interface contact between the two phases in order to produce a strong exchange coupling. A further development of exchange coupled nanostructured compounds will be the deposition of FiM particles onto an AFM substrate, (e.g., $La_{0.33}Ca_{0.66}MnO_3$).

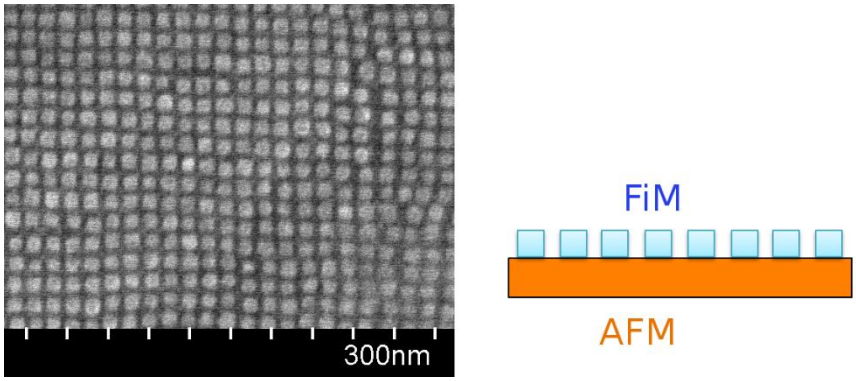

Figure 7.3: TEM image and graphical sketch of cubic nanoparticles of cobalt ferrite deposited onto a LCMO AFM film. The design of these materials has been performed in collaboration with Doc. Gurvinder Singh (NTNU University).

Chapter 8
Appendix

8.1 Perovskites

Perovskites are ABO_3 structured compounds where *A* represents a large radius cation and *B* a small radius one. *A* cations describe the corners of a cubic cell, an oxygen ion is sited in the center of each cubic face and a *B* cation is sited in the center of such cell. Thus, the small *B* cation owns an octahedral coordination with 6 oxygen ions, while the large *A* cation is sited in the center of a dodecahedron, coordinated by 12 oxygen ions.

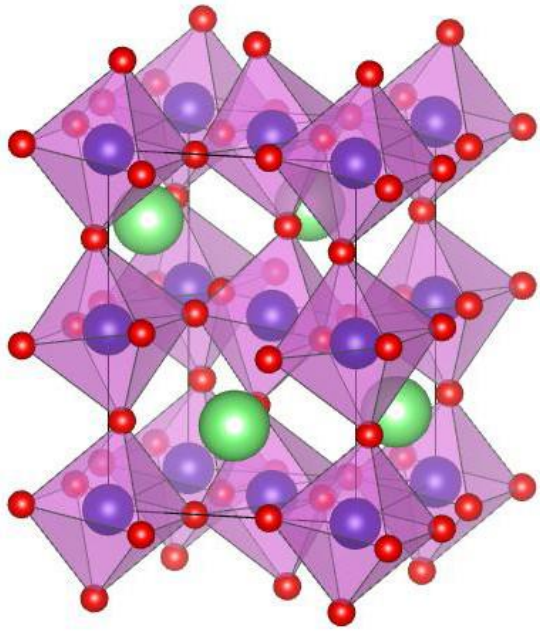

Figure 8.1: $R_{1-x}A_xMnO_3$ structure. The A-sites are represented by the large cations (largest spheres), while Mn in B-sites are described as the spheres inside the octahedra. Oxygen ions are represented as small spheres at the vertexes of the octahedra.

8.1.1 Hole-doped rare-earth manganites

Perovskites manganites own a perovskite structure with manganese representing the *B* cation. Hole-doped manganese oxides has attracted a new attention after the discovered of their colossal magnetoresistance (CMR) effect [207]. They own trivalent rare-earth elements (R) and a divalent alkaline-earth in *A* sites in a $R_{1-x}A_xMnO_3$ structure. The mixed valence of cations in *A* sites produce a mixed valence Mn^{3+} / Mn^{4+} in *B* sites. In the ideally perovskite structure, *A* cations describe a cubic cell, if the ions size produces a tolerance factor t = 1:

$$t = \frac{r_A + r_O}{\sqrt{2}(r_{Mn} + r_O)} \qquad 8.1$$

where r_A, r_O and r_{Mn} are the average *A* ions size, the oxygen radius and the manganese Mn^{3+} / Mn^{4+} average radius. Slightly differences from the ideal ions size induce lower-symmetry distortions versions where the coordination numbers of *A* and *B* cations can be reduced. The orthorhombic and tetragonal phases are most common non-cubic variants. The nature and amount of the R_{1-X} doping represent the main effects on the magnetic and electric properties of such compounds. In particular, compositions with x ≈ 0.3, usually own a curie temperature T_C for the paramagnetic-ferromagnetic transition, which also correspond to an insulator-metal transition.

The octahedral coordinated Mn ions own a splitting of 3*d* electrons in a lower energy triple degenerate state t_{2g} and a higher energy double degenerate e_g one. Mn^{3+} and Mn^{4+} ions own $t_{2g}^3\ e_g^1$ and $t_{2g}^3\ e_g^0$ configuration, respectively. A Jahn-Teller distortion occurs for Mn^{3+} octahedron, further splitting the energy levels (orbital ordering, **figure 8.2** [252]). A strong Hund coupling emerges inducing parallel arrangement among e_g^1 and t_{2g}^3, allowing thus for an easy hoping trough the Mn-O-Mn bond. It occurs in a simultaneous double hopping for $Mn^{3+} \rightarrow O^{2-}$ and $O^{2-} \rightarrow Mn^{4+}$, which is maximized if the spins of the two ions own a parallel alignment. These double exchange [253] interactions are both responsible of the magnetic order and the conductivity of such oxides.

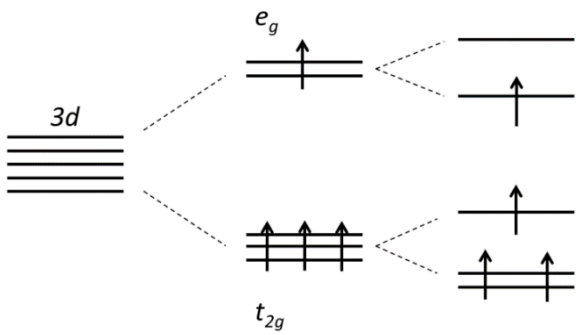

Figure 8.2: Energy level diagram of Mn^{3+} 3d orbitals

$La_{1-x}Ca_xMnO_3$ is one of the most studied hole-doped manganites with CMR properties. The different doping produces a rich phase diagrams with different effect of orbital ordering resulting in several possible combinations of magnetic and electric behavior.

8.2 Magnetic measurements protocols

The magneto-thermic background of a material deeply influences its magnetic behavior. For this reason several magnetic measurements protocol have been developed in order to evaluate the magnetic properties of a sample.

8.2.1 Magnetization Vs Temperature

For the magnetization Vs temperature analysis, the Zero Field Cooled (ZFC), Field Cooled (FC), and Thermo-Remanent Magnetization (TRM) represent frequently used protocols (**figure 8.3**). To perform ZFC measurements the sample is first cooled from room temperature to a low one in zero field; then the magnetization (M_{ZFC}) is recorded warming up the system, with a static applied magnetic field. With the same magnetic field applied, the M_{FC} is recorded during the subsequent cooling to the lowest starting temperature. In the TRM measurements, the sample is cooled from high temperature to a low one (usually quite under the occurrence of the SPM blocking) in an external magnetic field, then the field is turned off and the magnetization is measured warming up to the starting temperature.

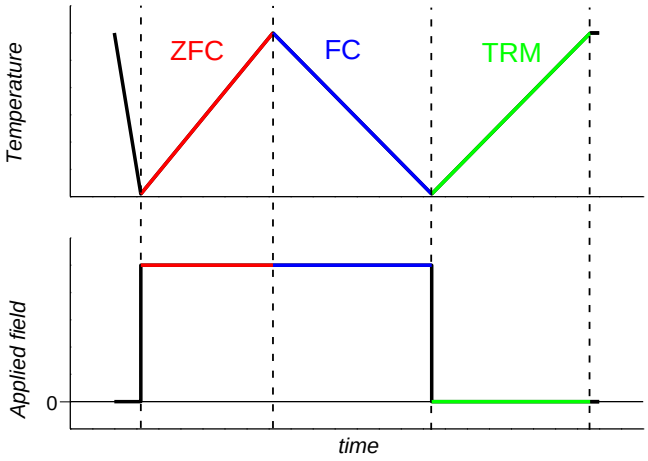

Figure 8.3: Graphical description of the ZFC-FC-TRM protocol.

For an ensemble of non-interacting nanoparticles, information about the effective magnetic anisotropy energy distribution *f(T)* can be obtained by the TRM derivative curve [254]:

$$f(t) \propto -\frac{dM_{TRM}}{dT} \qquad (8.1)$$

These two quantities are proportional, thus, at a given temperature *T'*, the thermal energy $k_B T'$ allows a fraction of particles to overcome their anisotropy energy barrier and to act as superparamagnet. At that temperature, the ratio between the fraction of unblocked (P_{SPM}) and that of blocked (P_B) particles can be defined as [180]:

$$R' = \frac{P_{SPM}}{P_B} = \frac{\int_{T'}^{Tmax} f(T)dT}{\int_{Tmin}^{T'} f(T)dT} \qquad (8.2)$$

where T_{min} and T_{max} represent the minimum and maximum temperatures covered in the range of measurement. According to the relation (8.1) and (8.2), the temperature corresponding to a value $R' = 1$ is identified as that in which the integral of the TRM derivative curve reaches 50% of its maximum value; such temperature is usually considered as the average blocking temperature T_B of the sample [32,180]. However, this definition does not consider the number of particles involved in in the SPM state, owning bigger particles larger magnetization contribution on the curve, in addition, as in composite samples, more than one distribution can be present, thus the evaluation of the respective average blocking temperature cannot be solved through the integral method. An alternative is to define T_B as the temperature corresponding to the peak of the derivative curve [255,256], assuming that the particles size distribution is symmetric. It is worth to mention that this evaluation can introduce a difference smaller than 10 % with respect the other definition [180].

8.2.2 Magnetization Vs Field

Magnetization Vs field curves have been measured in the range − 5 T to + 5 T of applied field (**figure 8.4**).

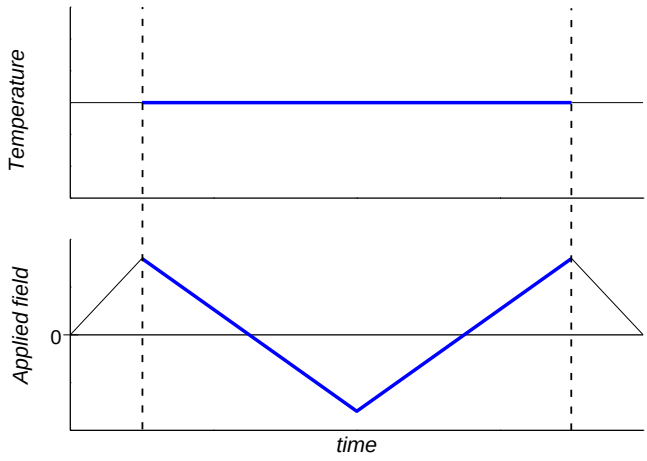

Figure 8.4: Graphical description of M Vs H protocol.

Figure 8.5 shows an example of a curve measured at 5 K, where the analyzed sample is below its superparamagnetic transition temperature, and it exhibits a hysteretic behavior. The thermal energy is not enough to allow the flipping of the magnetization orientation of nanoparticles, which happens only with the application of a threshold field, producing the irreversibility behavior in such curves. For NPs ensembles, the size distribution translates in a distribution of anisotropy energy; in addition, they are supposed to have a random orientation of magnetic anisotropy axis. This means that is possible to identify an average field, the coercive field $\mu_0 H_C$, as the field necessary to reverse the average magnetization from a negative to a positive value. This field is proportional to the average anisotropy energy of the nanoparticles. The point of irreversibility of M Vs H curves, which we have measured as the point in which the difference between the branches is under the 1% of their maximum value, can be taken as the saturation field $\mu_0 H_{SAT}$, the maximum field that is necessary to apply to reverse all the superspins moments.

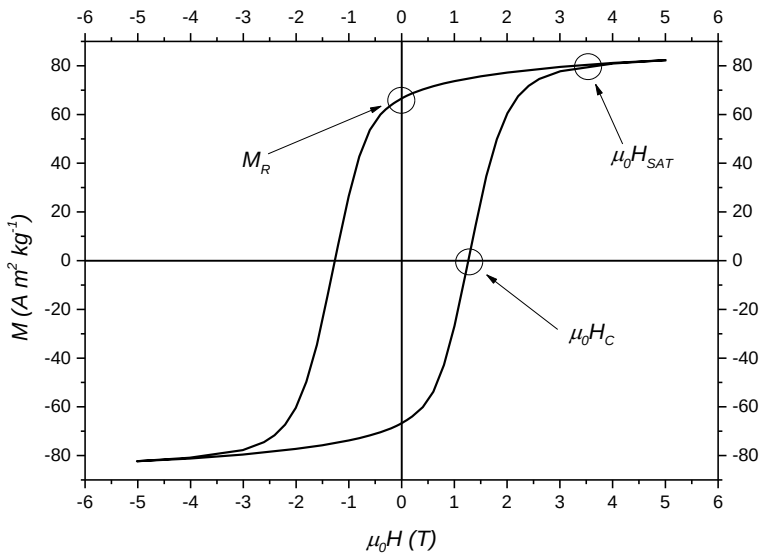

Figure 8.5: An example of M Vs H curve is shown. The coercive field $\mu_0 H_C$, the saturation field $\mu_0 H_{SAT}$ and the remanent magnetization M_R are evidenced.

the remanence magnetization M_R can be directly evaluated by the curve as the residual magnetization after the field removal. Furthermore the saturation magnetization M_S was extrapolated fitting the curves at high field using the Law of Approach to Saturation (LAS)[37]:

$$M = M_S\left(1 - \frac{A}{H} - \frac{B}{H^2}\right) \qquad (8.3)$$

where *A* and *B* are constant parameters. An alternative approach is to consider also the contribution of an high anisotropy component visible only at high field, which exhibits a paramagnetic linear behavior [257]:

$$M = M_0\left(1 - \frac{A}{H} - \frac{B}{H^2}\right) + \chi_d H \qquad (8.4)$$

where M_0 represent the spontaneous magnetization and χ_d the susceptibility of spins with the highest anisotropy (e.g., canted spins).

8.2.3 The remanent magnetization analysis

The field dependence of remanent magnetization was measured using the IRM (Isothermal Remanent Magnetization) and DCD (Direct Current Demagnetization) protocols. According to the IRM protocol, the sample, in the demagnetized state, was cooled in a zero magnetic field down to 5 K. Then, a small external field was applied for 10 s, and after it was switched off, the remanence (M_{IRM}) was measured. The process was repeated, increasing the field step by step up to 5 T. In a DCD measurement the initial state was the magnetically saturated one. After cooling the sample at 5 K, an external field of − 5 T was applied for 10 s, then it is turned off and the remanence (M_{DCD}) was measured. As in IRM a small external field in the opposite direction to magnetization was applied for 10 s and then switched off, and the remanent magnetization was measured. This was repeated increasing the field up to +5 T.

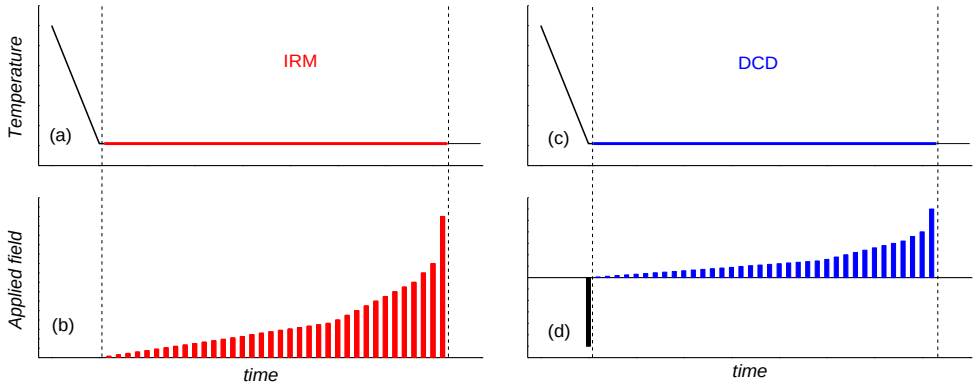

Figure 8.6: IRM (a and b) and DCD (c and d) protocols graphical description.

The differentiated remanence curve of M_{DCD} with respect to the field $\mu_0 H_{reverse}$ ($\chi_{irr} = dM_{DCD}/d\mu_0 H$), represents the irreversible component of the susceptibility. This quantity can be considered as a measure of the energy barrier distribution which, in a nanoparticles system, is associated with a distribution of particles coercivities and it is generally called the switching field distribution (SFD) [11,70,110].

ΔM-plots clarify picture of the interparticles interactions of a sample. For a system with uniaxial anisotropy and without interparticles interactions, the same energy barrier is calculated from IRM and DCD curves, as in Wohlfarth relation [225]:

$$m_{DCD}(H) = 1 - 2m_{IRM} \qquad (8.5)$$

where m_{DCD} and m_{IRM} are the values of magnetization normalized for the saturation remanence for DCD and IRM curves, respectively. Kelly et al. rewrote this expression as [258]:

$$\Delta M = m_{DCD}(H) - 1 + 2m_{IRM} \qquad (8.6)$$

In presence of interactions, the ΔM plot shows deviation from zero. Negative deviations are usually taken as indicative of the prevalence of interactions which stabilize the

demagnetized state (i.e., dipole-dipole interactions). Positive values are attributed to the prevalence of interactions promoting the magnetized state (i.e., exchange interactions) [70].

References

[1] Gaius Plinius Secundus (Plinius the elder), Naturalis Historia, n.d.

[2] Encylopaedia Britannica, Encylopaedia Br. (1989).

[3] M.N.. Baibich, J.M.. Broto, A.. Fert, F.N.. Van Dau, F.. Petroff, P.. Feitenne, et al., Giant Magnetoresistance of (001) Fe/(001)Cr Magnetic superlattices, Phys. Rev. Lett. 61 (1988) 2472–2475.

[4] J.F. Gregg, W. Allen, K. Ounadjela, M. Viret, M. Hehn, S.M. Thompson, et al., Giant magnetoresistive effects in a single element magnetic thin film, Phys. Rev. Lett. 77 (1996) 1–4. doi:10.1103/PhysRevLett.77.1580.

[5] C.L. Chien, J.Q. Xiao, J.S. Jiang, Giant negative magnetoresistance in granular ferromagnetic systems (invited), J. Appl. Phys. 73 (1993) 5309–5314. doi:10.1063/1.353765.

[6] D. Peddis, Magnetic Properties of Spinel Ferrite Nanoparticles : Influence of the Magnetic Structure, in: Magn. Nanoparticle Assem., 2014: pp. 159 –198.

[7] L. Suber, D. Peddis, Approaches to Synthesis and Characterization of Spherical and Anisometric Metal Oxide Magnetic Nanomaterials, in: Nanomater. Life Sci., Wiley, 2009.

[8] S. Morup, M.F. Hansen, C. Frandsen, Magnetic Nanoparticle, in: D.L. Andrews, G.D. Scholes, G.P. Wiederrecht (Eds.), Compr. Nanosci. Technol., Elsevier, New York, 2011: pp. 437–491.

[9] L. Néel, Théorie du trainage Magnétique des ferromagnétiques en grains fins avec applications aux terres cuites, Ann. Gèophysique. 5 (1949) 99–136.

[10] J.L. Dormann, D. Fiorani, E. Tronc, Magnetic Relaxation in Fine-Particle Systems, in: I. Prigogine, S.A. Rice (Eds.), Adv. Chem. Physics, Vol. 98, John Wiley & Sons, Inc., Hoboken, NJ, USA, 1997. doi:DOI: 10.1002/9780470141571.ch4.

[11] C. Binns, ed., Nanomagnetism: Fundamentals and Applications, Elsevier, Oxford, 2014.

[12] P. Tartaj, M. del P. Morales, S. Veintemillas-Verdaguer, T. González-Carreño, C.J. Serna, ıa del P. Pedro Tartaj1Morales1, et al., The preparation of magnetic nanoparticles for applications in biomedicine, J. Phys. D. Appl. Phys. 36 (2003) R182. http://iopscience.iop.org/0022-3727/36/13/202 (accessed August 29, 2012).

[13] J.B. Haun, T.-J. Yoon, H. Lee, R. Weissleder, Magnetic nanoparticle biosensors., Wiley Interdiscip. Rev. Nanomed. Nanobiotechnol. 2 (2010) 291–304. doi:10.1002/wnan.84.

[14] E. a Schultz-Sikma, H.M. Joshi, Q. Ma, K.W. Macrenaris, A.L. Eckermann, V.P. Dravid, et al., Probing the Chemical Stability of Mixed Ferrites: Implications for MR Contrast Agent Design., Chem. Mater. 23 (2011) 2657–2664. doi:10.1021/cm200509g.

[15] N. a Frey, S. Peng, K. Cheng, S. Sun, Magnetic nanoparticles: synthesis, functionalization, and applications in bioimaging and magnetic energy storage., Chem. Soc. Rev. 38 (2009) 2532–42. doi:10.1039/b815548h.

[16] C. Sun, J.S.H. Lee, M. Zhang, Magnetic nanoparticles in MR imaging and drug delivery., Adv. Drug Deliv. Rev. 60 (2008) 1252–65. doi:10.1016/j.addr.2008.03.018.

[17] P. Guardia, N. Pérez, A. Labarta, X. Batlle, Controlled synthesis of iron oxide nanoparticles over a wide size range Supporting information, Langmuir. 26 (2010) 5843–7. doi:10.1021/la903767e.

[18] D. Maity, S.N. Kale, R. Kaul-Ghanekar, J.-M. Xue, J. Ding, Studies of magnetite nanoparticles synthesized by thermal decomposition of iron (III) acetylacetonate in tri(ethylene glycol), J. Magn. Magn. Mater. 321 (2009) 3093–3098. doi:10.1016/j.jmmm.2009.05.020.

[19] N.D. Thorat, V.M. Khot, a B. Salunkhe, a I. Prasad, R.S. Ningthoujam, S.H. Pawar, Surface functionalized LSMO nanoparticles with improved colloidal stability for hyperthermia applications, J. Phys. D. Appl. Phys. 46 (2013) 105003. doi:10.1088/0022-3727/46/10/105003.

[20] M. Andrés Vergés, R. Costo, a G. Roca, J.F. Marco, G.F. Goya, C.J. Serna, et al., Uniform and water stable magnetite nanoparticles with

diameters around the monodomain–multidomain limit, J. Phys. D. Appl. Phys. 41 (2008) 134003. doi:10.1088/0022-3727/41/13/134003.

[21] K. Raj, B. Moskowitz, R. Casciari, Advances in ferrofluid technology, J. Magn. Magn. Mater. 149 (1995) 174–180. doi:10.1016/0304-8853(95)00365-7.

[22] Q.M. Kainz, O. Reiser, Polymer- and dendrimer-coated magnetic nanoparticles as versatile supports for catalysts, scavengers, and reagents, Acc. Chem. Res. 47 (2014) 667–677. doi:10.1021/ar400236y.

[23] R. Hudson, Y. Feng, R.S. Varma, A.H. Moores, Bare Magnetic Nanoparticles: Sustainable Synthesis and Applications in Catalytic Organic Transformations, Green Chem. 16 (2014) 4493–4505. doi:10.1039/c4gc00418c.

[24] A.S. Edelstein, R.C. Cammarata, Nanomaterials: Synthesis, Properties and Applications, Bristol, 1996.

[25] R. Skomski, P. Manchanda, P.K. Kumar, B. Balamurugan, A. Kashyap, D.J. Sellmyer, Predicting the Future of Permanent-Magnet Materials, IEEE Trans. Magn. 49 (2013) 3215–3220. doi:10.1109/TMAG.2013.2248139.

[26] S.N. Piramanayagam, T.C. Chong, Development in Data Storage, Wiley, Wiley, Singapore, 2012.

[27] M.L. Fdez-gubieda, A. Muela, J. Alonso, A. Garcı, M. Barandiara, R. Ferna, Magnetite Biomineralization in Magnetospirillum gryphiswaldense : Time_resolved Magnetic ans Structural Studies, ACS Nano. 7 (2013) 3297–3305.

[28] S. Bedanta, W. Kleemann, Supermagnetism, J. Phys. D. Appl. Phys. 42 (2009) 013001 1–28. doi:10.1088/0022-3727/42/1/013001.

[29] W.H. Meiklejohn, C.P. Bean, New magnetic anisotropy, Phys. Rev. 102 (1956) 1413–1414. http://journals.aps.org/pr/abstract/10.1103/PhysRev.105.904 (accessed December 1, 2014).

[30] A. López-Ortega, M. Estrader, G. Salazar-Alvarez, A.G. Roca, J. Nogués, Applications of exchange coupled bi-magnetic hard/soft and

soft/hard magnetic core/shell nanoparticles, Phys. Rep. 553 (2015) 1–32. doi:http://dx.doi.org/10.1016/j.physrep.2014.09.007.

[31] A. López-Ortega, M. Estrader, G. Salazar-Alvarez, A.G. Roca, J. Nogués, Applications of exchange coupled bi-magnetic hard/soft and soft/hard magnetic core/shell nanoparticles, Phys. Rep. (2014). doi:10.1016/j.physrep.2014.09.007.

[32] C. Cannas, A. Musinu, G. Piccaluga, D. Fiorani, D. Peddis, H.K. Rasmussen, et al., Magnetic properties of cobalt ferrite-silica nanocomposites prepared by a sol-gel autocombustion technique., J. Chem. Phys. 125 (2006) 164714 1–11. doi:10.1063/1.2354475.

[33] A.R. West, Solid State Chemistry and its applications, 1984.

[34] C. Liu, B. Zou, A.J. Rondinone, Z.J. Zhang, Chemical Control of Superparamagnetic Properties of Magnesium and Cobalt Spinel Ferrite Nanoparticles through Atomic Level Magnetic Couplings, J. Am. Chem. Soc. 122 (2000) 6263–6267.

[35] J.M.D. Coey, Magnetism and Magnetic Materials, Cambridge University Press, 2010.

[36] S. Blundell, Order and magnetic structures, in: Magn. Condens. Matter, Oxford Univesity Press, Oxford, 2001: pp. 85–110.

[37] A.H. Morrish, The physical principles of magnetism, Wiley-IEEE Press, New York, 2001.

[38] F. Wiekhorst, E. Shevchenko, H. Weller, J. Kötzler, Anisotropic superparamagnetism of monodispersive cobalt-platinum nanocrystals, Phys. Rev. B. 67 (2003) 224416. doi:10.1103/PhysRevB.67.224416.

[39] L. Néel, No Title, Ann. Géophysique. 5 (1949) 99–109.

[40] W.F.J. Brown, Thermal Fluctuations of Single-Domain Particle, Phys. Rev. Lett. 130 (1963).

[41] E.C. Stoner, E.P. Wohlfarth, A Mechanism of Magnetic Hysteresis in Heterogeneous Alloys, Philos. Trans. R. Soc. London A Math. Phys. Eng. Sci. 240 (1948) 599–642. http://rsta.royalsocietypublishing.org/content/240/826/599.abstract.

[42] M. Knobel, W. Nunes, Superparamagnetism and other magnetic features in granular materials: a review on ideal and real systems, J. Nanosci. Nanotechnol. 8 (2008) 1880–1885. doi:10.1166/jnn.2008.017.

[43] S. Mørup, M.F. Hansen, C. Frandsen, Magnetic interactions between nanoparticles., Beilstein J. Nanotechnol. 1 (2010) 182–190. doi:10.3762/bjnano.1.22.

[44] C. Vestal, Q. Song, Z. Zhang, Effects of interparticle interactions upon the magnetic properties of CoFe2O4 and MnFe2O4 nanocrystals, J. Phys. Chem. B. (2004) 18222–18227. http://pubs.acs.org/doi/abs/10.1021/jp0464526 (accessed July 4, 2014).

[45] J. a. De Toro, S.S. Lee, D. Salazar, J.L. Cheong, P.S. Normile, P. Muñiz, et al., A nanoparticle replica of the spin-glass state, Appl. Phys. Lett. 102 (2013) 183104. doi:10.1063/1.4804187.

[46] L. Theil Kuhn, K. Lefmann, C. Bahl, S. Ancona, P. -a. Lindgård, C. Frandsen, et al., Neutron study of magnetic excitations in 8-nm α-Fe2O3 nanoparticles, Phys. Rev. B. 74 (2006) 184406. doi:10.1103/PhysRevB.74.184406.

[47] V. Skumryev, S. Stoyanov, Y. Zhang, Beating the superparamagnetic limit with exchange bias, Nature. 423 (2003) 19–22. doi:10.1038/nature01750.1.

[48] D. Peddis, P.E. Jonsson, S. Laureti, G. Varvaro, Magnetic Interactions: A Tool to Modify the Magnetic Properties of Materials Based on Nanoparticles, in: C. Binns (Ed.), Nanomagnetism Fundam. Appl., Elsevier, 2014: pp. 129–179.

[49] M. a. Ruderman, C. Kittel, M. a. Ruderman, Indirect Exchange Coupling of nuclear Magnetic Moments by Conduction Electrons, Phys. Rev. B. 96 (1954) 99–102. doi:10.1103/PhysRev.96.99.

[50] T. Kasuya, A Theory of Metallic Ferro- and Antiferromagnetism on Zener's Model, Prog. Theor. Phys. 16 (1956) 45–57. doi:10.1143/PTP.16.45.

[51] K. Yosida, Y. Kei, Magnetic Properties of Cu-Mn Alloys, Phys. Rev. Lett. 106 (1957). doi:10.1103/PhysRev.106.893.

[52] V. Kondratyev, H. Lutz, Shell Effect in Exchange Coupling of Transition Metal Dots and Their Arrays, Phys. Rev. Lett. 81 (1998) 4508–4511. doi:10.1103/PhysRevLett.81.4508.

[53] M. Scheinfein, K. Schmidt, K. Heim, G. Hembree, Magnetic Order in Two-Dimensional Arrays of Nanometer-Sized Superparamagnets, Phys. Rev. Lett. 76 (1996) 1541–1544. doi:10.1103/PhysRevLett.76.1541.

[54] C. Cannas, G. Concas, D. Gatteschi, A. Falqui, A. Musinu, G. Piccaluga, et al., Superparamagnetic behaviour of [gamma]-Fe2O3 nanoparticles dispersed in a silica matrix, Phys. Chem. Chem. Phys. 3 (2001) 832–838. doi:10.1039/B008645M.

[55] C. Cannas, G. Concas, D. Gatteschi, A. Musinu, G. Piccaluga, C. Sangregorio, How to tailor maghemite particle size in [gamma]-Fe2O3-SiO2 nanocomposites, J. Mater. Chem. 12 (2002) 3141–3146. doi:10.1039/B204292D.

[56] C. Cannas, a. Ardu, a. Musinu, D. Peddis, G. Piccaluga, Spherical Nanoporous Assemblies of Iso-Oriented Cobalt Ferrite Nanoparticles: Synthesis, Microstructure, and Magnetic Properties, Chem. Mater. 20 (2008) 6364–6371. doi:10.1021/cm801839s.

[57] C. Liu, B. Zou, A.J. Rondinone, Z.J. Zhang, Reverse micelle synthesis and characterization of superparamagnetic MnFe2O4 spinel ferrite nanocrystallites, J. Am. Chem. Soc. 104 (2000) 6263–6267. doi:10.1021/ja000784g.

[58] S. Komarneni, E. Fregeau, E. Breval, R. Roy, Hydrothermal Preparation of Ultrafine Ferrites and Their Sintering, J. Am. Ceram. Soc. 71 (1988) C–26–C–28. doi:10.1111/j.1151-2916.1988.tb05773.x.

[59] S. Sun, H. Zeng, D.B. Robinson, S. Raoux, P.M. Rice, S.X. Wang, et al., Monodisperse MFe2O4 (M = Fe, Co, Mn) Nanoparticles, J. Am. Chem. Soc. 126 (2003) 273–279. doi:10.1021/ja0380852.

[60] C. Cannas, A. Musinu, A. Ardu, F. Orrù, D. Peddis, M. Casu, et al., CoFe 2 O 4 and CoFe 2 O 4 /SiO 2 Core/Shell Nanoparticles: Magnetic and Spectroscopic Study, Chem. Mater. 22 (2010) 3353–3361. doi:10.1021/cm903837g.

[61] C. Cannas, A. Ardu, D. Peddis, C. Sangregorio, G. Piccaluga, A. Musinu, Surfactant-assisted route to fabricate CoFe2O4 individual

nanoparticles and spherical assemblies., J. Colloid Interface Sci. 343 (2010) 415–22. doi:10.1016/j.jcis.2009.12.007.

[62] F. Fiévet, R. Brayner, The Polyol Process, in: R. Brayner, F. Fiévet, T. Coradin (Eds.), Nanomater. A Danger or a Promise?, Springer London, 2013: pp. 1–25. doi:10.1007/978-1-4471-4213-3_1.

[63] W. Cai, J. Wan, Facile synthesis of superparamagnetic magnetite nanoparticles in liquid polyols., J. Colloid Interface Sci. 305 (2007) 366–70. doi:10.1016/j.jcis.2006.10.023.

[64] G. Baldi, D. Bonacchi, C. Innocenti, G. Lorenzi, C. Sangregorio, Cobalt ferrite nanoparticles: The control of the particle size and surface state and their effects on magnetic properties, J. Magn. Magn. Mater. 311 (2007) 10–16. doi:10.1016/j.jmmm.2006.11.157.

[65] R. Hergt, S. Dutz, M. Röder, Effects of size distribution on hysteresis losses of magnetic nanoparticles for hyperthermia., J. Phys. Condens. Matter. 20 (2008) 385214. doi:10.1088/0953-8984/20/38/385214.

[66] N. Frey, S. Sun, Magnetic Nanoparticle for Information Storage Applications, in: Inorg. Nanoparticles Synth. Appl. Perspect., 2010: pp. 33–68. http://66.35.39.81:11081/nano/publications/just-in-print/K10915_chapter3 (2).pdf (accessed December 1, 2014).

[67] H.J. Richter, Density limits imposed by the microstructure of magnetic recording media, J. Magn. Magn. Mater. 321 (2009) 467–476. doi:10.1016/j.jmmm.2008.04.161.

[68] M. Gaumet, A. Vargas, R. Gurny, F. Delie, Nanoparticles for drug delivery: the need for precision in reporting particle size parameters., Eur. J. Pharm. Biopharm. 69 (2008) 1–9. doi:10.1016/j.ejpb.2007.08.001.

[69] R.H. Kodama, a. E. Berkowitz, E.J. McNiff, S. Foner, Surface spin disorder in ferrite nanoparticles, J. Appl. Phys. 81 (1997) 5552. doi:10.1063/1.364659.

[70] D. Peddis, F. Orrù, A. Ardu, C. Cannas, A. Musinu, G. Piccaluga, Interparticle Interactions and Magnetic Anisotropy in Cobalt Ferrite Nanoparticles: Influence of Molecular Coating, Chem. Mater. 24 (2012) 1062–1071. doi:10.1021/cm203280y.

[71] R. Rakshit, M. Mandal, M. Pal, K. Mandal, Tuning of magnetic properties of CoFe2O4 nanoparticles through charge transfer effect, Appl. Phys. Lett. 104 (2014) 092412. doi:10.1063/1.4867706.

[72] J. Salafranca, J. Gazquez, N. Pérez, A. Labarta, S.T. Pantelides, S.J. Pennycook, et al., Surfactant organic molecules restore magnetism in metal-oxide nanoparticle surfaces., Nano Lett. 12 (2012) 2499–503. doi:10.1021/nl300665z.

[73] Y. Tanaka, S. Saita, S. Maenosono, Influence of surface ligands on saturation magnetization of FePt nanoparticles, Appl. Phys. Lett. 92 (2008) 093117. doi:10.1063/1.2891083.

[74] H. Yang, T. Ogawa, D. Hasegawa, M. Takahashi, Synthesis and magnetic properties of monodisperse magnetite nanocubes, J. Appl. Phys. 103 (2008) 07D526. doi:10.1063/1.2833820.

[75] N. Bao, L. Shen, W. An, P. Padhan, C. Heath Turner, A. Gupta, Formation Mechanism and Shape Control of Monodisperse Magnetic CoFe 2 O 4 Nanocrystals, Chem. Mater. 21 (2009) 3458–3468. doi:10.1021/cm901033m.

[76] Q. Song, Z.J. Zhang, Shape control and associated magnetic properties of spinel cobalt ferrite nanocrystals., J. Am. Chem. Soc. 126 (2004) 6164–8. doi:10.1021/ja049931r.

[77] S.-H. Noh, W. Na, J.-T. Jang, J.-H. Lee, E.J. Lee, S.H. Moon, et al., Nanoscale magnetism control via surface and exchange anisotropy for optimized ferrimagnetic hysteresis., Nano Lett. 12 (2012) 3716–21. doi:10.1021/nl301499u.

[78] G. Salazar-Alvarez, J. Qin, V. Sepelak, Cubic versus spherical magnetic nanoparticles: the role of surface anisotropy, J. Am. Chem. Soc. (2008) 13234–13239. http://pubs.acs.org/doi/abs/10.1021/ja0768744 (accessed March 16, 2012).

[79] M.F.M. Hansen, S. Mørup, Models for the dynamics of interacting magnetic nanoparticles, J. Magn. Magn. Mater. 184 (1998) L262–274. doi:10.1016/S0304-8853(97)01165-7.

[80] D. Fiorani, J.L. Dormann, R. Cherkaoui, E. Tronc, F. Lucari, F. D'Orazio, et al., Collective magnetic state in nanoparticles systems, J.

Magn. Magn. Mater. 196-197 (1999) 143–147. doi:10.1016/S0304-8853(98)00694-5.

[81] P. Jönsson, Superparamagnetism and spin glass dynamics of interacting magnetic nanoparticle systems, Adv. Chem. Phys. (2004) 1–62. http://books.google.com/books?hl=en&lr=&id=wK3Vhq-VnBQC&oi=fnd&pg=PA191&dq=Superparamagnetism+and+Spin+Glass+Dynamics+of+Interacting+Magnetic+Nanoparticle+Systems&ots=GbMBLFl3b7&sig=eAGKFPhK4XwjourmYSMOsas1kuU (accessed March 28, 2014).

[82] R.H. Victora, X. Shen, Composite media for perpendicular magnetic recording, IEEE Trans. Magn. 41 (2005) 537–542. doi:10.1109/TMAG.2005.855263.

[83] Y. Wang, R. Wang, H.-L. Xie, J.-M. Bai, F.-L. Wei, Micromagnetic simulation with three models of FeCo/L1 0 FePt exchange-coupled particles for bit-patterned media, Chinese Phys. B. 22 (2013) 068506. doi:10.1088/1674-1056/22/6/068506.

[84] A. Demortière, P. Panissod, B.P. Pichon, G. Pourroy, D. Guillon, B. Donnio, et al., Size-dependent properties of magnetic iron oxide nanocrystals., Nanoscale. 3 (2011) 225–32. doi:10.1039/c0nr00521e.

[85] A.G. Roca, D. Carmona, N. Miguel-Sancho, O. Bomatí-Miguel, F. Balas, C. Piquer, et al., Surface functionalization for tailoring the aggregation and magnetic behaviour of silica-coated iron oxide nanostructures., Nanotechnology. 23 (2012) 155603. doi:10.1088/0957-4484/23/15/155603.

[86] A.G. Roca, D. Niznansky, J. Poltierova-Vejpravova, B. Bittova, M. a. González-Fernández, C.J. Serna, et al., Magnetite nanoparticles with no surface spin canting, J. Appl. Phys. 105 (2009) 114309. doi:10.1063/1.3133228.

[87] D. Peddis, C. Cannas, A. Musinu, A. Ardu, F. Orrù, D. Fiorani, et al., Beyond the Effect of Particle Size: Influence of CoFe2O4 Nanoparticle Arrangements on Magnetic Properties, Chem. Mater. 25 (2013) 2–10. doi:10.1021/cm303352r.

[88] S. Si, C. Li, X. Wang, D. Yu, Q. Peng, Y. Li, Magnetic monodisperse Fe3O4 nanoparticles, Cryst. Growth Des. 5 (2005) 12–14. http://pubs.acs.org/doi/abs/10.1021/cg0497905 (accessed July 3, 2014).

[89] L. Hu, C. De Montferrand, Y. Lalatonne, L. Motte, A. Brioude, Effect of Cobalt Doping Concentration on the Crystalline Structure and Magnetic Properties of Monodisperse Co, J. Phys. Chem. (2012).

[90] J.I. Gittleman, B. Abeles, S. Bozowski, Superparamagnetism and relaxation effects in granular Ni-SiO2 and Ni-Al2O3 films, Phys. Rev. B. 9 (1974).

[91] D. Peddis, C. Cannas, A. Musinu, G. Piccaluga, Coexistence of Superparmagnetism and Spin-Glass Like Magnetic Ordering Phenomena in a CoFe2O4-SiO2 Nanocomposite, J. Phys. Chem. C. 112 (2008) 5141–5147. doi:10.1021/jp076704d.

[92] A.G. Roca, M.P. Morales, K. O'Grady, C.J. Serna, K. O'Grady, Structural and magnetic properties of uniform magnetite nanoparticles prepared by high temperature decomposition of organic precursors, Nanotechnology. 17 (2006) 2783–2788. doi:10.1088/0957-4484/17/11/010.

[93] R. Kodama, A. Berkowitz, E.M. Jr, S. Foner, E. McNiff, Surface Spin Disorder in NiFe2O4 Nanoparticles., Phys. Rev. Lett. 77 (1996) 394–397. http://www.ncbi.nlm.nih.gov/pubmed/10062440 (accessed July 21, 2014).

[94] N. Cordente, M. Respaud, F. Senocq, M.-J. Casanove, C. Amiens, B. Chaudret, Synthesis and Magnetic Properties of Nickel Nanorods, Nano Lett. 1 (2001) 565–568. doi:10.1021/nl0100522.

[95] C.R. Vestal, Z.J. Zhang, Effects of surface coordination chemistry on the magnetic properties of MnFe(2)O(4) spinel ferrite nanoparticles., J. Am. Chem. Soc. 125 (2003) 9828–33. doi:10.1021/ja035474n.

[96] D. Peddis, N. Yaacoub, M. Ferretti, A. Martinelli, G. Piccaluga, A. Musinu, et al., Cationic distribution and spin canting in CoFe2O4 nanoparticles., J. Phys. Condens. Matter. 23 (2011) 426004 1–8. doi:10.1088/0953-8984/23/42/426004.

[97] N.N. Greenwood, T.C. Gibb, Mössbauer Spectroscopy, Springer, 2013. doi:10.1007/978-94-009-5697-1.

[98] G.M. Bancroft, Mössbauer spectroscopy: an introduction for inorganic chemists and geochemist, McGraw-Hill, London, 1973.

[99] Steen Mørup, Mossbauer spectroscopy and its applications in materials science, (2004).

[100] E. Tronc, P. Prené, J.P. Jolivet, J.L. Dormann, J.M. Grenèche, Spin Canting in γ-Fe2O3 Nanoparticles, Hyperfine Interact. 112 (1998) 97–100. doi:10.1023/A:1011092712136.

[101] J. Coey, Noncollinear spin arrangement in ultrafine ferrimagnetic crystallites, Phys. Rev. Lett. 27 (1971) 1970–1972. http://journals.aps.org/prl/abstract/10.1103/PhysRevLett.27.1140 (accessed July 10, 2014).

[102] Y. Yin, a P. Alivisatos, Colloidal nanocrystal synthesis and the organic-inorganic interface., Nature. 437 (2005) 664–70. doi:10.1038/nature04165.

[103] W. Wu, Q. He, C. Jiang, Magnetic iron oxide nanoparticles: synthesis and surface functionalization strategies, Nanoscale Res. Lett. 3 (2009) 397–415. doi:10.1007/s11671-008-9174-9.

[104] D. Ling, M.J. Hackett, T. Hyeon, Surface ligands in synthesis, modification, assembly and biomedical applications of nanoparticles, Nano Today. 9 (2014) 457–477. doi:10.1016/j.nantod.2014.06.005.

[105] C. Berry, A. Curtis, Functionalisation of magnetic nanoparticles for applications in biomedicine, J. Phys. D. Appl. Phys. 198 (2003). http://iopscience.iop.org/0022-3727/36/13/203 (accessed February 11, 2013).

[106] M. Günay, H. Erdemi, A. Baykal, H. Sözeri, M.S. Toprak, Triethylene glycol stabilized MnFe2O4 nanoparticle: Synthesis, magnetic and electrical characterization, Mater. Res. Bull. 48 (2013) 1057–1064. doi:10.1016/j.materresbull.2012.11.097.

[107] H. Deligöz, A. Baykal, E.E. Tanrıverdi, Z. Durmus, M.S. Toprak, Synthesis, structural and electrical properties of triethylene glycol (TREG) stabilized Mn0.2Co0.8Fe2O4 NPs, Mater. Res. Bull. 47 (2012) 537–543. doi:10.1016/j.materresbull.2011.12.050.

[108] A. Baykal, H. Deligöz, H. Sozeri, Z. Durmus, M.S. Toprak, Triethylene Glycol Stabilized CoFe2O4 Nanoparticles, J. Supercond. Nov. Magn. 25 (2012) 1879–1892. doi:10.1007/s10948-012-1500-x.

[109] H. Yang, C. Zhang, X. Shi, H. Hu, X. Du, Y. Fang, et al., Water-soluble superparamagnetic manganese ferrite nanoparticles for magnetic resonance imaging., Biomaterials. 31 (2010) 3667–3673. doi:10.1016/j.biomaterials.2010.01.055.

[110] K. O'Grady, R.W. Chantrelll, Remanence curves of Fine particle system I: Experimental studies, Int. Work. Stud. Magn. Prop. Fine Part. Their Relev. to Mater. Sci. (1991) 93–102.

[111] M. Artus, L. Ben Tahar, F. Herbst, L. Smiri, F. Villain, N. Yaacoub, et al., Size-dependent magnetic properties of CoFe2O4 nanoparticles prepared in polyol., J. Phys. Condens. Matter Condens. Matter. 23 (2011) 506001. doi:10.1088/0953-8984/23/50/506001.

[112] M. Gonzales-Weimuller, M. Zeisberger, K.M. Krishnan, Size-dependant heating rates of iron oxide nanoparticles for magnetic fluid hyperthermia, J. Magn. Magn. Mater. 321 (2009) 1947–1950. doi:10.1016/j.jmmm.2008.12.017.

[113] G. Muscas, G. Singh, W.R. Glomm, R. Mathieu, P.A. Kumar, G. Concas, et al., Tuning the Size and Shape of Oxide Nanoparticles by Controlling Oxygen Content in the Reaction Environment: Morphological Analysis by Aspect Maps, Chem. Mater. 27 (2015) 1982–1990. doi:10.1021/cm5038815.

[114] W. Pyrz, D. Buttrey, Particle size determination using TEM: a discussion of image acquisition and analysis for the novice microscopist, Langmuir. (2008) 11350–11360. http://pubs.acs.org/doi/abs/10.1021/la801367j (accessed May 20, 2014).

[115] M. Reetz, M. Maase, Computer image processing of transmission electron micrograph pictures as a fast and reliable tool to analyze the size of nanoparticles, J. Phys. …. 104 (2000) 8779–8781. doi:10.1021/jp000328e.

[116] J. Schindelin, I. Arganda-Carreras, E. Frise, V. Kaynig, M. Longair, T. Pietzsch, et al., Fiji: an open-source platform for biological-image analysis, Nat Meth. 9 (2012) 676–682. http://dx.doi.org/10.1038/nmeth.2019.

[117] E. Limpert, W. a. Stahel, M. Abbt, Log-normal Distributions across the Sciences: Keys and Clues, Bioscience. 51 (2001) 341. doi:10.1641/0006-3568(2001)051[0341:LNDATS]2.0.CO;2.

[118] L. Kiss, J. Söderlund, New approach to the origin of lognormal size distributions of nanoparticles, Nanotechnology. 25 (1999). http://iopscience.iop.org/0957-4484/10/1/006 (accessed August 6, 2014).

[119] C.G. Granqvist, R.A. Buhrman, Ultrafine metal particles, J. Appl. Phys. 14853 (1976) 2200. doi:10.1063/1.322870.

[120] A.T. Ngo, P. Bonville, M.P. Pileni, Nanoparticles of Co x Fe y properties z O 4 : Synthesis and superparamagnetic, Eur. Phys. J. B. 592 (1999) 583–592. doi:http://dx.doi.org/10.1007/s100510050801.

[121] A.P. Stevenson, D. Blanco Bea, S. Civit, S. Antoranz Contera, A. Iglesias Cerveto, S. Trigueros, Three strategies to stabilise nearly monodispersed silver nanoparticles in aqueous solution., Nanoscale Res. Lett. 7 (2012) 151. doi:10.1186/1556-276X-7-151.

[122] I. Römer, A.J. Gavin, T. a White, R.C. Merrifield, J.K. Chipman, M.R. Viant, et al., The critical importance of defined media conditions in Daphnia magna nanotoxicity studies., Toxicol. Lett. 223 (2013) 103–8. doi:10.1016/j.toxlet.2013.08.026.

[123] R. Fisker, J. Carstensen, M. Hansen, Estimation of nanoparticle size distributions by image analysis, J. Nanoparticle …. (2000) 267–277. http://link.springer.com/article/10.1023/A:1010023316775 (accessed May 20, 2014).

[124] V. Annapu Reddy, N.P. Pathak, R. Nath, Particle size dependent magnetic properties and phase transitions in multiferroic BiFeO3 nano-particles, J. Alloys Compd. 543 (2012) 206–212. doi:10.1016/j.jallcom.2012.07.098.

[125] M. Sugimoto, The past, present, and future of ferrites, J. Am. Ceram. Soc. 82 (1999) 269–280. http://onlinelibrary.wiley.com/doi/10.1111/j.1551-2916.1999.tb20058.x/abstract (accessed October 6, 2013).

[126] X. Batlle, N. Pérez, P. Guardia, O. Iglesias, A. Labarta, F. Bartolomé, et al., Magnetic nanoparticles with bulklike properties (invited), J. Appl. Phys. 109 (2011) 07B524. doi:10.1063/1.3559504.

[127] G. Muscas, G. Concas, C. Cannas, A. Musinu, A. Ardu, F. Orrù, et al., Magnetic Properties of Small Magnetite Nanocrystals, J. Phys. Chem. C. 117 (2013) 23378–23384. doi:10.1021/jp407863s.

[128] C. Singh, A. Goyal, S. Singhal, Nickel doped cobalt ferrite nanoparticles: Efficient catalysts for the reduction of nitroaromatic compounds and photo-oxidative degradation of toxic dyes., Nanoscale. 6 (2014) 7959–7970. doi:10.1039/C4NR01730G.

[129] A. Hannour, D. Vincent, F. Kahlouche, A. Tchangoulian, S. Neveu, V. Dupuis, Self-biased cobalt ferrite nanocomposites for microwave applications, J. Magn. Magn. Mater. 353 (2014) 29–33. doi:10.1016/j.jmmm.2013.10.010.

[130] D. Carta, M.F. Casula, A. Falqui, D. Loche, G. Mountjoy, C. Sangregorio, et al., A Structural and Magnetic Investigation of the Inversion Degree in Ferrite Nanocrystals MFe2O4 (M = Mn, Co, Ni), J. Phys. Chem. C. 113 (2009) 8606–8615. doi:10.1021/jp901077c.

[131] B.G. Toksha, S.E. Shirsath, S.M. Patange, K.M. Jadhav, Structural investigations and magnetic properties of cobalt ferrite nanoparticles prepared by sol–gel auto combustion method, Solid State Commun. 147 (2008) 479–483. doi:10.1016/j.ssc.2008.06.040.

[132] T. Hyeon, Y. Chung, J. Park, S.S. Lee, Y.-W. Kim, B.H. Park, Synthesis of Highly Crystalline and Monodisperse Cobalt Ferrite Nanocrystals, J. Phys. Chem. B. 106 (2002) 6831–6833. doi:10.1021/jp026042m.

[133] A.P. Herrera, L. Polo-Corrales, E. Chavez, J. Cabarcas-Bolivar, O.N.C.C. Uwakweh, C. Rinaldi, Influence of aging time of oleate precursor on the magnetic relaxation of cobalt ferrite nanoparticles synthesized by the thermal decomposition method, J. Magn. Magn. Mater. 328 (2013) 41–52. doi:10.1016/j.jmmm.2012.09.069.

[134] Y. Yu, A. Mendoza-Garcia, B. Ning, S. Sun, Cobalt-substituted magnetite nanoparticles and their assembly into ferrimagnetic nanoparticle arrays., Adv. Mater. 25 (2013) 3090–4. doi:10.1002/adma.201300595.

[135] J. Xie, S. Peng, N. Brower, N. Pourmand, S.X. Wang, S. Sun, One-pot synthesis of monodisperse iron oxide nanoparticles for potential biomedical applications, Pure Appl. Chem. 78 (2006) 1003–1014. doi:10.1351/pac200678051003.

[136] S. Sun, H. Zeng, D.B. Robinson, S. Raoux, P.M. Rice, S.X. Wang, et al., Monodisperse MFe 2 O 4 (M) Fe, Co, Mn) Nanoparticles, J. Am. Chem. Soc. 4 (2004) 126–132.

[137] M. Levy, A. Quarta, A. Espinosa, A. Figuerola, C. Wilhelm, M. García-Hernández, et al., Correlating Magneto-Structural Properties to Hyperthermia Performance of Highly Monodisperse Iron Oxide Nanoparticles Prepared by a Seeded-Growth Route, Chem. Mater. 23 (2011) 4170–4180. doi:10.1021/cm201078f.

[138] R. Viswanatha, D.D. Sarma, Growth of Nanocrystals in Solution, in: Nanomater. Chem., Wiley-VCH Verlag GmbH & Co. KGaA, 2007: pp. 139–170. doi:10.1002/9783527611362.ch4.

[139] V. LaMer, R. Dinegar, Theory, production and mechanism of formation of monodispersed hydrosols, J. Am. Chem. Soc. 72 (1950) 4847–4854. http://pubs.acs.org/doi/abs/10.1021/ja01167a001 (accessed April 18, 2013).

[140] I.M. Lifshitz, V. V Slyozov, The kinetics of precipitation from supersaturated solid solutions, J. Phys. Chem. Solids. 19 (1961) 35–50. doi:http://dx.doi.org/10.1016/0022-3697(61)90054-3.

[141] C. Wagner, Theorie dealtering von Niederschlägen durch umlösen., Z. Elektrochem.. 65 (1961) 581–591.

[142] E. Fantechi, G. Campo, D. Carta, A. Corrias, C. de Julián Fernández, D. Gatteschi, et al., Exploring the Effect of Co Doping in Fine Maghemite Nanoparticles, J. Phys. Chem. C. 116 (2012) 8261–8270. doi:10.1021/jp300806j.

[143] Z. Li, Y. Ma, L. Qi, One-pot synthesis of CoFe–Fe3O4 nanocomposites with tunable magnetic properties and long term stability, Mater. Res. Bull. 48 (2013) 3157–3163. doi:10.1016/j.materresbull.2013.04.063.

[144] Z. Xu, C. Shen, Y. Tian, X. Shi, H.-J. Gao, Organic phase synthesis of monodisperse iron oxide nanocrystals using iron chloride as precursor, Nanoscale. 2 (2010) 1027–1032. doi:10.1039/B9NR00400A.

[145] B. Balamurugan, D.J. Sellmyer, G.C. Hadjipanayis, R. Skomski, Prospects for nanoparticle-based permanent magnets, Scr. Mater. (2012).

[146] J.S. Jiang, S.D. Bader, Rational design of the exchange-spring permanent magnet., J. Phys. Condens. Matter. 26 (2014) 064214. doi:10.1088/0953-8984/26/6/064214.

[147] C. Vázquez-Vázquez, M. a. López-Quintela, M.C. Buján-Núñez, J. Rivas, Finite size and surface effects on the magnetic properties of cobalt ferrite nanoparticles, J. Nanoparticle Res. 13 (2010) 1663–1676. doi:10.1007/s11051-010-9920-7.

[148] R. Valenzuela, Magnetic ceramics, Cambridge University Press, 2005.

[149] S. Laureti, G. Varvaro, a M. Testa, D. Fiorani, E. Agostinelli, G. Piccaluga, et al., Magnetic interactions in silica coated nanoporous assemblies of CoFe2O4 nanoparticles with cubic magnetic anisotropy., Nanotechnology. 21 (2010) 315701. doi:10.1088/0957-4484/21/31/315701.

[150] J. Lynch, J. Zhuang, T. Wang, D. LaMontagne, H. Wu, Y.C. Cao, Gas-bubble effects on the formation of colloidal iron oxide nanocrystals., J. Am. Chem. Soc. 133 (2011) 12664–74. doi:10.1021/ja2032597.

[151] T. Sugimoto, Preparation of monodispersed colloidal particles, Adv. Colloid Interface Sci. 28 (1987) 65–108. http://www.sciencedirect.com/science/article/pii/000186868780009X (accessed March 4, 2014).

[152] Y. Chen, E. Johnson, X. Peng, Formation of monodisperse and shape-controlled MnO nanocrystals in non-injection synthesis: self-focusing via ripening., J. Am. Chem. Soc. 129 (2007) 10937–47. doi:10.1021/ja073023n.

[153] N.J.J. Johnson, A. Korinek, C. Dong, F.C.J.M. van Veggel, Self-focusing by Ostwald ripening: a strategy for layer-by-layer epitaxial growth on upconverting nanocrystals., J. Am. Chem. Soc. 134 (2012) 11068–71. doi:10.1021/ja302717u.

[154] B. Voss, M. Haase, Intrinsic focusing of the particle size distribution in colloids containing nanocrystals of two different crystal phases., ACS Nano. 7 (2013) 11242–54. doi:10.1021/nn405026w.

[155] P. Dagtepe, V. Chikan, Quantized Ostwald Ripening of Colloidal Nanoparticles, J. Phys. Chem. C. 3701 (2010) 16263–16269. http://pubs.acs.org/doi/abs/10.1021/jp105071a (accessed January 30, 2014).

[156] J. Thessing, J. Qian, H. Chen, N. Pradhan, X. Peng, Interparticle influence on size/size distribution evolution of nanocrystals., J. Am. Chem. Soc. 129 (2007) 2736–7. doi:10.1021/ja068072z.

[157] Q. Song, Z.J. Zhang, Correlation between spin-orbital coupling and the superparamagnetic properties in magnetite and cobalt ferrite spinel nanocrystals., J. Phys. Chem. B. 110 (2006) 11205–9. doi:10.1021/jp060577o.

[158] E. Tirosh, G. Shemer, Optimizing cobalt ferrite nanocrystal synthesis using a magneto-optical probe, Chem. Mater. (2006) 465–470. http://pubs.acs.org/doi/abs/10.1021/cm052401p (accessed March 9, 2012).

[159] M. V Limaye, S.B. Singh, S.K. Date, D. Kothari, V.R. Reddy, A. Gupta, et al., High coercivity of oleic acid capped CoFe2O4 nanoparticles at room temperature., J. Phys. Chem. B. 113 (2009) 9070–6. doi:10.1021/jp810975v.

[160] E. Fantechi, C. Innocenti, M. Zanardelli, M. Fittipaldi, E. Falvo, M. Carbo, et al., A Smart Platform for Hyperthermia Application in Cancer Treatment: Cobalt-Doped Ferrite Nanoparticles Mineralized in Human Ferritin Cages, ACS Nano. 8 (2014) 4705–4719. http://pubs.acs.org/doi/abs/10.1021/nn500454n (accessed December 4, 2014).

[161] D. Peddis, C. Cannas, G. Piccaluga, E. Agostinelli, D. Fiorani, Spin-glass-like freezing and enhanced magnetization in ultra-small CoFe2O4 nanoparticles., Nanotechnology. 21 (2010) 125705 1–10. doi:10.1088/0957-4484/21/12/125705.

[162] S. Kubickova, D. Niznansky, M.P. Morales Herrero, G. Salas, J. Vejpravova, Structural disorder versus spin canting in monodisperse maghemite nanocrystals, Appl. Phys. Lett. 104 (2014) 223105. doi:10.1063/1.4881331.

[163] B. Martínez, X. Obradors, L. Balcells, A. Rouanet, C. Monty, Low Temperature Surface Spin-Glass Transition in γ- Fe2O3 Nanoparticles, Phys. Rev. Lett. 80 (1998) 181–184. http://link.aps.org/doi/10.1103/PhysRevLett.80.181.

[164] D. Lin, A.C. Nunes, C.F. Majkrzak, A.E. Berkowitz, Polarized neutron study of the magnetization density distribution within a CoFe2O4

colloidal particle II, J. Magn. Magn. Mater. 145 (1995) 343–348. doi:10.1016/0304-8853(94)01627-5.

[165] C.R. Alves, R. Aquino, J. Depeyrot, T. a. P. Cotta, M.H. Sousa, F. a. Tourinho, et al., Surface spin freezing of ferrite nanoparticles evidenced by magnetization measurements, J. Appl. Phys. 99 (2006) 08M905 1–3. doi:10.1063/1.2163844.

[166] D. Peddis, M. V Mansilla, S. Mørup, C. Cannas, A. Musinu, G. Piccaluga, et al., Spin-canting and magnetic anisotropy in ultrasmall CoFe2O4 nanoparticles., J. Phys. Chem. B. 112 (2008) 8507–8513. doi:10.1021/jp8016634.

[167] K. Maaz, S. Karim, A. Mashiatullah, J. Liu, M.D. Hou, Y.M. Sun, et al., Structural analysis of nickel doped cobalt ferrite nanoparticles prepared by coprecipitation route, Phys. B Condens. Matter. 404 (2009) 3947–3951. doi:10.1016/j.physb.2009.07.134.

[168] S. Kubickova, J. Vejpravova, P. Holec, D. Niznansky, Correlation of crystal structure and magnetic properties of Co(1−x)NixFe2O4/SiO2 nanocomposites, J. Magn. Magn. Mater. 334 (2013) 102–106. doi:10.1016/j.jmmm.2013.01.005.

[169] M. Mozaffari, J. Amighian, E. Darsheshdar, Magnetic and structural studies of nickel-substituted cobalt ferrite nanoparticles, synthesized by the sol–gel method, J. Magn. Magn. Mater. 350 (2014) 19–22. doi:10.1016/j.jmmm.2013.08.008.

[170] S. Singhal, J. Singh, S.. Barthwal, K. Chandra, Preparation and characterization of nanosize nickel-substituted cobalt ferrites (Co1−xNixFe2O4), J. Solid State Chem. 178 (2005) 3183–3189. doi:10.1016/j.jssc.2005.07.020.

[171] P.P. Hankare, K.R. Sanadi, K.M. Garadkar, D.R. Patil, I.S. Mulla, Synthesis and characterization of nickel substituted cobalt ferrite nanoparticles by sol–gel auto-combustion method, J. Alloys Compd. 553 (2013) 383–388. doi:10.1016/j.jallcom.2012.11.181.

[172] C.S. Kim, S.W. Lee, S.I. Park, J.Y. Park, Y.J. Oh, Atomic migration in Ni–Co ferrite, J. Appl. Phys. 79 (1996) 5428. doi:10.1063/1.362328.

[173] R.C. Kambale, P. a. Shaikh, S.S. Kamble, Y.D. Kolekar, Effect of cobalt substitution on structural, magnetic and electric properties of nickel

ferrite, J. Alloys Compd. 478 (2009) 599–603. doi:10.1016/j.jallcom.2008.11.101.

[174] L. Kumar, P. Kumar, M. Kar, Cation distribution by Rietveld technique and magnetocrystalline anisotropy of Zn substituted nanocrystalline cobalt ferrite, J. Alloys Compd. 551 (2013) 72–81. doi:10.1016/j.jallcom.2012.10.009.

[175] a. T. Ngo, P. Bonville, M.P. Pileni, Spin canting and size effects in nanoparticles of nonstoichiometric cobalt ferrite, J. Appl. Phys. 89 (2001) 3370. doi:10.1063/1.1347001.

[176] N. Moumen, M. Pileni, Control of the size of cobalt ferrite magnetic fluid, J. Phys. Chem. (1996) 1867–1873. http://pubs.acs.org/doi/abs/10.1021/jp9524136 (accessed October 10, 2014).

[177] H. Qu, J. Li, Remanence enhancement in magnetically interacting particles, Phys. Rev. B. 68 (2003) 212402. doi:10.1103/PhysRevB.68.212402.

[178] F. Morup, M.F. Hansen, C. Frandsen, S. Mørup, M.F. Hansen, C. Frandsen, Magnetic Nanoparticles, Compr. Nanosci. Technol. 1 (2011) 437–491. doi:http://dx.doi.org/10.1016/B978-0-12-374396-1.00036-2.

[179] a. Virden, S. Wells, K. O'Grady, Physical and magnetic properties of highly anisotropic cobalt ferrite particles, J. Magn. Magn. Mater. 316 (2007) e768–e771. doi:10.1016/j.jmmm.2007.03.100.

[180] A.J. Rondinone, C. Liu, Z.J. Zhang, Determination of Magnetic Anisotropy Distribution and Anisotropy Constant of Manganese Spinel Ferrite Nanoparticles, J. Phys. Chem. B. 105 (2001) 7967–7971. doi:10.1021/jp011183u.

[181] E.C. Sousa, M.H. Sousa, G.F. Goya, H.R. Rechenberg, M.C.F.L. Lara, F. a. Tourinho, et al., Enhanced surface anisotropy evidenced by Mössbauer spectroscopy in nickel ferrite nanoparticles, J. Magn. Magn. Mater. 272-276 (2004) E1215–E1217. doi:10.1016/j.jmmm.2003.12.295.

[182] H. Nathani, S. Gubbala, R.D.K. Misra, Magnetic behavior of nanocrystalline nickel ferrite, Mater. Sci. Eng. B. 121 (2005) 126–136. doi:10.1016/j.mseb.2005.03.016.

[183] G. Concas, G. Spano, C. Cannas, A. Musinu, D. Peddis, G. Piccaluga, Inversion degree and saturation magnetization of different nanocrystalline cobalt ferrites, J. Magn. Magn. Mater. 321 (2009) 1893–1897. doi:10.1016/j.jmmm.2008.12.001.

[184] J. Wang, Prepare highly crystalline NiFe2O4 nanoparticles with improved magnetic properties, Mater. Sci. Eng. B. 127 (2006) 81–84. doi:10.1016/j.mseb.2005.09.003.

[185] D. Carta, G. Mountjoy, G. Navarra, M.F. Casula, D. Loche, S. Marras, et al., X-ray Absorption Investigation of the Formation of Cobalt Ferrite Nanoparticles in an Aerogel Silica Matrix, J. Phys. Chem. C. 111 (2007) 6308–6317. doi:10.1021/jp0708805.

[186] S. Chkoundali, S. Ammar, N. Jouini, F. Fiévet, P. Molinié, M. Danot, et al., Nickel ferrite nanoparticles: elaboration in polyol medium via hydrolysis, and magnetic properties, J. Phys. Condens. Matter. 16 (2004) 4357–4372. doi:10.1088/0953-8984/16/24/017.

[187] C. Cannas, A. Falqui, A. Musinu, D. Peddis, G. Piccaluga, Piccaluga.G., CoFe2O4 nanocrystalline powders prepared by citrate-gel methods: Synthesis, structure and magnetic properties, J. Nanoparticle Res. 8 (2006) 255–267. doi:10.1007/s11051-005-9028-7.

[188] E. Morán, M. Blesa, M.-E. Medina, Nonstoichiometric Spinel Ferrites Obtained from α-NaFeO2 via Molten Media Reactions, Inorg. Chem. 41 (2002) 5961–5967. doi:10.1021/ic011302k.

[189] G.A. Sawatzky, F. Van Der Woude, A.H. Morrish, Mossbauer Study of Several Ferrimagnetic Spinels, Phys. Rev. B. 187 (1969) 747–757. http://link.aps.org/doi/10.1103/PhysRev.187.747.

[190] T.A. Anhøj, B. Bilenberg, B. Thomsen, C.D. Damsgaard, H.K. Rasmussen, C.S. Jacobsen, et al., Spin canting and magnetic relaxation phenomena in Mn0.25Zn0.75Fe2O4, J. Magn. Magn. Mater. 260 (2003) 115–130. doi:10.1016/S0304-8853(02)01237-4.

[191] S. Ammar, A. Helfen, N. Jouini, Magnetic properties of ultrafine cobalt ferriteparticles synthesized by hydrolysis in a polyol medium, J. Mater. Chem. (2001) 186–192. doi:10.1039/b003193n.

[192] C. Feldmann, Polyol-Mediated Synthesis of Nanoscale Functional Materials, Adv. Funct. Mater. 13 (2003) 101–107. doi:10.1002/adfm.200390014.

[193] R.J. Joseyphus, T. Matsumoto, H. Takahashi, D. Kodama, K. Tohji, B. Jeyadevan, Designed synthesis of cobalt and its alloys by polyol process, J. Solid State Chem. 180 (2007) 3008–3018. doi:10.1016/j.jssc.2007.07.024.

[194] R. Street, S.D. Brown, Magnetic viscosity, fluctuation fields, and activation energies (invited), J. Appl. Phys. 76 (1994) 6386–6390. http://dx.doi.org/10.1063/1.358275.

[195] V. Karanasos, I. Panagiotopoulos, D. Niarchos, H. Okumura, G.C. Hadjipanayis, Magnetic properties and granular structure of CoPt/B films, J. Appl. Phys. 88 (2000) 2740–2744. http://dx.doi.org/10.1063/1.1287230.

[196] K. O'Grady, H. Laidler, The limits to magnetic recording — media considerations, J. Magn. Magn. Mater. 200 (1999) 616–633. doi:10.1016/S0304-8853(99)00499-0.

[197] J. de Toro, P. Normile, Controlled Close-Packing of Ferrimagnetic Nanoparticles: An Assessment of the Role of Interparticle Superexchange Versus Dipolar Interactions, J. …. (2013). http://pubs.acs.org/doi/abs/10.1021/jp402444x (accessed February 10, 2014).

[198] S. Sun, Monodisperse FePt Nanoparticles and Ferromagnetic FePt Nanocrystal Superlattices, Science (80-.). 287 (2000) 1989–1992. doi:10.1126/science.287.5460.1989.

[199] G. Herzer, The Random Anisotropy Model, in: B. Idzikowski, P. Švec, M. Miglierini (Eds.), Prop. Appl. Nanocrystalline Alloy. from Amorph. Precursors SE - 2, Springer Netherlands, 2005: pp. 15–34. doi:10.1007/1-4020-2965-9_2.

[200] J.C. Denardin, W.C. Nunes, M. Knobel, Effects of magnetic interparticle coupling in the blocking temperature of granular Co multilayers, Phys. B Condens. Matter. 384 (2006) 290–293. doi:10.1016/j.physb.2006.06.013.

[201] W. Nunes, L. Socolovsky, J. Denardin, F. Cebollada, A. Brandl, M. Knobel, Role of magnetic interparticle coupling on the field dependence

of the superparamagnetic relaxation time, Phys. Rev. B. 72 (2005) 212413. doi:10.1103/PhysRevB.72.212413.

[202] J.G. Barbosa, M.R. Pereira, J. a Mendes, M.P. Proença, J.P. Araújo, B.G. Almeida, Cobalt ferrite thin films deposited by electrophoresis on p-doped Si substrates, J. Phys. Conf. Ser. 200 (2010) 072009. doi:10.1088/1742-6596/200/7/072009.

[203] M. Knobel, W.C. Nunes, H. Winnischofer, T.C.R. Rocha, L.M. Socolovsky, C.L. Mayorga, et al., Effects of magnetic interparticle coupling on the blocking temperature of ferromagnetic nanoparticle arrays, J. Non. Cryst. Solids. 353 (2007) 743–747. doi:10.1016/j.jnoncrysol.2006.12.037.

[204] a. Michels, R. Viswanath, J. Barker, R. Birringer, J. Weissmüller, Range of Magnetic Correlations in Nanocrystalline Soft Magnets, Phys. Rev. Lett. 91 (2003) 267204. doi:10.1103/PhysRevLett.91.267204.

[205] Y. Tokura, Orbital Physics in Transition-Metal Oxides, Science (80-.). 288 (2000) 462–468. doi:10.1126/science.288.5465.462.

[206] E. Dagotto, Complexity in strongly correlated electronic systems., Science. 309 (2005) 257–62. doi:10.1126/science.1107559.

[207] Y. Tokura, Y. Tomioka, Colossal magnetoresistive manganites, J. Magn. Magn. Mater. 200 (1999) 1–23. doi:10.1016/S0304-8853(99)00352-2.

[208] P. Anil Kumar, S. Ray, S. Chakraverty, D.D. Sarma, Engineered spin-valve type magnetoresistance in Fe3O4-CoFe2O4 core-shell nanoparticles, Appl. Phys. Lett. 103 (2013) 102406. doi:10.1063/1.4819956.

[209] T. Fujii, M. Kawasaki, A. Sawa, H. Akoh, Y. Kawazoe, Y. Tokura, Hysteretic current–voltage characteristics and resistance switching at an epitaxial oxide Schottky junction SrRuO3／SrTi0.99Nb0.01O3, Appl. Phys. Lett. 86 (2005) 012107. doi:10.1063/1.1845598.

[210] D. Choudhury, P. Mandal, R. Mathieu, A. Hazarika, S. Rajan, A. Sundaresan, et al., Near-Room-Temperature Colossal Magnetodielectricity and Multiglass Properties in Partially Disordered LaNiMnO6, Phys. Rev. Lett. 108 (2012) 127201. doi:10.1103/PhysRevLett.108.127201.

[211] D. Khomskii, Classifying multiferroics: Mechanisms and effects, Physics (College. Park. Md). 2 (2009). doi:10.1103/Physics.2.20.

[212] J.F. Scott, Applications of magnetoelectrics, J. Mater. Chem. 22 (2012) 4567. doi:10.1039/c2jm16137k.

[213] H. Zheng, J. Wang, S.E. Lofland, Z. Ma, L. Mohaddes-Ardabili, T. Zhao, et al., Multiferroic BaTiO3-CoFe2O4 Nanostructures., Science. 303 (2004) 661–3. doi:10.1126/science.1094207.

[214] R.K. Zheng, H. Gu, B. Xu, X.X. Zhang, The origin of the non-monotonic field dependence of the blocking temperature in magnetic nanoparticles., J. Phys. Condens. Matter. 18 (2006) 5905–10. doi:10.1088/0953-8984/18/26/010.

[215] P. Anil Kumar, D.D. Sarma, Effect of "dipolar-biasing" on the tunability of tunneling magnetoresistance in transition metal oxide systems, Appl. Phys. Lett. 100 (2012) 262407. doi:10.1063/1.4731206.

[216] T. Sarkar, a K. Raychaudhuri, a K. Bera, S.M. Yusuf, Effect of size reduction on the ferromagnetism of the manganite La1−x CaxMnO3 (x =0.33), New J. Phys. 12 (2010) 123026. doi:10.1088/1367-2630/12/12/123026.

[217] T. Sarkar, B. Ghosh, A.K. Raychaudhuri, T. Chatterji, Crystal structure and physical properties of half-doped manganite nanocrystals of less than 100-nm size, Phys. Rev. B. 77 (2008) 235112. http://link.aps.org/doi/10.1103/PhysRevB.77.235112 (accessed April 3, 2013).

[218] K. Shankar, A. Raychaudhuri, Low-temperature polymer precursor-based synthesis of nanocrystalline particles of lanthanum calcium manganese oxide (La0.67Ca0.33MnO3) with enhanced ferromagnetic transition temperature, J. Mater. Res. 21 (2006) 27–33. doi:10.1557/JMR.2006.0031.

[219] S. Xi, W. Lu, Y. Sun, Magnetic properties and magnetocaloric effect of La0.8Ca0.2MnO3 nanoparticles tuned by particle size, J. Appl. Phys. 111 (2012) 063922. doi:10.1063/1.3699037.

[220] Y. Tokura, ed., Colossal magnetoresistive oxides, CRC Press, 2000.

[221] L. Liu, J.J. Zheng, S.L. Yuan, Z.M. Tian, C.H. Wang, The magnetic properties of nanosized La1−xCaxMnO3 ($0.5 \leq x \leq 0.8$), J. Nanoparticle Res. 13 (2010) 2305–2310. doi:10.1007/s11051-010-9988-0.

[222] A. Martinelli, M. Ferretti, C. Castellano, M.R. Cimberle, R. Masini, D. Peddis, et al., Structural, microstructural and magnetic properties of (La1−xCax)MnO3 nanoparticles, J. Phys. Condens. Matter. 25 (2013) 176003. doi:10.1088/0953-8984/25/17/176003.

[223] D. Markovic, V. Kusigerski, M. Tadic, J. Blanusa, M.V. Antisari, V. Spasojevic, Magnetic properties of nanoparticle La0.7Ca0.3MnO3 prepared by glycine–nitrate method without additional heat treatment, Scr. Mater. 59 (2008) 35–38. doi:10.1016/j.scriptamat.2008.02.020.

[224] M.A. Lopez-Quintela, L.E. Hueso, J. Rivas, F. Rivadulla, Intergranular magnetoresistance in nanomanganites, Nanotechnology. 14 (2003) 212–219. http://iopscience.iop.org/0957-4484/14/2/322 (accessed October 8, 2014).

[225] E.P. Wohlfarth, Relations between Different Modes of Acquisition of the Remanent Magnetization of Ferromagnetic Particles, J. Appl. Phys. 29 (1958) 595–596.

[226] N. Domingo, D. Fiorani, a M. Testa, C. Binns, S. Baker, J. Tejada, Exchange bias in a superspin glass system of Co particles in Mn matrix, J. Phys. D. Appl. Phys. 41 (2008) 134009. doi:10.1088/0022-3727/41/13/134009.

[227] M. Blancomantecon, K. Ogrady, Interaction and size effects in magnetic nanoparticles, J. Magn. Magn. Mater. 296 (2006) 124–133. doi:10.1016/j.jmmm.2004.11.580.

[228] R. Mathieu, P. Svedlindh, R. Chakalov, Z. Ivanov, Grain-boundary effects on magnetotransport in La0.7Sr0.3MnO3 biepitaxial films, Phys. Rev. B. 62 (2000) 3333–3339. http://journals.aps.org/prb/abstract/10.1103/PhysRevB.62.3333 (accessed November 8, 2014).

[229] N. Zhang, W. Ding, W. Zhong, D. Xing, Y. Du, Tunnel-type giant magnetoresistance in the granular perovskite La0.85Sr0.15MnO3, Phys. Rev. B. 56 (1997) 8138–8142. http://journals.aps.org/prb/abstract/10.1103/PhysRevB.56.8138 (accessed October 15, 2014).

[230] L. Balcells, J. Fontcuberta, B. Martínez, X. Obradors, High-field magnetoresistance at interfaces in manganese perovskites, Phys. Rev. B. 58 (1998) R14697–R14700. doi:10.1103/PhysRevB.58.R14697.

[231] P. Dey, T. Nath, Effect of grain size modulation on the magneto- and electronic-transport properties of La0.7Ca0.3MnO3 nanoparticles: The role of spin-polarized tunneling at the enhanced grain surface, Phys. Rev. B. 73 (2006) 214425. doi:10.1103/PhysRevB.73.214425.

[232] D. Varshney, M.A. Dar, Structural and magneto-transport properties of (1−x)La0.67Sr0.33MnO3 (LSMO)+(x)BaTiO3 (BTO) composites, J. Alloys Compd. 619 (2015) 122–130. doi:10.1016/j.jallcom.2014.08.219.

[233] D. Markovic, V. Kusigerski, M. Tadic, J. Blanusa, Z. Jaglicic, N. Cvjeticanin, et al., The influence of the heat treatment on the structural and magnetic properties of nanoparticle La0.7Ca0.3MnO3 prepared by glycine–nitrate method, J. Alloys Compd. 494 (2010) 52–57. doi:10.1016/j.jallcom.2010.01.062.

[234] E. Restrepo-Parra, G. Orozco-Hernández, J.C. Riaño-Rojas, Monte Carlo simulation of surface anisotropy in La2/3Ca1/3MnO3 nanoparticles, J. Magn. Magn. Mater. 344 (2013) 44–48. doi:10.1016/j.jmmm.2013.05.002.

[235] T. Zhang, G. Li, T. Qian, J.F. Qu, X.Q. Xiang, X.G. Li, Effect of particle size on the structure and magnetic properties of La[sub 0.6]Pb[sub 0.4]MnO[sub 3] nanoparticles, J. Appl. Phys. 100 (2006) 094324. doi:10.1063/1.2364622.

[236] V.M. Andrade, R.J. Caraballo-Vivas, T. Costas-Soares, S.S. Pedro, D.L. Rocco, M.S. Reis, et al., Magnetic and structural investigations on La0.6Sr0.4MnO3 nanostructured manganite: Evidence of a ferrimagnetic shell, J. Solid State Chem. 219 (2014) 87–92. doi:10.1016/j.jssc.2014.07.013.

[237] V. Spasojevic, A. Mrakovic, M. Perovic, V. Kusigerski, J. Blanusa, Superspin-glass like behavior of nanoparticle La0.7Ca0.3MnO3 obtained by mechanochemical milling, J. Nanoparticle Res. 13 (2010) 763–771. doi:10.1007/s11051-010-0076-2.

[238] A. Rostamnejadi, H. Salamati, P. Kameli, H. Ahmadvand, Superparamagnetic behavior of La0.67Sr0.33MnO3 nanoparticles

prepared via sol–gel method, J. Magn. Magn. Mater. 321 (2009) 3126–3131. doi:10.1016/j.jmmm.2009.05.035.

[239] P. Dey, T.K. Nath, P.K. Manna, S.M. Yusuf, Enhanced grain surface effect on magnetic properties of nanometric La0.7Ca0.3MnO3 manganite: Evidence of surface spin freezing of manganite nanoparticles, J. Appl. Phys. 104 (2008) 103907. doi:10.1063/1.3020524.

[240] T. Ji, J. Fang, V. Golob, J. Tang, C.J. O'Connor, Preparation and magnetic properties of La0.9Ca0.1MnO3 nanoparticles at 300 °C, J. Appl. Phys. 92 (2002) 6833. doi:10.1063/1.1513880.

[241] S.B. Xi, W.J. Lu, H.Y. Wu, P. Tong, Y.P. Sun, Surface spin-glass, large surface anisotropy, and depression of magnetocaloric effect in La0.8Ca0.2MnO3 nanoparticles., J. Appl. Phys. 112 (2012) 123903. doi:10.1063/1.4768842.

[242] J. Du, Y. Gao, L. Chai, G. Zou, Y. Li, Y. Qian, Hausmannite Mn3O4 nanorods: synthesis, characterization and magnetic properties, Nanotechnology. 17 (2006) 4923–4928. doi:10.1088/0957-4484/17/19/024.

[243] R. Bussamara, W.W.M. Melo, J.D. Scholten, P. Migowski, G. Marin, M.J.M. Zapata, et al., Controlled synthesis of Mn3O4 nanoparticles in ionic liquids., Dalton Trans. 42 (2013) 14473–9. doi:10.1039/c3dt32348j.

[244] D. Choudhury, S. Mukherjee, P. Mandal, A. Sundaresan, U. V. Waghmare, S. Bhattacharjee, et al., Tuning of dielectric properties and magnetism of SrTiO3 by site-specific doping of Mn, Phys. Rev. B. 84 (2011) 125124. doi:10.1103/PhysRevB.84.125124.

[245] T. Zhu, B.G. Shen, J.R. Sun, H.W. Zhao, W.S. Zhan, Surface spin-glass behavior in La2/3Sr1/3MnO3 nanoparticles, Appl. Phys. Lett. 78 (2001) 3863. doi:10.1063/1.1379597.

[246] H. Khurshid, W. Li, M.-H. Phan, P. Mukherjee, G.C. Hadjipanayis, H. Srikanth, Surface spin disorder and exchange-bias in hollow maghemite nanoparticles, Appl. Phys. Lett. 101 (2012) 022403. doi:10.1063/1.4733621.

[247] A. Cabot, A.P. Alivisatos, V.F. Puntes, L. Balcells, Ò. Iglesias, A. Labarta, Magnetic domains and surface effects in hollow maghemite

nanoparticles, Phys. Rev. B. 79 (2009) 94419. http://link.aps.org/doi/10.1103/PhysRevB.79.094419.

[248] S.S.P. Parkin, K.P. Roche, M.G. Samant, P.M. Rice, R.B. Beyers, R.E. Scheuerlein, et al., Exchange-biased magnetic tunnel junctions and application to nonvolatile magnetic random access memory (invited), J. Appl. Phys. 85 (1999) 5828–5833. doi:10.1063/1.369932.

[249] H. Zeng, J. Li, J.P. Liu, Z.L. Wang, S. Sun, Exchange-coupled nanocomposite magnets by nanoparticle self-assembly., Nature. 420 (2002) 395–398. doi:10.1038/nature01208.

[250] K. O'Grady, H. Laidler, K.O. Grady, The limits to magnetic recording -- media considerations, J. Magn. Magn. Mater. 200 (1999) 616–633.

[251] J. Nogués, J. Sort, V. Langlais, V. Skumryev, S. Suriñach, J.S. Muñoz, et al., Exchange bias in nanostructures, Phys. Rep. 422 (2005) 65–117. doi:10.1016/j.physrep.2005.08.004.

[252] D.I. Khomskii, Orbital Effects in Manganites, Int. J. Mod. Phys. B. 15 (2001) 2665–2681. doi:10.1142/S0217979201006380.

[253] C. Zener, Interaction between the d-Shells in the Transition Metals. II. Ferromagnetic Compounds of Manganese with Perovskite Structure, Phys. Rev. 82 (1951) 403–405. http://link.aps.org/doi/10.1103/PhysRev.82.403.

[254] D. Peddis, D. Rinaldi, G. Ennas, A. Scano, E. Agostinelli, D. Fiorani, Superparamagnetic blocking and superspin-glass freezing Q2 in ultra small d-(Fe0.67Mn0.33)OOH particles, Phys. Chem. Chem. Phys. 14 (2012) 3162–9. doi:10.1039/c2cp22473a.Please.

[255] B.N. Pianciola, E. Lima, H.E. Troiani, L.C.C.M. Nagamine, R. Cohen, R.D. Zysler, Size and surface effects in the magnetic order of CoFe2O4 nanoparticles, J. Magn. Magn. Mater. 377 (2015) 44–51. doi:10.1016/j.jmmm.2014.10.054.

[256] M. Sasaki, P. Jönsson, H. Takayama, H. Mamiya, Aging and memory effects in superparamagnets and superspin glasses, Phys. Rev. B. 71 (2005) 1–9. doi:10.1103/PhysRevB.71.104405.

[257] R. Grössinger, A critical examination of the law of approach to saturation. I. Fit procedure, Phys. Status Solidi. 66 (1981) 665–674. doi:10.1002/pssa.2210660231.

[258] K. O'Grady, R.W. Chantrell, Remanence Curves of Fine particles Systems I: Experimental Studies, (1992).